

**Ultrafast Dynamics in InAs Quantum Dot
and GaInNAs Quantum Well
Semiconductor Heterostructures**

Thesis submitted to the University of St Andrews
in application for the degree of Doctor of Philosophy

David Brendan Malins



University
of
St Andrews

School of Physics and Astronomy

University of St Andrews

Fife, Scotland

October 2007

Declaration

I, David Brendan Malins, hereby certify that this thesis, which is approximately 36500 words in length, has been written by me, that it is the record of work carried out by me and that it has not been submitted in any previous application for a higher degree.

Date

Signature of candidate

I was admitted as a candidate for the degree of Doctor of Philosophy in December, 2003; the higher study for which this is a record was carried out in the University of St. Andrews between 2003 and 2007.

Date

Signature of candidate

I hereby certify that the candidate has fulfilled the conditions of the Resolution and Regulations appropriate for the degree of Doctor of Philosophy in the University of St. Andrews and that the candidate is qualified to submit this thesis in application for that degree.

Date

Signature of supervisor

Unrestricted

In submitting this thesis to the University of St. Andrews I understand that I am giving permission for it to be made available for use in accordance with the regulations of the University Library for the time being in force, subject to any copyright vested in the work not being affected thereby. I also understand that the title and abstract will be published, and that a copy of the work may be made and supplied to any bona fide library or research worker.

Date

Signature of candidate

Abstract

The quantum confined Stark effect (QCSE) and ultrafast absorption dynamics near the bandedge have been investigated in p-i-n waveguides comprising quantum confined heterostructures grown on GaAs substrates, for emission at $1.3\mu\text{m}$. The materials are; isolated InAs/InGaAs dot-in-a-well (DWELL) quantum dots (QD), bilayer InAs quantum dots and GaInNAs multiple quantum wells (MQW). The focus was to investigate these dynamics in a planar waveguide geometry, for the purpose of large scale integration in optical systems.

Initial measurements of the QCSE using photocurrent measurements showed a small shift for isolated QDs whilst a significant shift of 40nm (at 1340nm) was demonstrated for bilayer dots, comparable to that of GaInNAs MQW (30nm at 1300nm). These are comparable to InP based quaternary multiple quantum wells used in modulator devices.

With the use of a broadband continuum source the isolated quantum dots exhibit both a small QCSE (15nm at 1280nm) and minimal broadening which is desirable for saturable absorbers used in monolithic modelocked semiconductor lasers (MMSL). A robust experimental set-up was developed for characterising waveguide modulators whilst the electroabsorption and electro-refraction was calculated ($\Delta n \approx 1.5 \times 10^{-3}$) using the Kramers-Kronig dispersion relation.

Pump probe measurements were performed at room temperature using 250fs pulses from an optical parametric oscillator (OPO) on the three waveguide samples. For the isolated QDs ultrafast absorption recovery was recorded from 62ps (0V) to 700fs (-10V) and the shortest times shown to be due to tunneling. Additionally we have shown good agreement of the temperature dependence of these dots and the pulse width durations from a modelocked semiconductor laser using the same material. Bilayer QDs are shown to exhibit ultrafast absorption recovery from 119ps (0V) to 5ps (-10V) offering potential for applications as modelocking elements. The GaInNAs multiple quantum wells show absorption recovery of 55ps (0V), however under applied reverse bias they exhibit long lived field screening transients. These results are explained qualitatively by the spatial separation of electrons and holes at heterobarrier interfaces.

Contents

1	Introduction	1
1.1	Optical communications	1
1.2	Electro-Optical modulators	5
1.2.1	Intensity modulators	6
1.2.2	Phase modulators	7
1.3	Optical propagation and dispersion	8
1.4	Nonlinear refraction in active semiconductors	10
1.5	Summary	10
	References for Chapter 1	11
2	Optical properties of semiconductor heterostructures	14
2.1	Bulk III-V compound semiconductors	14
2.2	Low dimensional effects: The quantum well	19
2.2.1	Quantum confinement energy	20
2.2.2	Optical transitions	25
2.2.3	Optical nonlinearities	30
2.3	GaNAs multiple quantum wells	31
2.3.1	Electronic Structure	32
2.3.2	Recombination centres	34
2.4	Quantum dot heterostructures	35
2.4.1	Energy levels in QD systems	35
2.4.2	Bilayer InAs/GaAs quantum dots	36
2.5	Electric field effects: The p-n junction	38
2.5.1	Thermionic emission theory	40

2.5.2	Field emission - Fowler-Nordheim tunneling	42
2.5.3	Electro-absorption mechanisms in bulk	43
2.5.4	The quantum confined Stark effect (QCSE)	45
2.6	Summary	48
	References for Chapter 2	49
3	Development of Femtosecond and Broadband Optical Sources	52
3.1	Introduction	52
3.2	Optical parametric Oscillator	52
3.2.1	Coupled wave equations	53
3.2.2	Quasi-phasematching	55
3.2.3	Optical properties of the gain medium (PPLN)	56
3.2.4	OPO cavity	59
3.2.5	The pump laser system	61
3.2.6	Pulse diagnostics	62
3.3	Characterisation of the OPO	65
3.3.1	Length tuning	66
3.3.2	Power measurements	67
3.3.3	Grating and temperature tuning	68
3.4	Supercontinuum generation for linear measurements	69
3.4.1	Dispersion in optical fibre	69
3.4.2	Nonlinearities in optical fibre	70
3.4.3	Microstructured fibre and continuum generation	71
3.5	Summary	73
	References for Chapter 3	74
4	Characterisation and Fabrication of active waveguide devices	75
4.1	Introduction	75
4.2	Experimental setup: Spontaneous emission (SE)	76
4.3	Sample 101: InAs-InGaAs-GaAs DWELL	77
4.3.1	Spontaneous emission results	78
4.4	Sample 102: InAs-GaAs Bilayer QD	80

4.4.1	Spontaneous emission results	81
4.5	Sample 103: GaInNAs MQW	82
4.5.1	Mode solving with effective index	83
4.5.2	Photolithography and Ion beam milling	83
4.5.3	Contacts and cleaving	88
4.5.4	Output (IL) and Voltage (IV) results (950nm etch)	91
4.5.5	Output (IL) results (1300nm etch)	92
4.6	Summary	92
	References for Chapter 4	94
5	Linear characterisation and Electro-refraction	95
5.1	Introduction	95
5.2	Investigation of the quantum-confined Stark effect	95
5.3	Photocurrent measurements	96
5.3.1	Results for single QDs: Sample 101	97
5.3.2	Results for Bilayer QDs: Sample 102	99
5.3.3	Results for GaInNAs MQWs: Sample 103	100
5.4	Optical transmission measurements (I): Tuneable laser	102
5.4.1	Experimental setup	102
5.4.2	Absorption results for single QDs: Sample 101	103
5.5	Optical transmission measurements (II):Tuneable supercontinuum	104
5.5.1	Transmission setup with real-time normalisation	104
5.5.2	Absorption results for single QDs: sample 101	106
5.5.3	Refractive index results for isolated QDs	108
5.6	Summary	109
	References for Chapter 5	111
6	Nonlinear Electro-absorption dynamics	113
6.1	Introduction	113
6.2	Pump-probe technique	113
6.2.1	Ultrafast carrier dynamics	116
6.2.2	Waveguide coupling efficiency	117

6.3	Time dependent carrier escape in InAs Dots-in-a-well (DWELL)	120
6.3.1	Temperature dependent escape in InAs DWELL	125
6.4	Absorption recovery in InAs/GaAs Bilayer QD's	128
6.5	Field dependent absorption dynamics in GaInNAs MQWs	133
6.5.1	Field screening effects	133
6.5.2	Results for absorption recovery	134
6.5.3	Field screening dynamics involving heterobarriers	136
6.6	Summary	138
	References for Chapter 6	140
7	Summary and Conclusions	144
7.1	Summary of thesis	144
7.2	InAs quantum dots	145
7.3	InAs Bilayer Quantum dots	146
7.4	GaInNAs Multiple Quantum wells	147
7.5	Linear measurements	148
7.6	Time-resolved measurements	148
7.7	Device prospects	149
7.8	Further work	149
	References for Chapter 7	151
A	Numerical evaluation of the Kramers-Krönig relations	152
A.0.1	Method A	154
A.0.2	Method B	155
A.0.3	Discussion	156
	References for Chapter A	157

Chapter 1

Introduction

The aim of the research described in this thesis was to investigate new materials for optical telecommunications at wavelengths around $1.3\mu\text{m}$, based on GaAs substrates, as an alternative platform to InP. From a commercial point of view it is cost effective to have devices that have good temperature characteristics and can operate without expensive cooling solutions. From a technological point of view optoelectronic devices on GaAs substrates offer the potential to utilise fabrication expertise from the electronics industry. The specific devices investigated in the following chapters are based on the electro-absorption modulator. Although not limited to such applications, these devices can be used for switching in optical networks and also as saturable absorbers in passively modelocked semiconductor lasers.

1.1 Optical communications

Semiconductor edge emitting laser diodes based on InGaAsP/InP are widely deployed in current long-haul telecommunications networks. They cover the zero dispersion point and absorption minimum of silica fibre in the spectral range of 1300-1550nm. One of the major drawbacks with this technology is the expensive nature of the thermoelectric cooling needed due to the typically poor characteristic temperature (T_0) of InGaAsP lasers. The figure of merit (FOM) for the temperature stability of threshold current density (J_{th}) in such ridge waveguide lasers is defined as,

$$J_{th} = J_0 \exp\left(\frac{T}{T_0}\right). \quad (1.1)$$

The development of lower cost vertical cavity surface emitting lasers (VCSELs), has led to devices exhibiting low threshold currents, low beam divergence and symmetrical optical modes [1]. This has introduced the problem of fabricating Bragg reflecting mirrors in such structures, using InGaAsP/InP layers which have very little refractive index contrast. Adding many periods increases the optical losses and exacerbates the thermal issue further. The inclusion of InGaAlAs in the cladding layers can increase the confinement due to the increased band offset, improving T_0 (90-110 K) [2, 3]. However, this is still low compared to other materials and such intricate structures complicate the growth process further [4] which in turn increases the cost. An alternative to this is to use GaAs based material due to the low cost of such substrates and its good thermal properties in AlGaAs/GaAs lasers. Currently there are four proposed methods which can achieve 1.3-1.55 μm emission for active devices; they are GaInNAs and GaAsSb quantum wells (QWs), InGaAs strained quantum wells and InAs/GaAs quantum dots (QDs).

GaInNAs quantum wells

Adding small amounts of nitrogen to GaAs is found to decrease the lattice constant and band-gap which leads to long wavelength emission [5], although at high concentrations the alloy exhibits phase separation. Addition of In to GaAs has the effect of increasing the lattice constant whilst decreasing the band-gap. For this reason GaInNAs can be lattice matched to GaAs with suitable material quality for the processing of long wavelength lasers [6]. When a thin layer of GaInNAs is sandwiched between GaAs layers, very deep quantum wells can be formed which strongly confine the electrons in the conduction band and thus improve the temperature characteristics of such devices. Continuous wave (CW) room temperature lasing at 1.31 μm was first demonstrated in a $Ga_{0.7}In_{0.3}N_{0.01}As_{0.99}$ strained quantum well laser grown by molecular beam epitaxy (MBE) [7]. The minimisation of nitrogen content is essential to maintain high crystalline quality of such material. Characteristic temperatures (T_0) of 215K have been reported [8], however current densities are typically higher than other GaAs based lasers, at 400-680 Acm^{-2} [9]. Evidence

also suggests that 50% of the current density is lost via non-radiative recombination [10]. More recently, electrically pumped GaInNAs VCSEL's have been demonstrated at operating wavelengths up to $1.34\mu\text{m}$ at room temperature with a threshold current of 2.8mA [11].

GaAsSb quantum wells

The addition of Sb to GaAs can be achieved to high concentrations, whilst still maintaining good material quality. A highly strained $\text{GaAs}_{0.66}\text{Sb}_{0.34}$ QW laser was demonstrated at $1.27\mu\text{m}$ with $J_{th}=450\text{Acm}^{-2}$ [12]. However the band offset is small, which allows two transitions of similar energy. This gives rise to spectral broadening and poor current confinement [13]. Recent developments of such ridge waveguide lasers at $1.3\mu\text{m}$ wavelengths have resulted in low values for T_0 and evidence suggesting that 90% of the threshold current density is due to non-radiative recombination [14]. It is clear that this material system still requires much research, however the wavelength emission can be very long with optically pumped extended cavity VCSELs demonstrated at $2.4\mu\text{m}$ [15]. This will clearly have applications for communications and gas sensing capabilities in the future.

InAs/GaAs quantum dots

When InAs is grown on GaAs with a critical thickness of between 1.7 and 4 monolayers (ML) the strain due to the lattice mismatch leads to the formation of three dimensional islands, which exhibit atomic like properties. The transformation to quantum dots (QD) grown layer by layer with islands is known as the Stranski-Krasanow growth mode [16], having typical dimensions of 10nm base and 6nm height. Adding more InAs leads to relaxation of the strain and the red-shift of the band-gap energy is limited to about $1.24\mu\text{m}$. Atomic layer epitaxy (ALE) was first proposed by metal-organic vapour phase epitaxy (MOVPE), where elements are alternatively deposited, leading to 24ML dislocation free $\text{In}_{0.5}\text{Ga}_{0.5}\text{As}$ growth ($\lambda = 1.32\mu\text{m}$) [17]. Later this was demonstrated with molecular beam epitaxy (MBE) [18]. This leads to larger dots (20nm base and 10nm height) but with a reduced dot density (typically $1.3 \times 10^{10}\text{cm}^{-2}$). Room temperature lasing was first demonstrated in an ALE grown device with 11ML $\text{In}_{0.5}\text{Ga}_{0.5}\text{As}$ up to $1.31\mu\text{m}$ with a current density of 405Acm^{-2} [19]. However above room temperature such structures jump

to excited state lasing at $\lambda = 1.15\mu\text{m}$ due to saturation of the ground state gain with such low dot density. With the inclusion of AlGaAs capping to form a graded-index separate confinement heterostructure (SCH) and high reflection coatings, the current density can be reduced in such devices to 90Acm^{-2} . However, the saturation of the ground state remains a problem.

Free standing InAs on GaAs QDs exhibits strain relaxation and the wavelength can reach out to $1.53\mu\text{m}$ [20], however in real structures the strain is maintained and the wavelength range is limited. Introducing a strain reducing cap layer of InGaAs or InAlAs over the InAs QDs [21] can help extend the wavelength whilst maintaining the dot density as high as $7 \times 10^{10}\text{cm}^{-2}$ [22]. The development of these dot in a well (DWELL) structures has lead to emission at $\lambda = 1.285\mu\text{m}$ with $J_{th} = 24\text{Acm}^{-2}$ [23] and more recently $\lambda = 1.306\mu\text{m}$ with $J_{th} = 39\text{Acm}^{-2}$, operating up to 100°C [24]. The reason for such low J_{th} in QD lasers is the low transparency current density which is directly proportional to the number of available states (N_e) in the active region as (τ is the radiative recombination time),

$$J_{trans} = \left(\frac{qN_e}{2\tau} \right). \quad (1.2)$$

The adverse effect is a low modal gain which is easily saturated and is typically 9cm^{-1} for DWELL lasers [22]. Such gain is spread over a large photoluminescent (PL) spectral width due to the inhomogeneous size distribution of the QDs ($\sim 80\text{meV}$). The current method of overcoming low gain is to stack dot layers together with sufficient separation to avoid coupling and further strain effects [25], however the low gain is still an issue for QD VCSEL's. QD lasers tend to have high T_0 due to temperature independence of J_{trans} and high confinement of the carriers due to the large band offset relative to GaAs.

This thesis will concentrate on two of the technologies mentioned above, namely, GaInNAs QWs and InAs/GaAs QDs due to the extensive research in these materials and successful demonstration of operational devices to date.

InGaAs quantum wells

Strained InGaAs QW's have excellent device performance up to $1\mu\text{m}$. Incidentally InGaAs VCSELs are commercially available for use in local area networks (transmission $\sim 500\text{m}$) over multimode fibre at 850nm . However the cut-off wavelength of single mode fibre is around $1.2\mu\text{m}$ and due to the critical thickness issue of InAs, low temperature approaches need to be employed to grow such material capable of approaching $1.3\mu\text{m}$. Devices incorporating a strain buffer layer (SBL) below the active region have achieved close to $1.2\mu\text{m}$ whilst demonstrating a reduction in the PL bandwidth at full width half maximum of 33 to 23meV [26]. The down side to this is the higher J_{trans} (90Acm^{-1}) attributed to current leakage via the SBL and enhancement of point defects for non-radiative recombination from low temperature growth [27]. Additionally such lasers show low slope efficiencies compared to InP based lasers and this has been attributed to light scattering and absorption due to the strain induced crystalline imperfections. However they still show good temperature characteristics, with uncooled CW lasing being demonstrated with $T_0=140\text{K}$ [28]. In this situation the emission was also red-shifted to $1.256\mu\text{m}$ due to the band-gap being inversely proportional to temperature in such material whilst the chip heats up.

1.2 Electro-Optical modulators

Since the invention of the laser in 1960, the electro-optic effect in materials has played an integral part for amplitude, phase and polarisation modulation. Initially lithium niobate (LN) was used due to its low insertion loss however, the development of double heterostructure semiconductor lasers and the rapid improvements in material quality lead to the first efficient modulator in GaAs during 1973 [29]. One year later the first electro-optic switch comparable to LN was demonstrated in GaAs [30]. This breakthrough lead to intense research into a plethora of modulator devices based on the electro-optic bandedge shift in bulk semiconductors (Franz-Keldych effect) and quantum well semiconductors (quantum-confined Stark effect). The development of fibre optic communications has exploited the ability to directly modulate semiconductor lasers and further reduced the need for external modulators. The vast improvement in material quality and processing technologies paved the way for III-V semiconductor optical guides with propagation losses of 0.2-0.7dB/cm by

the mid 1980's. The last 20 years has seen a huge requirement for switching devices used for demultiplexing, wavelength switching and clock recovery of optic signals with three main aims: High speed, low power operation and large scale integration. Semiconductors offer the ability to manage their absorption and refractive index profiles by bandgap engineering. In addition, electrically driven devices allow these parameters to be actively changed in situ. Optical modulators generally come in two flavours; intensity (electro-absorption) modulators and phase (electro-refraction) modulators. These two effects are fundamentally connected via the optical susceptibility of the material and both can be changed by the application of a D.C. electric field. For a detailed history of different modulators, see for example Wakita [31].

1.2.1 Intensity modulators

Franz and Keldysh carried out some pioneering work in the late 1950s in bulk semiconductors. They predicted that under the influence of an electric field, absorption can occur below the forbidden band-gap. That is to say, the tunneling probability for electrons and holes increases and the probability of a transition below the band-gap energy is non-zero. This was later experimentally verified, however at this time large voltages were required and insertion losses were also high. During the 70s the introduction of double heterostructure growth techniques led to an increase in the research of this effect. With the added problems of chirp in directly modulated diode lasers, low-chirp Franz-Keldysh modulators were finally realised [32]. The 1980s saw the discovery of the quantum-confined-Stark-effect (QCSE) [33] in semiconductor quantum wells, under the influence of electric fields perpendicular to the wells. This effect differs from the Franz-Keldysh effect in that it involves an exciton (electron-hole bound pair) resonance which exists at room temperature (due to the lateral confinement of carriers). Under the influence of the field, the shift in binding energy of the pair is small compared to the energy shift for single particle states. However, the wavefunction overlap is reduced between the electron and hole and the absorption is reduced. The peak energy shift in the bandedge is approximately quadratic for low fields. For large wells, when excitons become neglected the effect is known as the quantum-confined Franz-Keldysh effect [34]. The QCSE is covered in more detail in chapter 2.

1.2.2 Phase modulators

The refractive index of a material can be altered by the strain induced via an applied electric field. Phase modulators can therefore be implemented using the inherent linear Pockels effect or the quadratic Kerr effect, depending on whether they are non-centrosymmetric or centrosymmetric crystals respectively. Additionally in bulk semiconductors the absorption of free carriers gives rise to plasma effects and bandgap renormalisation (details of which can be found in solid state texts such as Kittel [35]). These absorption changes are related to the refractive index and hence the change in phase of the propagating wave via the Kramers-Kronig dispersion relation. The linear and quadratic electro-optic effects mentioned above dominate the contributions that alter the refractive index at long wavelengths. However for wavelengths close to the absorption edge, the bandgap shift and quadratic electro-optic effects become dominant.

The use of phase changing elements (such as semiconductor optical amplifiers) in combination with a directional coupler or optical interferometer can also provide amplitude modulation. Two such examples of this are the Terahertz-Optical -Asymmetrical-Demultiplexer (TOAD) [36] and the Mach-Zehnder interferometer configuration [37], as shown in figure 1.1.

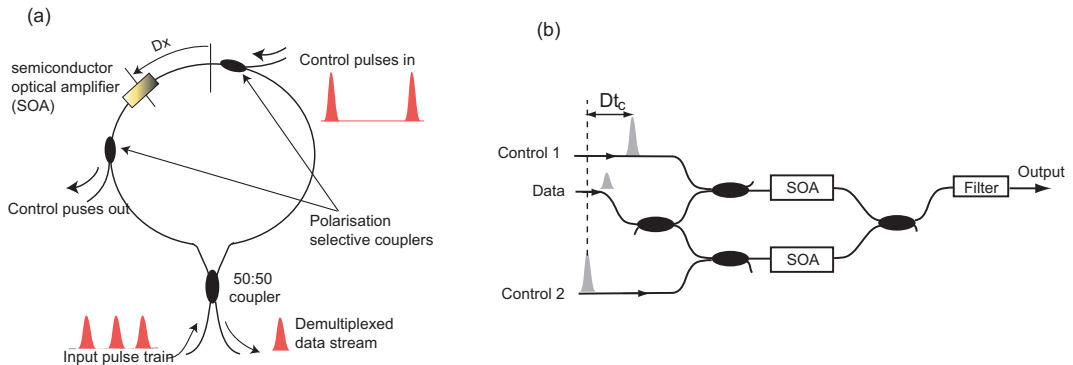


Figure 1.1: (a) A TOAD optical switch, using the non-linear phase change induced by strong optical pulses to infer an asymmetric phase change between counter propagating data pulses. (b) A Mach-Zehnder interferometer using the optically induced phase change in two optical amplifiers to achieve fast optical switching of data pulses.

Exploiting the large quadratic electro-optic effect due to the QCSE leads to a trade off in phase modulators. Large changes in the refractive index close to the bandedge involves

substantial losses due to electroabsorption. However, moving away from the resonance (detuning) increases the chirping parameter (ratio between the refractive index and absorption) [38], which is also detrimental for optical transmission. Phase modulators are typically characterised by the voltage required to achieve π phase-shift. For a quaternary (InGaAlAs) MQW (30 periods) waveguide device, typically $300\mu\text{m}$ in length. The approximate parameters could be; $V_\pi \approx 3.8\text{V}$, 3dB frequency response $\approx 18\text{GHz}$ with intensity modulation of 1.5dB, and fibre to fibre coupling loss of $\approx 9\text{dB}$.

The remaining section will discuss the issues of refractive index and dispersion when the oscillating dipoles interact with an electromagnetic wave. In addition nonlinear refraction due to intense pulse propagation will be discussed.

1.3 Optical propagation and dispersion

To understand the origin of dispersion we consider the fundamental interaction between the electric field (neglecting the magnetic field interactions for simplicity) and a dielectric media. The interaction for a plane wave is described by Maxwell's equation (1.3), where the polarisation (\mathbf{P}) quantifies the response of the material, in a classical sense, the perturbation of loosely bound electrons forming dipoles with their binding nucleus.

$$\Delta^2 \mathbf{E} = \mu \varepsilon_0 \frac{\partial^2 \mathbf{E}}{\partial t^2} + \mu \frac{\partial^2 \mathbf{P}}{\partial t^2}, \quad (1.3)$$

where, μ and ε_0 are the permeability and permittivity in free space respectively and \mathbf{E} is the electric field. For low to moderate light intensities, the polarisation has a linear relationship with \mathbf{E} , where the proportionality constant is known as the complex electrical susceptibility ($\chi(\omega)$). This fully describes the absorption, refraction and dispersion. In terms of more physically intuitive parameters we can write,

$$\left(\frac{\mathbf{k}(\omega)c}{\omega} \right)^2 = 1 + \chi(\omega) = 1 + \chi'(\omega) + i\chi''(\omega) \quad (1.4)$$

$$\left(\frac{\mathbf{k}(\omega)c}{\omega} \right) = n(\omega) = \eta(\omega) + i\kappa(\omega). \quad (1.5)$$

Where $\eta(\omega)$ is the real refractive index and determines the speed of light in the medium

by definition of the phase velocity ($v_{ph} = \omega/\mathbf{k}(\omega) = c/\eta(\omega)$), κ is the imaginary part of the complex refractive index and determines the magnitude of absorption ($\alpha = 2\omega\mathbf{k}(\omega)/c$) in Beer's law. The real and imaginary parts of the complex susceptibility are shown in figure 1.2, for a resonance centred at ω_0 . They are related to each other through the Kramers-Kronig dispersion relation which is covered in detail in Appendix A.

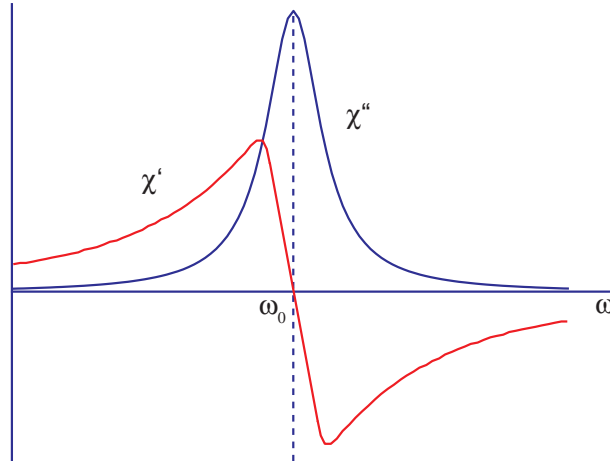


Figure 1.2: Real (χ') and imaginary (χ'') components of the susceptibility around a resonance centred at ω_0 .

The spectral phase ($\phi(\omega)$) accumulated after propagating a length L forms the origin of chirp and is given as,

$$\phi(\omega) = \frac{\omega\eta(\omega)}{c}L. \quad (1.6)$$

For the case of optical pulse propagation we can expand this phase transfer function around the carrier frequency (ω_0), in order to analyse the dispersive properties as follows,

$$\phi = \phi_0 + \frac{d\phi}{d\omega}[\omega - \omega_0] + \frac{d^2\phi}{d\omega^2} \frac{[\omega - \omega_0]^2}{2!} + \frac{d^3\phi}{d\omega^3} \frac{[\omega - \omega_0]^3}{3!} + \dots \quad (1.7)$$

The first term, ϕ_0 is simply a phase offset. The second term ($d\phi/d\omega$) is called group delay ($\tau_g = L(dk/d\omega)$) and is a measure of the overall time taken for the pulse to propagate through the medium at the group velocity ($v_g = d\omega/dk = L(d\omega/d\phi)$). The third term ($d^2\phi/d\omega^2$) is called group delay dispersion ($GDD = L(d^2k/d\omega^2)$) which is extremely important as it is the rate at which a pulse centred at the reference frequency will increase in duration as it propagates through the medium. Higher order terms lead to

the accumulation of more complex spectral phase. Under the influence of higher electric field intensities, the presence of higher order susceptibilities $\chi^{(2)}$ and $\chi^{(3)}$ can lead to the generation of new wavelengths, as covered in chapter 3.

1.4 Nonlinear refraction in active semiconductors

As mentioned previously the absorption (or gain in electrically pumped devices) and the refractive index are related. The absorption (or gain) is both carrier density and temperature dependent. The largest changes in the refractive index occur around the resonance of the bandgap and for energies above and near this energy, increasing the carrier density reduces the refractive index (and vice versa) [39]. When intense optical pulses such as the ones use in this thesis are present, the rapid changes in carrier density via band filling gives rise to an absorption change and the presence of nonlinear refraction. For the pulses used here (≈ 250 fs) the main effects are band filling and carrier heating. These changes in refractive index contribute to accumulation of spectral phase and in the worst case, pulse breakup. Although the linewidth enhancement factor is not investigated specifically in the work that follows it is an important parameter for real devices and is defined as, [40]

$$\alpha_N = -\frac{\partial\chi'/\partial N}{\partial\chi''/\partial N} = -\frac{4\pi}{\lambda} \frac{\partial\eta/\partial N}{\partial\alpha/\partial N}. \quad (1.8)$$

Where, χ' and χ'' are the real and imaginary parts of the complex susceptibility.

1.5 Summary

Current semiconductors that can be grown lattice matched to GaAs for wavelength emission at $1.3\mu\text{m}$ have been reviewed. This forms the basis of the work that is covered in the following thesis, investigating the nonlinear optical dynamics of the electrons close to the bandedge for some of these materials, with a view to applications in modulator devices. With this in mind, an overview of modulator fundamentals has been introduced and the subject of optical wave propagation, including dispersion in dielectric media has been covered.

References for Chapter 1

- [1] D I Babic, K Streubel, R P Mirin, N M Margalit, J E Bowers, E L Hu, D E Mars, L Yang, and L Carey. Room-temperature continuous-wave operation of $1.54\mu\text{m}$ vertical-cavity lasers. *IEEE Photon. Tech. Lett.*, 7:p1225–p1227, 1995.
- [2] T Ishikawa, T Higashi, T Uchida, T Yamamoto, T Fujji, H Shoji, M Kobayashi, and H Soda. Well-thickness dependence of high-temperature characteristics in $1.3\mu\text{m}$ AlGaInAs-InP strained-multiple-quantum-well lasers. *IEEE Photon. Tech. Lett.*, 10:p1703–p1705, 1998.
- [3] K Takemasa, T Munakata, M Kobayashi, H Wada, and T Kamijoh. High-temperature operation of $1.3\mu\text{m}$ AlGaInAs strained multiple quantum well lasers. *Elect. Lett.*, 34:p1231–p1233, 1998.
- [4] A Caliman, E Kapon, and A Mereuta. $1.3\mu\text{m}$ and $1.55\mu\text{m}$ wavelength wafer fused InAlGaAs/InP-AlGaAs/GaAs VCSEL's with high single mode output power. *CLEO Europe 2007*, 2007.
- [5] Markus Weyers and Michio Sato. Growth of GaAsN alloys by low-pressure metalorganic chemical vapor deposition using plasma-cracked NH_3 . *Applied Physics Letters*, 62(12):1396–1398, 1993.
- [6] M Kondow, K Uomi, A Niwa, T Kitatani, S Watahiki, and Y Yazawa. GaInNAs: A novel material for long wavelength range laser diodes with excellent high-temperature performance.
- [7] K Nakahara, M Kondow, T Kitatani, M C Larson, and K Uomi. $1.3\mu\text{m}$ continuous-wave lasing operation in GaInNAs quantum-well lasers. *IEEE Phot. Tech. Lett.*, 10:p487–p488, 1998.
- [8] T Kitatani, K Nakahara, M Kondow, K Uomi, and T Tanara. A $1.3\mu\text{m}$ GaInNAs/GaAs Single-Quantum-Well Laser Diode with a High Characteristic Temperature over 200K. *Japan. J. App. Phys.*, 39:L86–7, 2000.
- [9] A Yu Egorov, D Bernklau, D Livshits, V Ustinov, Zh I Alferov, and H Riechert. High power cw operation of ingaasn lasers at $1.3\mu\text{m}$. *Elect. Lett.*, 35(19):1643, 1999.
- [10] S Tomic, E P O'Rielly, R Fehse, S J Sweeney, A R Adams, A D Andreev, S A Choulis, T J C Hosea, and H Riechert. Theoretical and experimental analysis of $1.3\mu\text{m}$ InGaAsN/GaAs lasers. *IEEE J. Sel. Top. Quan. Elec.*, 9:p1228, 2003.
- [11] M Yamada, T Anan, H Hatakeyama, K Tokutome, N Suzuki, T Nakamura, and K Nishi. Low-threshold operation of $1.34\mu\text{m}$ GaInNAs VCSEL grown by MOVPE. *Phot. Tech. Lett.*, 17(5):p950–p952, 2005.
- [12] M Yamada, T Anan, K Tokutome, K Nishi, A Gomyo, and S Sugou. Low-threshold lasing at $1.3\mu\text{m}$ from GaAsSb quantum wells directly grown on GaAs substrates. *Proc. Conf. LEOS '98 (Orlando 1998)*, pages p149–p150, 1998.
- [13] Prins, A. D. and Dunstan, D. J. and Lambkin, J. D. and O'Reilly, E. P. and Adams, A. R. and Pritchard, R. and Truscott, W. S. and Singer, K. E. Evidence of type-I band offsets in strained $\text{GaAs}_{1-x}\text{Sb}_x/\text{GaAs}$ quantum wells from high-pressure photoluminescence. *Phys. Rev. B*, 47(4):2191–2196, Jan 1993.
- [14] K. Hild, S. J. Sweeney, S. Wright, D. A. Lock, S. R. Jin, I. P. Marko, S. R. Johnson, S. A. Charro, S.-Q. Yu, and Y.-H. Zhang. Carrier recombination in $1.3\mu\text{m}$ GaAsSb/GaAs quantum well lasers. *Applied Physics Letters*, 89(17):173509, 2006.
- [15] M Rattunde, N Schulz, C Ritzenthaler, B Rosener, C Manz, L Kohler, and J Wagner. High power, high brightness tuneable GaSb based VECSEL at $2.3\mu\text{m}$. *CLEO Europe 2007 June 17-22nd*, 2007.
- [16] I N Stranski and L Krastanow. Sitzungsberichte d. Akad. d. *Wissenschaften in Wien, Abt. IIb*, Band 146:pp797, 1937.
- [17] K Mukai, N Ohtsuka, M Sugawara, and S Yamazaki. Self-Formed $\text{In}_{0.5}\text{Ga}_{0.5}\text{As}$ Quantum Dots on GaAs Substrates Emitting at $1.3\mu\text{m}$. *Jap. J. Appl. Phys.*, 33:L1710–L1712, 1994.

- [18] R. P. Mirin, J. P. Ibbetson, K. Nishi, A. C. Gossard, and J. E. Bowers. $1.3\mu\text{m}$ photoluminescence from InGaAs quantum dots on GaAs. *App. Phys. Lett.*, 67(25):3795–3797, 1995.
- [19] D. L. Huffaker, G. Park, Z. Zou, O. B. Shchekin, and D. G. Deppe. $1.3\mu\text{m}$ room-temperature GaAs-based quantum-dot laser. *Applied Physics Letters*, 73(18):2564–2566, 1998.
- [20] Hideaki Saito, Kenichi Nishi, and Shigeo Sugou. Influence of GaAs capping on the optical properties of InGaAs/GaAs surface quantum dots with $1.5\mu\text{m}$ emission. *Applied Physics Letters*, 73(19):2742–2744, 1998.
- [21] V. M. Ustinov, N. A. Maleev, A. E. Zhukov, A. R. Kovsh, A. Yu. Egorov, A. V. Lunev, B. V. Volovik, I. L. Krestnikov, Yu. G. Musikhin, N. A. Bert, P. S. Kop'ev, Zh. I. Alferov, N. N. Ledentsov, and D. Bimberg. InAs/InGaAs quantum dot structures on GaAs substrates emitting at $1.3\mu\text{m}$. *Applied Physics Letters*, 74(19):2815–2817, 1999.
- [22] L F Lester, A Stintz, H Li, T C Newell, E A Pease, B A Fuchs, and K J Malloy. Optical characteristics of $1.24\mu\text{m}$ InAs quantum-dot laser diodes. *Photonics Technology Letters*, 11(8):p931–p933, 1999.
- [23] Xiaodong Huang, A. Stintz, C.P. Hains, G.T. Liu, J. Cheng, and K.J. Malloy. Efficient high-temperature CW lasing operation of oxide-confined long-wavelength InAs quantum dot lasers. *Electronics Letters*, 36(1):41–42, 2000.
- [24] Lui H Y, Sellers I R, Gutierrez M, Groom K M, Beanland R, Soong W M, Hopkinson M, David J P R, Badcock T J, Mowbray D J, and Skolnick M S. Optimizing the growth of $1.3\mu\text{m}$ InAs/InGaAs dots-in-a-well structure: Achievement of high-performance laser. *Mat. Sci. and Eng. C*, 25:p779–p783, 2005.
- [25] A. E. Zhukov, A. R. Kovsh, N. A. Maleev, S. S. Mikhrin, V. M. Ustinov, A. F. Tsatsul'nikov, M. V. Maximov, B. V. Volovik, D. A. Bedarev, Yu. M. Shernyakov, P. S. Kop'ev, Zh. I. Alferov, N. N. Ledentsov, and D. Bimberg. Long-wavelength lasing from multiply stacked inas/ingaas quantum dots on gaas substrates. *Applied Physics Letters*, 75(13):1926–1928, 1999.
- [26] D Schlenker, T Miyamoto, Z Chen, F Koyama, and K Iga. $1.17\mu\text{m}$ highly strained GaInAs-GaAs quantum-well laser. *Phot. Tech. Lett.*, 11:p946–p948, 1999.
- [27] Naresh Chand, E. E. Becker, J. P. van der Ziel, S. N. G. Chu, and N. K. Dutta. Excellent uniformity and very low (50 Acm^{-2}) threshold current density strained InGaAs quantum well diode lasers on GaAs substrate. *Applied Physics Letters*, 58(16):1704–1706, 1991.
- [28] F. Koyama, D. Schlenker, T. Miyamoto, Z. Chen, A. Matsutani, T. Sakaguchi, and K. Iga. $1.2\mu\text{m}$ highly strained GaInAs/GaAs quantum well lasers for singlemode fibre datalink. *Electronics Letters*, 35(13):1079–1081, 1999.
- [29] F. K. Reinhart. Electroabsorption in $\text{Al}_y\text{Ga}_{1-y}\text{As} - \text{Al}_x\text{Ga}_{1-x}\text{As}$ double heterostructures. *Applied Physics Letters*, 22(8):372–374, 1973.
- [30] K Tada and K Hirose. A new light modulator using perturbation of synchronism between two coupled guides. *Applied Physics Letters*, 25(10):561–562, 1974.
- [31] K Wakita. *Semiconductor Optical Modulators*. Kluwer Academic Publishers, 1998.
- [32] Y. Noda, M. Suzuki, Y. Kushiro, and S. Akiba. 1.6 GHz electroabsorption light modulation in InGaAsP/InP double heterostructures with strip-loaded planar waveguide.
- [33] D. A. B. Miller, D. S. Chemla, T. C. Damen, A. C. Gossard, W. Wiegmann, T. H. Wood, and C. A. Burrus. Band-edge electroabsorption in quantum well structures: The quantum-confined stark effect. *Phys. Rev. Lett.*, 53(22):2173–2176, Nov 1984.
- [34] D. A. B. Miller, D. S. Chemla, and S. Schmitt-Rink. Relation between electroabsorption in bulk semiconductors and in quantum wells: The quantum-confined franz-keldysh effect. *Phys. Rev. B*, 33(10):6976–6982, May 1986.
- [35] C Kittel. *Introduction to solid state physics*. Wiley, 7th edition, 1995.

- [36] J P Sokoloff, P R Prucnal, I Glesk, and M Kane. A terahertz optical asymmetric demultiplexer (TOAD). *IEEE Photon. Technol. Lett.*, 5(7):787, 1993.
- [37] R Schrieck, M Kwakernaak, H Jckel, E Gamper, E Gini, W Vogt, and H Melchior. Ultrafast switching dynamics of Mach-Zehnder interferometric switches. *IEEE J. Quantum Electron.*, 37(6):603–605, 2001.
- [38] J E Zucker, T L Hendrickson, and C A Burrus. Electro-optic phase modulation in GaAs/AlGaAs quantum well waveguides. *Appl. Phys. Lett.*, 52(12):945–947, 1988.
- [39] C H Henry, R A Logan, and K A Bertness. Spectral dependence of the change in refractive index due to carrier injection in AlGaAs lasers. *J. Appl. Phys.*, 52(7):4457–4461, 1981.
- [40] C H Henry. Theory of the linewidth enhancement factor. *IEEE J. Quantum Electron.*, 18(2):259–264, 1982.

Chapter 2

Optical properties of semiconductor heterostructures

This chapter outlines the optical and electronic properties of quantum confined GaAs based heterostructures, which will form the basis for understanding the experimental work of the following chapters. Using sophisticated growth techniques such as Metal Organic Chemical Vapour Deposition (MOCVD) and Molecular Beam Epitaxy (MBE) capable of depositing single layers of atoms, it has become possible to grow structures with physical confinement on the order of the de Broglie wavelength of electrons.

The following discussion will focus on the GaInNAs quantum well and InAs-InGaAs quantum dot material systems.

2.1 Bulk III-V compound semiconductors

Of the 14 general types of crystal lattice, III-V compound semiconductors are formed by two interpenetrating face-centred cubes (fcc), giving a diamond (zinc-blende) structure. The basis consists of one atom at each lattice site and a second atom displaced one quarter of a cube length ($a/4$) in each of the 3 dimensions. This forms a series of basic cubes of side $a/2$ where the four atoms at alternative corners of the basic cube are at the corners of a regular tetrahedron. This translates through the whole structure so that each atom at the centre of the diamond structure is the centre of a tetrahedron with four nearest neighbouring atoms.

Consequently this gives rise to four covalent bonds involving 8 outer most electrons, 3 from one element and 5 from the other. The 8 electrons form bonding and anti-bonding levels, an s -type and 3 p -type in each set. Of the bonding levels, the lowest s -type contains 2 electrons, whilst at 0K the other 6 electrons completely fill the 3 p -type bonding levels (known as the valence bands). The lowest s -type orbital of the anti-bonding set is known as the conduction band.

Energy Bands

The introduction of the term 'bands' is due to the collective nature of many atoms with discrete levels as explained above, coming together to form the crystalline solid. Applying the exclusion principle to an entire system of N closely spaced atoms, then allows each valence electron state to split into a band containing N closely spaced levels. As N is large the levels can be thought as forming a continuous distribution of energies within the band. This introduces the idea of dispersion, where electrons can occupy the same energy level but have a different wavevector (\mathbf{k}) related to their particle momentum $\mathbf{p} = \hbar\mathbf{k}$. The semiconductors used in this thesis are 'direct' band, whereby the band extrema occur at the same point in k -space. The point at which $k = 0$ is known as the Brillouin zone centre (Γ) and at this point the degeneracy of the 3 valence bands is lifted due to the spin-orbit coupling of the electron and the atomic nucleus interaction. This gives rise to angular momentum states comprising a quadruplet ($J=3/2$) and a doublet ($J=1/2$), relative to $L=0$ (s -level) and $L=1$ (p level). The split-off band can be neglected if the splitting is large, however this does not apply to materials with low atomic mass such as silicon ($\Delta = 0.044eV$) as the splitting is proportional to the fourth power of atomic mass. Figure 2.1 explains pictorially many of the concepts above.

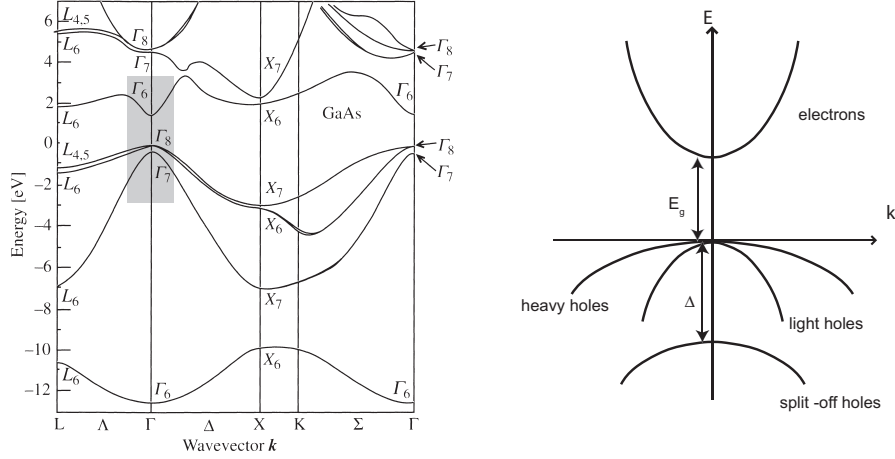


Figure 2.1: (a) Electronic pseudopotential band structure of GaAs. (b) Band structure of a bulk direct bandgap semiconductor in the parabolic approximation. Reproduced from reference [1]

The actual dispersion relation as depicted in the figure above is what defines the band structure. The wavefunction for a free particle in a vacuum is a plane wave $\exp(i\mathbf{k} \cdot \mathbf{r})$, where the energy of the particle is defined as $E = \mathbf{p}^2/2m = \hbar^2\mathbf{k}^2/2m$, m is the mass of the particle. However in a periodic crystal structure an averaged periodic potential $U(r)$ is assumed and used to solve the Schrodinger equation. This yields wavefunctions similar to that of the free particle except for an additional term which has the periodicity of the lattice $u_{\mathbf{k}}(\mathbf{r})$. These corresponding wavefunctions are known as Bloch waves.

$$\psi_{\mathbf{k}}(\mathbf{r}) = u_{\mathbf{k}}(\mathbf{r})\exp(i\mathbf{k} \cdot \mathbf{r}) \quad (2.1)$$

As for individual atomic energy levels there are forbidden regions between the bands (band gaps) where the Bloch functions of the electrons cannot exist.

At absolute zero semiconductors fill the valence band completely as mentioned above. The next available band is the the empty conduction band and is typically a few electron volts in energy separation. It is the nature of these bands that determines whether the material is an insulator or a semiconductor.

Density of states and the Fermi distribution

To calculate the number of states that exist in a particular energy band we can think of a sphere in k -space, where the radial coordinate determines the carrier states n . Now

we are only interested in k states that are positive and that can each accommodate two electrons, due to the spin dependency ($m_s = \pm 1/2$). With this in mind we can define the total number of states enclosed in $1/8$ of the volume of a sphere,

$$N = 2 \cdot \frac{1}{8} \cdot \frac{4}{3}\pi n^3 = \frac{\pi n^3}{3}. \quad (2.2)$$

We recall that \mathbf{k} is quantised in the dispersion relation as $\mathbf{k} = n\pi/L$ which corresponds to a discrete energy (E) for each state as,

$$E = \frac{\hbar^2 k^2}{2m} = \frac{\hbar^2 \pi^2 n^2}{2mL^2}. \quad (2.3)$$

Thus we can now write the relationship between N and E as below,

$$N = \frac{(2m)^{3/2} L^3 E^{3/2}}{3\pi^2 \hbar^3}. \quad (2.4)$$

The density of states (DOS) is defined as the number of individual states that exist between energy E and $E+dE$,

$$g(E) = \frac{dN}{dE} = \frac{(2m^{3/2})VE^{1/2}}{2\pi^2 \hbar^3}, \quad (2.5)$$

where V is the volume.

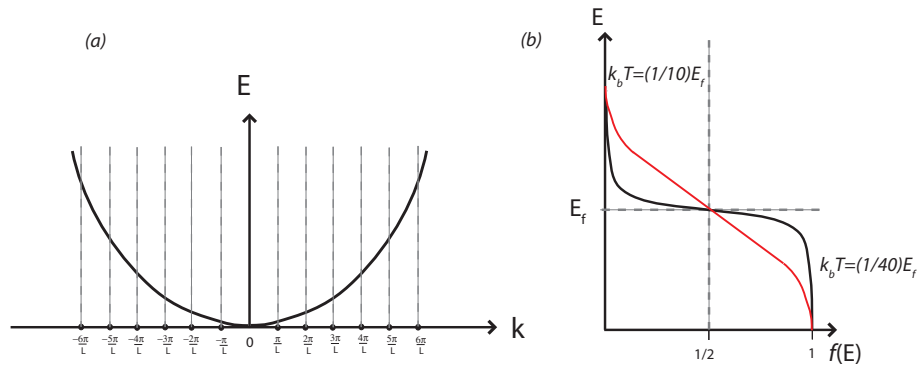


Figure 2.2: (a) Band structure of a 1D crystal in the extended zone scheme where the parabola indicates $E(k)$. (b) Fermi-dirac distribution for electrons showing the occupation probability for elevated temperature as a ratio of the fermi energy E_f . Reproduced from reference [2]

We now need to consider the occupation probability of the individual states over a range

of temperatures. Two factors mean that we cannot simply use the Maxwell-Boltzmann distribution. Firstly, the exclusion principle states that each state can only accommodate one particle. Secondly, we have an indistinguishability between identical particles. A solution to this statistical problem is the Fermi-Dirac distribution which is given below, where the Fermi level (E_f) is defined as the energy where the occupation probability is 1/2,

$$f(E) = \frac{1}{e^{(E-E_f)/k_bT} + 1}. \quad (2.6)$$

When E is much smaller than E_f the probability approaches unity. The shape is determined by the ratio of E_f/k_bT and as k_bT approaches E_f the probability rapidly falls as carriers are thermally liberated from the lowest laying states.

To calculate the total number of charge carriers we have to multiply the DOS by the probability distribution given by Fermi-Dirac and integrate over the energy interval. This gives the following for the electrons and holes,

$$n_{3d} = \int_{E_g}^{\infty} g_c(E)f(E)dE \quad (2.7)$$

$$p_{3d} = \int_0^{-\infty} g_v(E)[1 - f(E)]dE. \quad (2.8)$$

In the case of $E \gg E_f$ the fermi distribution can be approximated via the Boltzmann distribution and we find the following analytical solutions for the electron and hole densities,

$$n_{3d} = N_c \exp\left(-\frac{E_g - E_f}{k_bT}\right) = 2 \left(\frac{2m_e^* k_bT}{\pi \hbar^2}\right)^{3/2} \exp\left(-\frac{E_g - E_f}{k_bT}\right) \quad (2.9)$$

$$p_{3d} = N_v \exp\left(-\frac{E_f}{k_bT}\right) = 2 \left(\frac{2m_h^* k_bT}{\pi \hbar^2}\right)^{3/2} \exp\left(-\frac{E_f}{k_bT}\right). \quad (2.10)$$

Where, N_c and N_v are prefactors for the conduction and valance band densities, that depend on the electron and hole effective masses respectively. At low temperature we know that all states below E_f are occupied and we can use equation 2.4 to relate the

Fermi energy to the carrier density directly,

$$E_F = \frac{3^{2/3} \pi^{4/3} \hbar^2 n^{2/3}}{2m}. \quad (2.11)$$

Such carrier density can be changed via current injection or by adding impurities to increase the electron or hole concentration, as will be seen later. At high enough carrier concentrations the Fermi level can exist above conduction band.

2.2 Low dimensional effects: The quantum well

With the development of sophisticated techniques such as Metal-Organic Chemical Vapour Deposition (MOCVD) and Molecular Beam Epitaxy (MBE), it has become possible to grow compound semiconductors on the scale of the atomic layer. This allows the creation of periodic potentials within the crystal structure on the scale of the de Broglie wavelength of electrons and holes. The quantum well is a structure which has such potential confinement in the growth direction. In the same way as bands form by the Bloch waves in a 3D periodic crystal, the same thing happens in a quantum well. However in the simplest form (Type I) as shown in figure (2.3(b)), \mathbf{k}_z is quantized by sandwiching a narrow bandgap material in between two larger bandgap materials. The energy levels describing the motion of carriers in the growth direction become discrete, whilst \mathbf{k}_x and \mathbf{k}_y are still defined by the long range order of the periodic crystal. These heterostructures became popular for dramatically improving the efficiency of laser structures due to electrons and holes being less inclined to drift away from the junction.

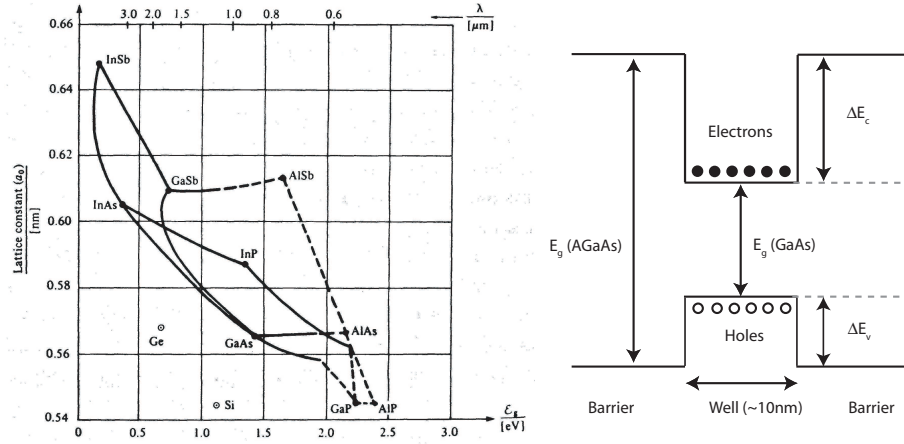


Figure 2.3: (a) Lattice constant for various semiconductors against their minimum band gap E_g , in eV and wavelength (solid lines indicate direct band transitions, dashed lines indicate indirect transitions) reproduced from [3]. (b) Formation of a type I quantum well using two semiconductor materials with differing band gap.

2.2.1 Quantum confinement energy

As mentioned previously, the Bloch waves that can propagate freely throughout a crystal lattice form bands due to the interaction with the periodic potential. The quantum well can be thought of as a finite crystal where an artificial potential has been introduced (between the barriers) over a distance L . The momentum \mathbf{k}_z vector is now quantized as $\mathbf{k}_z = n\pi/L$. Due to this confinement there is an increase in the ground state energy of the particle relative to the unconfined case, due to Heisenberg's uncertainty principle. This is due to the uncertainty of the particles momentum and hence the energy.

$$\Delta E = \frac{p(\Delta p)}{2m^*} \quad (2.12)$$

To describe the confinement we can introduce the approximation of an envelope function $\psi_n(z)$ which modulates the Bloch waves of the lattice and defines each subband, having a total wavefunction,

$$\Psi_n = \psi_n(z)u_{n,0}(\mathbf{r}) \exp(i\mathbf{K} \cdot \mathbf{R}). \quad (2.13)$$

We can solve the envelope functions with the time independent Schrodinger equation (2.14). Thus yielding the eigenenergies for the ground and excited state subbands at $\mathbf{k} = 0$.

$$\left[-\frac{d}{dz} \frac{\hbar^2}{2m_z^*(z)} \frac{d}{dz} + V(z) \right] \psi_n(z) = E_n \psi_n(z) \quad (2.14)$$

where m_z^* is electron effective mass in the z direction and E_n is the subband energy for the n th level. If the potential in equation 2.14 is zero within the well and infinite elsewhere then the wavefunctions are zero everywhere except inside the well. The normalized solutions for $\psi_n(z)$ and E_n inside the well are given as,

$$\psi_n(z) = \sqrt{\frac{2}{L}} \cos\left(\frac{n\pi z}{L}\right) \quad \text{for odd } n \quad (2.15)$$

$$\psi_n(z) = \sqrt{\frac{2}{L}} \sin\left(\frac{n\pi z}{L}\right) \quad \text{for even } n \quad (2.16)$$

and

$$E_n(z) = \frac{\hbar^2}{2m_w^*} \left(\frac{n\pi}{L}\right)^2 \quad \text{for all } n. \quad (2.17)$$

The subscript n denotes the subband number to differentiate it from the unconfined case. In a real quantum well however the potential is finite as depicted in figure 2.3. Due to the symmetry of the problem the solutions are still odd or even, although the wavefunctions can penetrate into the barrier material and the momentum vector \mathbf{k} is modified depending on where the particle exists.

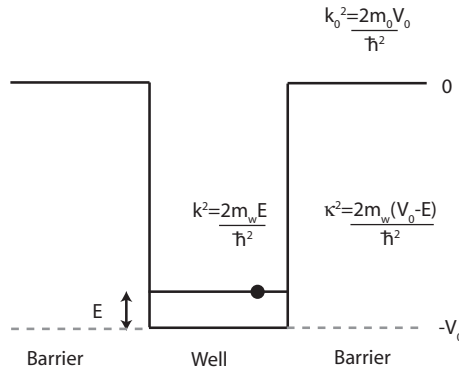


Figure 2.4: type I quantum well showing the momentum vector relating to different regions

The wavefunctions inside the barrier are decaying exponentials. If we consider the odd solution first, with the wave propagating to the right and apply the continuity condition to $\psi_n(z)$, we have the following,

$$C \cos\left(\frac{kL}{2}\right) = C' \exp\left(-\frac{\kappa L}{2}\right). \quad (2.18)$$

Note that the effective particle mass changes due to the material difference between the well and the barrier and the particle flux ($m^{*-1}d\psi/dz$) must also be continuous across the boundary, therefore,

$$-C \frac{k}{m_w^*} \sin\left(\frac{kL}{2}\right) = C' \frac{\kappa}{m_b^*} \exp\left(-\frac{\kappa L}{2}\right). \quad (2.19)$$

Upon dividing equation 2.19 by equation 2.18, we find,

$$\tan\left(\frac{kL}{2}\right) = \frac{m_w^* \kappa}{m_b^* k}. \quad (2.20)$$

Carrying out a similar analysis on the even solutions yields,

$$\cot\left(\frac{kL}{2}\right) = -\frac{m_w^* \kappa}{m_b^* k}. \quad (2.21)$$

To obtain the eigenenergies from equation 2.20 and equation 2.21 we have to solve them numerically or graphically. From inspection of figure 2.4 we can find a third equation relating the momentum vectors as,

$$\frac{m_w^*}{m_b^*} \sqrt{\frac{k_0^2}{k^2} - 1} = \frac{\kappa}{k}. \quad (2.22)$$

From these three equations we can find the eigenenergies for the subbands at $k = 0$ for $n = 1, 2, 3, \dots$ as shown below. Note that states above the confining potential extend into the 3D continuum [4].

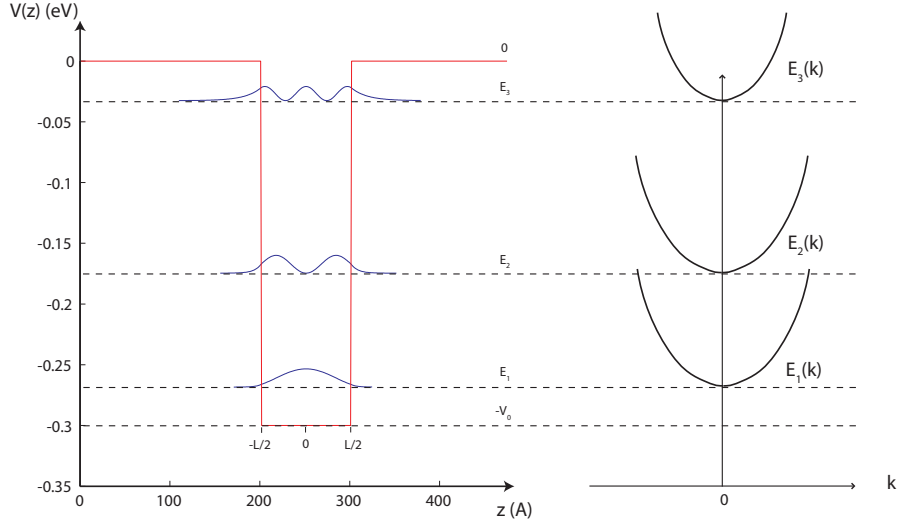


Figure 2.5: Numerical solution to Schrodinger equation for a quantum well with finite potential. The well consists of 10nm of GaAs and the barrier material is $Al_{0.4}Ga_{0.6}As$. Also drawn are the subbands which have the energy minimum defined by the confinement in the growth direct, whilst the dispersion relation in k_x and k_y remains.

2D Density of states

Keeping with the description of states in a sphere of k -space, we can write the 2D density of states as,

$$N_{2d}(k)\delta k = 2\frac{L}{2\pi}k\delta k, \quad (2.23)$$

where $L/2\pi$ is the density of points and k is fixed in one dimension, whilst the 2 corresponds to spin up and down states. Now E and k are linked via the dispersion relation,

$$\frac{dk}{dE}\delta E = \delta k = \frac{m}{\hbar^2 k}, \quad (2.24)$$

where,

$$N_{2d}(k)\delta k = N_{2d}(E)\delta E. \quad (2.25)$$

We can now write the density of states in energy space as follows,

$$n_{2d}(E) = \frac{m^*}{\hbar^2 \pi} \sum_{n=1}^{\infty} \theta(E - E_n). \quad (2.26)$$

In the above expression $\theta(E - E_n)$ is a step function also referred to as the Heaviside function [4]. These steps in energy correspond to the bound states of the potential well as shown in figure 2.5. In figure 2.6 a comparison of the density of states for bulk, quantum wells and quantum dots can be seen. In the latter case the 3D confinement gives rise to atomic like orbitals which in practice are inhomogeneously broadened due to the size distribution dictated by growth.

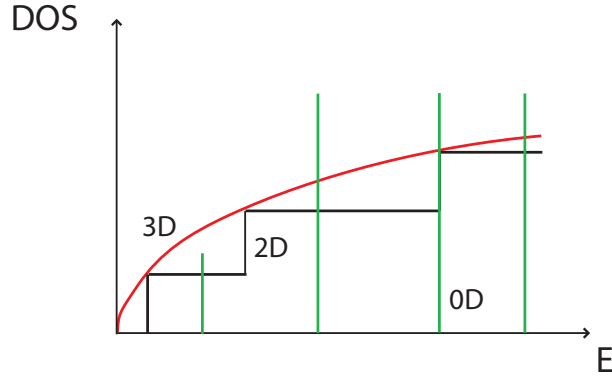


Figure 2.6: Density of states for bulk (3D), quantum well (2D) and quantum dot (0D).

Quantization of holes

As mentioned previously the valence bands take the form of p-type orbitals. These bands mix in a complex manner due to their small separation and the valence band properties need to be described by numerical calculations, using degenerate perturbation theory (such as $\mathbf{k}\cdot\mathbf{p}$) in bulk semiconductors. Using a multiband effective mass approximation the Hamiltonian is,

$$\sum_{\mu} [H_{\mu}(k) + V(z)\delta_{\mu}] \psi_n^{\mu} = E_n \psi_n^{\mu}. \quad (2.27)$$

Dealing with the top two valence bands which are degenerate at $k=0$, these are $m_j = \pm\frac{3}{2}$ (heavy) and $m_j = \pm\frac{1}{2}$ (light). The corresponding heavy hole and light hole Luttinger Hamiltonians are,

$$H_{hh} = \frac{\hbar^2 k_z^2}{2m_0}(\gamma_1 - 2\gamma_2) + \frac{\hbar^2(k_x^2 + k_y^2)}{2m_0}(\gamma_1 + \gamma_2) \quad (2.28)$$

$$H_{lh} = \frac{\hbar^2 k_z^2}{2m_0}(\gamma_1 + 2\gamma_2) + \frac{\hbar^2(k_x^2 + k_y^2)}{2m_0}(\gamma_1 - \gamma_2). \quad (2.29)$$

In the above expressions, γ_1 and γ_2 are the experimentally determined Luttinger parameters which are related to the dipole matrix elements for transitions ($\gamma_1 > \gamma_2$ in typical zinc blend compounds). The solution of these equations give the following masses,

$$m_{hhz} = \frac{m_0}{\gamma_1 - 2\gamma_2} \quad (2.30)$$

$$m_{lhz} = \frac{m_0}{\gamma_1 + 2\gamma_2}. \quad (2.31)$$

The quantum confinement in wells leads to a mixing of the light and heavy hole bands, which can be accounted for in $\mathbf{k}\cdot\mathbf{p}$ theory. This mixing results in the formation of highly non-parabolic bands [5], as shown in figure 2.7.

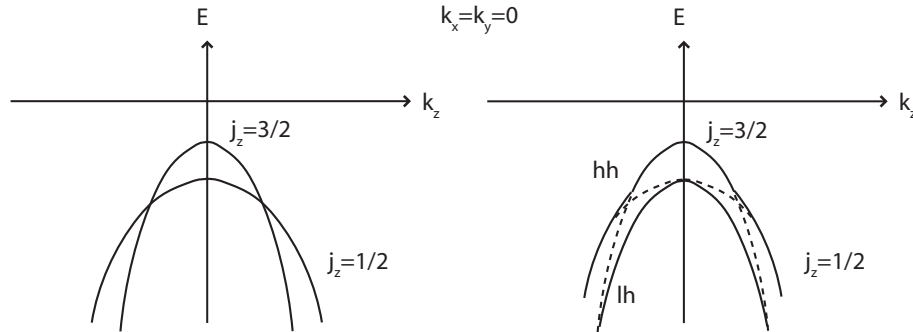


Figure 2.7: Dispersion of the $J_z=3/2$ and $J_z=1/2$ bands in a quantum well showing the effect of band anticrossing, leading to the formation of the heavy hole (hh) and light hole (lh) valence bands.

2.2.2 Optical transitions

Transitions between different states in a quantum well give rise to absorption. The basis of this is the introduction of a time dependent perturbation to the Hamiltonian of the Schrodinger equation, which arises from the interaction with an incoming sinusoidal electromagnetic wave. Three types of transition can occur: (1) An interband transition

involving the promotion of a valence subband electron to a conduction subband; (2) an intersubband transition where an electron moves from one subband to another subband the same band; (3) an intrasubband transition where an electron is promoted to another K state within the same subband denoted by the integer n . This later case is the subject of optical nonlinearities, however we will first outline the interband transitions.

We assume a dipole for the interaction between the optical field and the carriers, defined as $V(\mathbf{r}, t) = -e \cdot \mathbf{r} \cdot \mathbf{E}$, where \mathbf{E} is the electromagnetic wave, $\mathbf{E}(\mathbf{r}, t) = \mathbf{E}_q \cos(\mathbf{q} \cdot \mathbf{r} - \omega t)$. Within the envelope approximation we can define the transition rate from a state in the valence band (Ψ_{nK}^v) to a state in the conduction band ($\Psi_{mK'}^c$) by Fermi's golden rule as [6],

$$S(n\mathbf{K} \rightarrow m\mathbf{K}') = \frac{\pi e^2}{2\hbar} |\mathbf{E}_q \cdot \mathbf{r}_{cv}|^2 |\langle m, c | n, v \rangle|^2 \delta(E_s - \hbar\omega) \Delta_{\mathbf{K}\mathbf{K}'}. \quad (2.32)$$

Where, \mathbf{r}_{cv} is the matrix element of the \mathbf{r} between the bloch functions of the bulk valence and conduction bands at $\mathbf{k}=0$. The product of the following two terms give the dipolar matrix element of the interband transition. The wavevector of incoming radiation ($\mathbf{k} = 2\pi/\lambda$) is much smaller than \mathbf{K} and \mathbf{K}' , and the conservation of momentum is given by $\mathbf{K} \approx \mathbf{K}'$, hence the Kronecker delta $\Delta_{\mathbf{K}\mathbf{K}'}$ in equation 2.32. The conservation of energy is evident in the equation where E_s is the \mathbf{K} -dependent energy separation between initial and final states as follows,

$$E_s = E - E_g + E_m^c + \frac{\hbar^2 \mathbf{K}^2}{2m_c^*} + E_n^v + \frac{\hbar^2 \mathbf{K}^2}{2m_v^*}. \quad (2.33)$$

There is also a threshold condition of $E_g + E_m^c + E_n^v$ which must be fulfilled in order for a photon to instigate such a transition $n \rightarrow m$.

Furthermore the overlap element $\langle n, v | m, c \rangle$ in equation 2.32 gives rise to the concept of selection rules. In the case of the infinite well the overlap is unity for states of equal indices and otherwise zero, due to the orthogonality of states, which gives the selection rule $m = n$. In the case of finite wells, decay constants in the barriers are different for electrons and holes and the envelope functions may not be 100% orthogonal. Transitions between $m \neq n$ subbands may therefore occur with finite probability. Figure 2.8 summarises the situation of TE and TM polarised light interacting with a quantum well. It can be

shown that transitions between heavy hole and electron subbands are forbidden for TM polarised light, while TE polarised light can induce transitions from both light and heavy hole subbands into electron subbands.

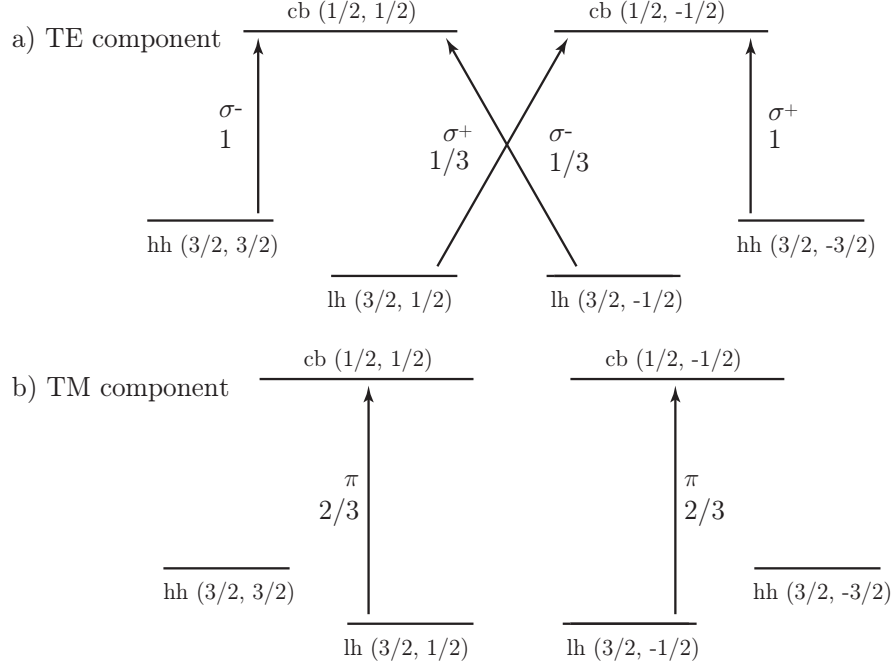


Figure 2.8: Summary of polarisation selection rules for light propagating parallel to the GaAs QW layers. π denotes light with linear polarisation and σ^+ and σ^- are right and left circularly polarised light, which themselves are combinations of linear polarisation. (a) For TE polarised light and (b) TM polarised light.

A final point to note is that in a real system there is a homogeneous broadening of the delta dirac function in equation 2.32. This is caused predominantly by intraband relaxation processes such as carrier-carrier and carrier-phonon scattering [7] and the lineshape is usually approximated by a Lorentzian function. In addition there is a component of the broadening for quantum confined systems attributed to inhomogeneous effects. These are typically variations in barrier/well thickness, localised strain, and impurities. In the case of quantum dots the fluctuation in the size distribution contributes significantly to this line broadening.

Absorption

When incident light causes optical interband transitions, photons are absorbed and carriers generated. When electrons are already present in the conduction band, then this can lead to the emission of photons via stimulated emission with subsequent carrier recombination. In the case of absorption, the net absorption rate is related to the transition probability via the imaginary part of the optical susceptibility. For the simplest case of bulk material the absorption is given as [6],

$$\alpha(\omega) = \frac{\pi e^2 x_{cv}^2 \omega}{\epsilon_0 \hbar n c} \rho_j(\omega) [f_v(\hbar\omega) - f_c(\hbar\omega)]. \quad (2.34)$$

Where, x_{cv} is the optical dipole matrix element of the transition and ρ_j is the 3D density of states. For the case of quantum wells this expression can be modified taking into account quantization effects to the dipole matrix element and the change in the density of states as follows,

$$\alpha_{QW}(\omega) = \sum_{n,m} \alpha_{QW}^{n \rightarrow m} \theta(\hbar\omega - E_g - E_m^c - E_n^v) [f_v(\hbar\omega) - f_c(\hbar\omega)]. \quad (2.35)$$

Where the sum includes contributions from all the available subbands in both the valence (n) and conduction (m) bands. f_c and f_v are the occupation probabilities in the conduction and valence bands and are given by the quasi-equilibrium Fermi functions, which depend on the quasi-Fermi levels for conduction (E_{F_c}) and valence (E_{F_v}) bands. The actual absorption coefficient is expressed as

$$\alpha_{QW}^{n \rightarrow m} = \frac{m_r^*}{\hbar^3} \hbar\omega \frac{(\mu_0/\epsilon_0)^{1/2}}{n(\omega)} |\eta_{\mathbf{q}} \cdot \mathbf{r}_{c\mathbf{v}}|^2 |\langle m, c | n, v \rangle|^2, \quad (2.36)$$

where, $\eta_{\mathbf{q}}$ indicates the polarisation of the optical field. This in turn changes the gain/absorption characteristics via the polarisation selection rules mentioned earlier. There is an inequality known as the Bernard-Durrafour condition, which states that for a photon to be amplified (experience gain) it must have energy greater than the bandgap but smaller than the difference between the quasi-Fermi levels. If the energy exceeds this then it will experience absorption higher in the bandstructure.

Excitons

Interband transitions from the absorption of photons creates an electron and hole in the conduction and valance band respectively. The coulomb interaction between these two particles gives rise to correlation of their motion and the bound pair is known as an exciton. In typical narrow bandgap semiconductors the coulombic interaction is screened by the valance band electrons and this leads to a weakly bound exciton (Wannier-Mott exciton) [1]. The motion can be decomposed into a centre of mass motion about a common mass behaving as a free particle ($M=m_e^* + m_h^*$). The relative motion is similar to that of a hydrogen atom and gives rise to bound states with principle quantum numbers $n=1,2,3$, etc. In addition, continuum states exist as those for free electrons and holes however their wavefunctions are still modified by the coulombic interaction.

Bound excitonic states can be identified as sharp peaks in absorption and emission spectra, although the binding energy is small and they are rapidly ionised with increasing temperature by collisions with thermal photons. Excitons in quantum wells persist even at room temperature, due to the increased lateral confinement of the carriers. The energy of such an exciton is equal to the energy required to create the electron-hole pair (E_g) minus the binding energy due to the coulomb interaction. Therefore exciton absorption occurs at energies below the fundamental bandgap.

Recombination

Electrons in a conduction band can relax to a valence band giving up their energy as they return to equilibrium. This process can occur radiatively or non-radiatively and these mechanisms can have a major impact on the absorption recovery of modulator devices. Firstly radiative recombination occurs when the relaxation of such an electron does so by emitting most or all of its energy as an electromagnetic wave. Again the transition between the two states must have a finite probability of occurring and it also depends on the carrier density as BN^2 where B is the bimolecular recombination coefficient. In contrast, non-radiative recombination can occur via two routes.

- Impurities within a semiconductor can lead to a deviation in the periodicity of the crystal potential. This creates additional allowed electronic levels within the bandgap

[6]. In a process known as *Shockley – Read – Hall* recombination an electron and hole are trapped by such a level and recombine. This is proportional to the density of traps as AN , where A is a constant dependent of the material.

- Auger recombination [8] is a process that can occur in direct band and indirect band-gap materials. It can occur by more than one interaction, however the most common occurrence is in electron-electron scattering in the conduction band. An electron recombines with a hole in the valence subband, however the energy liberated is given to another conduction band electron which can be promoted higher in the conduction band. This carrier may recombine with a hole at a later time generating a photon. Auger is therefore determined by 3 carriers and hence its rate is CN^3 . It is purely a density dependent recombination process. In the experiments that follow the photogenerated carrier densities were too small for this effect to be relevant.

As the above processes generally compete in parallel with radiative processes their existence can seriously impair the efficiency of active optoelectronic devices.

2.2.3 Optical nonlinearities

The amplitude and phase change experienced by an optical wave propagating through a semiconductor depends greatly on the interplay between the optical transitions and relaxation mechanisms mentioned previously. As mentioned in chapter 1, the gain and nonlinear refraction are connected via the Kramers-Kronig relations. What follows is a general discussion of the nonlinearities that arise from intense optical excitation.

Band-filling dynamics

When an optical beam is incident on the semiconductor with energy greater than the band-gap, generated carriers are arranged according to Pauli's exclusion principle. The absorption can then be saturated if the radiation is intense enough. The relaxation processes that enable the absorption to recover (mentioned previously) typically take from a hundred picoseconds to 1ns. Therefore the response of the semiconductor to pulses of durations longer than a few picoseconds is governed by these interband transitions. Next we shall look at the dynamic processes that occur below 1ps.

Spectral hole burning (SHB)

For a finite frequency range of photons in an interacting optical pulse, there will be sufficient intensity to burn a hole in the quasi-Fermi distribution. This local bleaching of transitions recovers typically over a time of ≈ 100 fs, via carrier-carrier scattering. In the case of absorption the beam creates carriers over a finite frequency range, saturating these states. Conversely in the gain regime, stimulated emission will deplete carriers over this finite range temporarily. At transparency there are no net transitions and SHB does not occur.

Carrier heating

The quasi-Fermi distributions that determine the valence and conduction subbands are temperature dependent due to their Fermi-Dirac functions. This leads to a strong temperature dependence of the carrier density away from the lattice temperature. Increasing the carrier temperature reduces the gain over all frequencies and moves the peak to lower energies. Subsequent cooling of the distribution back to the lattice temperature is mediated by phonon emission. In the case of semiconductor gain materials, carrier heating has been found to play an important role in the ultrafast dynamics, with typical recoveries of 500fs-1.5ps [9]. Several mechanisms can be responsible for such an effect. Firstly, free carrier absorption (FCA) whereby the absorption of a photon leads to a carrier already in the conduction band being promoted to a higher state within the band. Therefore scattering processes are responsible for heating the distribution. Secondly an intense optical beam can remove (stimulated emission) carriers with energy lower than the lattice temperature (cold carriers). In addition, with suitable intense beams two-photon absorption (TPA) can heat the distribution via the generation of carriers high in the band [10].

2.3 GaInNAs multiple quantum wells

The quaternary alloy $Ga_{1-y}In_yN_xAs_{1-x}$ is a unique III-V compound semiconductor, that can be grown lattice matched to GaAs (see figure 2.9). The transition energy of this alloy with $x=0$ can be tuned from 1.42eV to below 1.1eV, however the strain prevents these high quality QWs achieving a bandgap below 1eV. The inclusion of N in dilute amounts

($x \approx 0.01$) reduces the strain and the telecommunications wavelengths of $1.3 \mu\text{m}$ (0.95eV) and $1.55 \mu\text{m}$ (0.80eV) can be achieved. This material system was first proposed in 1995 employing a type I heterostructure, giving high electron confinement which offered the potential for long wavelength lasers with good temperature characteristics [11]. However, the inclusion of N was first shown to give a red-shift in the bandgap of $\text{GaAs}_{1-x}\text{N}_x$ [12], demonstrating the large bowing of the bandgap energy. GaInNAs has sparked a great amount of research interest since this time. With such high electron confinement it offers temperature benefits over competing InP based lasers [13]. As it can be lattice matched to GaAs it can be used in surface emitting lasers which require high contrast GaAs bragg mirrors. It also offers the potential for modulator devices owing to the large quantum confined Stark effect [14]. In addition non-radiative recombination is particularly relevant in this material [15], which offers the potential for fast absorption recovery for the use in modelocking of solid state lasers [16].

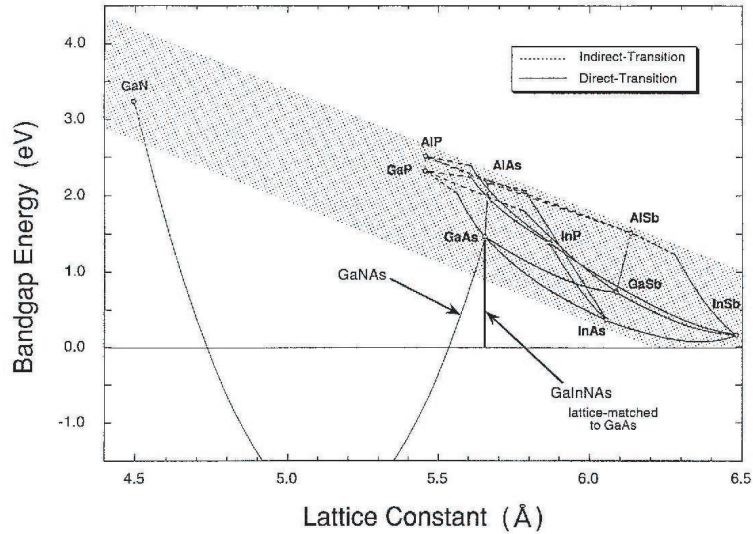


Figure 2.9: Relationship between the III-V and III-N-V compound semiconductors, showing the lattice matching of GaInNAs to GaAs. The inclusion of N is shown to cause a decrease in the bandgap with a decrease in lattice constant, in contrast to conventional semiconductors which show an increase in bandgap for a decrease in lattice constant (from Kondow et al. [11]).

2.3.1 Electronic Structure

Introducing nitrogen into InGaAs leads to the formation of localised and optically active electron states near the conduction band of the host material [17]. Energy states are

also created deep in the valence band [18] but these are not always in the region of interest to us and hence do not contribute to the band gap properties. The large difference between the atomic size of N and As leads to lattice relaxation around the substituted N atoms due to increased bond length and leads to deformation of the potential. The larger electronegativity of N compared to Ga and As favours the electron localization around the N atom. These dilute quantities have significant effects on the bandstructure due to the large molar fraction of the nitrogen upon substitution. Attempts to explain the large bandgap bowing and also a large effective mass ($\approx 0.11m_0$) have led to two models. Firstly the pseudopotential theory. This is a microscopic theoretical model used to calculate wavefunctions and band energies using experimentally corrected pseudopotentials. The calculation method is similar to that used for many semiconductors (see for example Chelikowsky et al. [19]). The second is an empirical band anticrossing model as explained below.

Band Anticrossing model (BAC)

The band anticrossing model was introduced to describe the two level repulsion observed in GaInNAs alloys [20]. The conduction band splitting is explained by the N induced perturbation which is enhanced as the N concentration is increased, giving an increasing energy separation between them. The new conduction bands are denoted E_+ and E_- and can be expressed as,

$$E_{\pm}(k) = \frac{1}{2} \left(E_N + E_M(k) \pm \sqrt{[E_N - E_M(k)]^2 + 4C_{NM}^2 \cdot x} \right). \quad (2.37)$$

Where, E_N is the N-induced energy state spread over the reciprocal space with constant energy and E_M is the energy dispersion of the GaAs conduction band. The advantage of the BAC model is that it provides a simple analytical expression for the conduction band dispersion as shown in figure 2.10. The BAC model has been used successfully to predict the increase in electron effective mass [21] and whilst over simplified, it has also been shown to describe the material properties of GaInNAs very well [22, 23].

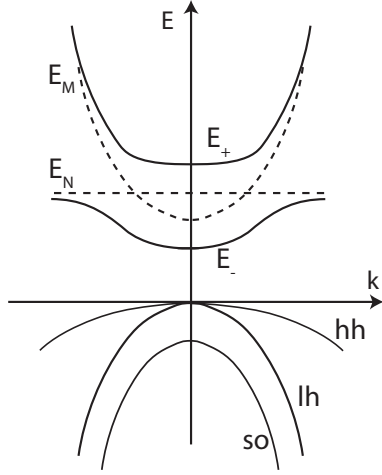


Figure 2.10: Schematic of the band anticrossing model of GaInNAs. The energy state E_N and the energy dispersion of the GaAs conduction band E_M are drawn with dashed lines. As a result of the anticrossing interaction, the energy bands E_+ and E_- are formed.

However, in the case of GaNAs alloys with $N > 0.1\%$ the BAC model underestimates the conduction band mass quite considerably. It has therefore been proposed that the nitrogen defect level above the conduction band may in fact be a range of defect levels, arising from clusters of nitrogen states in the material. A description of this compliment to the BAC model can be found by Lindsey et al. [24].

2.3.2 Recombination centres

The electronegativity of N is greater than both Ga or As and favours electron localisation around the nitrogen atom. This gives rise to crystalline defects which act as nonradiative recombination centres [25]. In the work of Chen et al. it was found that a lower growth temperature lead to an increase in the number of defects. Low growth temperatures are typically employed to suppress phase separation of the quaternary into GaN and InAs. However by applying rapid thermal annealing (RTA) these defects were shown to greatly reduced.

Thermal annealing

Thermal annealing has been shown to improve the optical properties of GaInNAs QWs with regards to the photoluminescence by reducing the concentration of defects [26]. This also leads to a smoother topology of the interface and is a technique also used to grow

bilayer quantum dots. However, annealing has been shown to give a blue-shift in the bandgap energy (a more complete discussion of this can be found in [27]).

The likely explanation for this is based upon the short range ordering of preferential bonding, during and after the annealing process. Klar et al. [28] found that in samples containing 30% indium, that the nitrogen occurred at (In) rich sites after annealing. They proposed that due to the non-equilibrium nature of the growth process, that Ga-N bonds are favoured at the surface of the growth. After appropriate annealing however, there is a shift to the equilibrium state where the N substitutes for a As atom and where In-N bonds are more likely as this relaxes the overall strain. The increase in nearest neighbours has the effect of reducing the perturbation of the potential and the bandgap increases slightly (dependent on N concentration) leading to a blue shift in the transition.

2.4 Quantum dot heterostructures

Quantum dots are not only interesting from the fundamental idea of producing artificial atoms (confinement on the order of the de Broglie wavelength in all 3 dimensions). They also exhibit high differential gain and fast carrier capture into their discrete states which is exciting from a device point of view, and even more so when the properties of these states can be tailored by changing the growth parameters.

2.4.1 Energy levels in QD systems

From a fundamental point of view and more specifically for the application to devices, it is desirable to be able to model the electronic structure of QDs. The simplistic approach for the case of quantum wells using the envelope function theory has been shown previously, the details of which can also be found in such texts as Bastard [29]. The basis of this calculation involves solving the eigenstates of a given quantum mechanical potential. However, in the case of quantum dots there are many uncertainties in the composition and shapes that arise from the generation of isolated 3D island on an otherwise 2D material system.

This problem arises because it is difficult to ascertain accurate structural information about the dots. There are no direct measurement techniques to determine the shape,

composition and strain once the dots are embedded in the final epitaxial structure. Despite this many complex models have been used to describe the dots. However it is difficult to choose a definitive method, again due to the lack of structural information. One of the first assumptions which needs to be made is the shape of the dot. Many techniques have been used to model the electronic properties of different shaped dots, most notably lens shaped [30], spherical [31] and pyramidal [32, 33]. A comprehensive review of the different methods can be found in Bimberg et al. [34].

In summary, the modeling consists of two main processes. Firstly when the structural assumptions have been established (such as shape and InAs/GaAs composition), the strain in the dot is calculated, using elastic theory. This results in the generation of a confinement potential where further assumptions regarding effective masses, band offsets and piezoelectric effects all need to be taken into account. The calculation of this potential is the most difficult part to predict accurately. The second process requires solving the Schrodinger equation for electrons and holes that exist in such a potential. This is commonly done using a single band, or eight band $\mathbf{k} \cdot \mathbf{p}$ numerical calculations [35] (the eight bands are the conduction, heavy hole, light hole and split-off, including spin up and down).

Additional steps can include coulombic effects or exciton binding energies, however these add to the complexity of the problem. The use of such calculations is clearly important however with so much uncertainty in the initial parameters it is very difficult to arrive at an accurate quantitative picture in regards to the electronic properties.

From the discussion above, sophisticated modeling of QDs is beyond the scope of this thesis. A simple picture of free dots is sufficient to analyse our results. Furthermore from an experimental point of view, appropriate information can be gained by the use of linear spectroscopy and photocurrent measurements, which will form a large part of the work presented in this thesis.

2.4.2 Bilayer InAs/GaAs quantum dots

Increasing the fill factor of the active region is particularly useful for quantum dot devices in order to increase the gain. However, if QD layers are grown close together the strain from the underlying layer leads to preferential nucleation above the buried QDs [36]. This

occurs because the In atoms can achieve a lower thermodynamic state due to the lower lattice mismatch between the InAs and the GaAs barrier layer. Since QD nucleation is more likely above the buried QDs, the formation occurs earlier in the second layer and so these dots become larger. However if the same growth conditions are used then the emission from the second layer of dots is actually blue shifted. This is due to strain-induced intermixing between the In and Ga [37, 38, 39]. This was investigated by predominantly altering the spacer layer thickness between adjacent layers of QDs and studying their emission via photoluminescence.

With this in mind, the close stacking of QD layers can be used to exploit the strain driven nucleation of In in the second layer as shown in figure 2.11. The addition of more InAs in the second layer growth phase was found to further increase the size of QDs in this layer and hence extend the wavelength emission [40, 41]. In addition the first layer was found to act as a template for the second layer, giving a more uniform size distribution of QDs offering a narrower inhomogeneous line-width for the emission.



Figure 2.11: Schematic showing the formation of bilayer quantum dots. The first layer (seed) acts as a template for the formation of In rich nucleation and the growth of larger dots in the second layer.

Long wavelength emission has also been demonstrated by reducing the growth temperature in the second layer, in order to inhibit the strain-induced intermixing [42]. It was later also shown that to get coincident emission from QD layers a smooth interface between the layers is required. In addition by annealing the surface prior to the growth of a second QD layer, the blue-shift can also be suppressed [43]. The emission wavelength from such material is clearly dependent on the QD size, whilst electronic coupling from the seed layer into the larger dots in the second layer is paramount to realising practical devices. A comprehensive study of the critical thickness of spacing between adjacent layers was carried out by Howe et al. [44]. In more recent work, the effects of In segregation and diffusion through the GaAs capping have been investigated, in order to optimise the critical thickness of InAs needed for dot formation in the second layer [45].

2.5 Electric field effects: The p-n junction

So far we have introduced the semiconductor materials. In order to observe electric field effects, we need to incorporate the material of interest between electrical contacts. One way to do this is to create a p-i-n structure, with the active material included in the intrinsic (i) region. The electrical bias can then be applied between the two (p and n) doped regions.

The semiconductor devices in this thesis rely on the conductivity of the material being defined by the impurity concentrations throughout the structure, known as doping. For the case of III-V devices the impurity usually comes from group IV of the periodic table. If such an impurity replaces a lattice site of a group III element it is known as a donor atom and the material becomes known as *n-type*, having an excess of electrons. Conversely if it replaces a group V element then it is known as an acceptor and becomes *p-type* with an excess of holes.

Now, to establish an equilibrium, electrons diffuse from the *n-type* whilst holes diffuse from the *p-type*. These recombination currents form a charge neutral region in the centre of the junction known as the depletion region. When it is desirable to increase this region an intrinsic region can be artificially generated by not doping this part of the structure and we then have a p-i-n junction. The *n-type* now has a net positive charge and *p-side* a net negative. Because of this net electric field, thermally activated carriers lead to generation currents in the opposite direction to the recombination currents and at thermal equilibrium the currents balance one another.

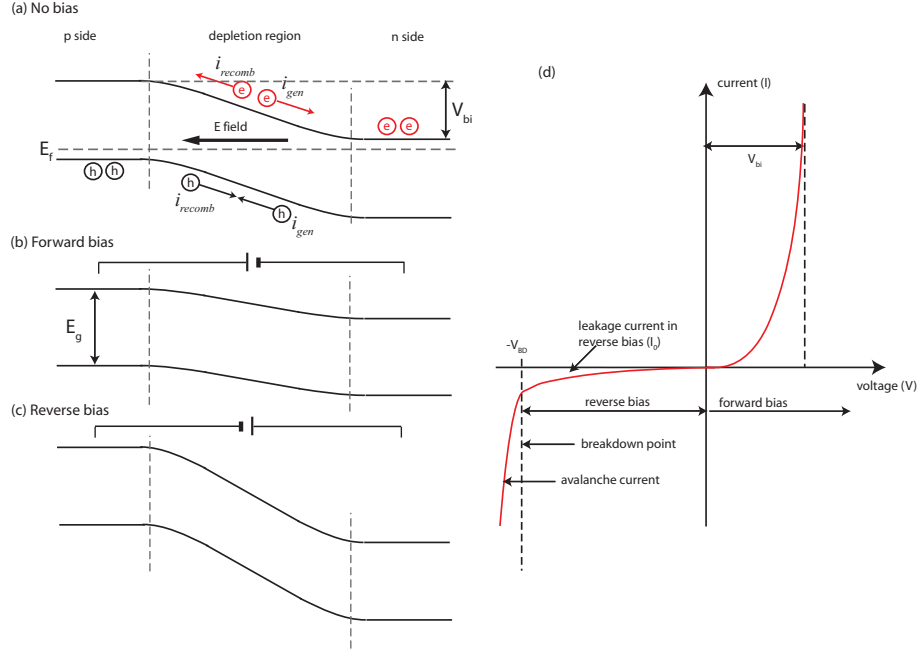


Figure 2.12: (a) pn junction, showing the recombination currents due to doping and generation currents from thermal effects at equilibrium. (b) Under forward bias. (c) Under reverse bias conditions. (d) I-V curve for a pn junction diode

If we now apply an external voltage and add electrons and holes, the generation currents stay the same but the recombination current increases by an amount equivalent to the Maxwell-Boltzman factor $\exp(\Delta E/k_b T) = \exp(eV/k_b T)$. This gives the net current as follows.

$$\begin{aligned}
 i_{total} &= i_{recomb} - i_{gen} \\
 &= i_{gen} e^{(eV/k_b T)} - i_{gen} \\
 I &= I_0 (e^{eV/k_b T} - 1)
 \end{aligned} \tag{2.38}$$

where I_0 is the saturation current under reverse bias. Two effects can occur under high reverse bias. Firstly avalanche breakdown, where carriers gain enough kinetic energy to create electron hole pairs by inelastic scattering. Secondly, Zener breakdown, whereby the valence band sits above the bottom of the conduction band and electrons and holes can tunnel through the junction.

Under the application of a reverse electric field electrons and holes will be driven in

opposite directions. The carriers can escape from the quantum wells or dots via two predominant mechanisms, which are field dependent. They are thermionic emission and quantum mechanical tunneling and will be introduced in the following section.

2.5.1 Thermionic emission theory

In order for an electron to escape during some time Δt , it must have v_x sufficient to overcome the image-charge barrier and must be sufficiently close to the metal-semiconductor interface $v_x \Delta t$. Two further assumptions are required. Firstly, the potential barrier is much larger than $k_b T$ and secondly, the electron collisions within the depletion region are neglected. Note that in figure 2.13(a) many electrons within the volume will not hit the area (A) due to their perpendicular components of velocity. However there will be neighbouring electrons that will hit A. So to find the total number we integrate over all possible v_x .

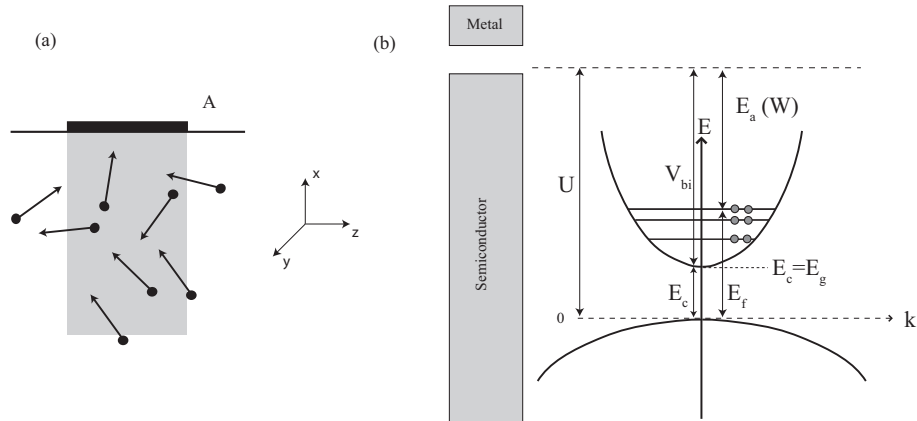


Figure 2.13: (a) Pictorial description of electron emission from the surface of a metal/semiconductor. (b) Energy diagram for electron emission from a semiconductor-metal interface.

The current density from a semiconductor to a metal can be defined as follows [46]

$$J_{s \rightarrow m} = qn \left(\frac{m}{2\pi k_b T} \right)^{\frac{3}{2}} \int_{-\infty}^{\infty} dv_y \int_{-\infty}^{\infty} dv_z \int_{v_{0,x}}^{\infty} v_x \exp \left(- \frac{m(v_x^2 + v_y^2 + v_z^2)}{2k_b T} \right) dv_x \quad (2.39)$$

where q is the electron charge, n is the total carrier density and the factor outside the integral is related to the constant density of states in velocity space. We need to integrate

in velocity space over the kinetic energy, however we are only interested in carriers that have sufficient velocity to escape in the x direction.

We can use the Gaussian integral in order to solve this equation giving the following,

$$J_{s \rightarrow m} = qn \left(\frac{k_b T}{2\pi m} \right)^{\frac{1}{2}} \exp \left(-\frac{mv_{0,x}^2}{2k_b T} \right) \quad (2.40)$$

We can now apply the conservation of energy to relate the carrier distribution in terms of the underlying potential $\frac{1}{2}m^*v_{0,x}^2 - qV_{bi} = 0$. Additionally we need to calculate the density of carriers. For this we use the previously defined analytical approximation of n_{3d} in equation 2.9. Because we are interested in carriers escaping from the top of the potential where $E \gg k_b T$ we can use the Boltzman distribution [47].

$$J_{s \rightarrow m} = q2 \left(\frac{2\pi m^* k_B T}{\hbar^2} \right)^{\frac{3}{2}} \left(\frac{k_b T}{2\pi m^*} \right)^{\frac{1}{2}} \exp \left(-\frac{qV_{bi}}{k_b T} \right) \exp \left(-\frac{(E_c - E_f)}{k_b T} \right) \quad (2.41)$$

From inspection of figure 2.13 we see that $qV_{bi} = qU - E_c$ and can re-write equation 2.41 as follows,

$$J_{s \rightarrow m} = \frac{q4\pi m^* (k_b T)^2}{\hbar^3} \exp \left(-\frac{(qU - E_f)}{k_b T} \right) = A^* T^2 \exp \left(-\frac{W}{k_b T} \right). \quad (2.42)$$

This is known as Richardson's Law for a metal/vacuum interface [48] where $A^*/A = m^*/m_0$ is defined for the effective electron mass m^* , where m_0 is the free electron mass. Similarly the hole current can be found by summing the light and heavy hole masses to give $(A^*/A)_h = (m_{lh}^* + m_{hh}^*)/m_0$. Note that in equation 2.42, $-(qU - E_f)$ is known as the work function (W) however in quantum well analysis it is often referred to as the activation energy E_a .

The rate of thermionic emission can then be given as follows

$$\Gamma_{therm} = \frac{A}{q} T^2 \exp \left(-\frac{E_a}{k_b T} \right) \quad (2.43)$$

In the case of quantum confined structures that will be used in this thesis, we will use an equation of the form shown in 2.43 to investigate the thermionic emission effects. As can be seen from figure 2.14, the barrier height will be reduced and the applied field will

have an influence on the emission of carriers

2.5.2 Field emission - Fowler-Nordheim tunneling

Field emission is the process whereby electrons or holes tunnel through a barrier in the presence of a high electric field. This is extremely important in the case of thin barriers in semiconductor-metal junctions when the doping densities are high. This is also highly important for quantum well and dot heterostructures under the influence of high fields.

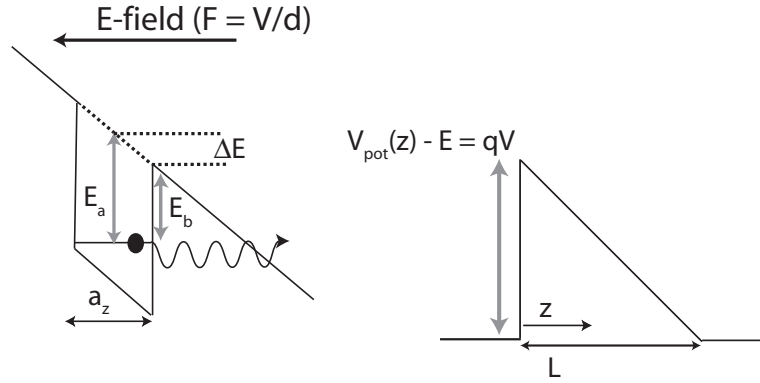


Figure 2.14: Fowler-Nordheim tunneling as a WKB approximation to a tunneling from a quantum confined potential

We recall that for an electron (or hole) confined to a potential in 1D, the time independent Schrodinger equation can be written as follows,

$$\frac{d^2\Psi}{dz^2} = \frac{2m^*(V_{pot} - E)}{\hbar^2}\Psi. \quad (2.44)$$

Assuming that $(V_{pot} - E)$ is non-varying over a small increment $z+dz$ we can write,

$$\Psi(z + dz) = \Psi(z)\exp(-k dz) \quad \text{where} \quad k = \frac{\sqrt{2m^*(V_{pot} - E)}}{\hbar}. \quad (2.45)$$

For a slowly varying potential we can apply the Wentzel-Kramers-Brillouin (WKB) approximation [49] and therefore integrate over the function that describes the potential from $z \rightarrow L$,

$$\Psi(L) = \Psi(0)\exp\left(-\int_0^L \frac{\sqrt{2m^*(V_{pot} - E)}}{\hbar} dz\right). \quad (2.46)$$

The tunneling probability is then the probability ratio of finding the particle beyond the barrier to that of finding it inside the well.

$$\Theta = \frac{\Psi(L)\Psi^*(L)}{\Psi(0)\Psi^*(0)} = \exp\left(-\frac{4\sqrt{2m^*}E_b^{3/2}}{3\hbar qF}\right), \quad (2.47)$$

where,

$$E_b = V_{pot} - E = qV(z=0) \quad F = V/L. \quad (2.48)$$

We now make the approximation that the z component of the electron k vector is equal to that for an infinite square potential well [50], namely $k_z = n\pi/a_z$, so therefore the electron velocity is $v_z = n\pi\hbar/a_z m^*$. The frequency at which the electron then strikes one barrier is,

$$f = \frac{n\hbar\pi}{2a_z^2 m^*}. \quad (2.49)$$

The overall tunneling rate is then the product of the barrier collision frequency and the tunneling probability,

$$\Gamma_{tun} = \frac{\hbar\pi}{2m_d^* a_z^2} \exp\left(-\frac{4\sqrt{2m_b^*}E_b^{3/2}}{3q\hbar F}\right). \quad (2.50)$$

From equation 2.50 it is clear that the tunneling rate is dependent on the barrier height and the field directly. One further aspect to mention is the change in absorption due to the presence of an electric field on a semiconductor material, and this will form the basis of the next section.

2.5.3 Electro-absorption mechanisms in bulk

Electro-absorption is the change in a materials absorption properties under the influence of an electric field. Practically this allows for fast electrically driven optical modulators by reverse biasing a semiconductor diode of suitable band gap material. In direct band gap bulk semiconductors this is known as the Franz-Keldysh effect [51, 52], however the effect requires high electrical fields and is only practical in waveguide devices with a long interaction length.

We know that the transition rate of an electron from an initial state in the valence band to a final state in the conduction band is determined by the overlap of wavefunctions. When an electric field is applied, the eigenfunctions are shifted laterally by the electrostatic potential ($z_{shift} = (E_{c1} - E_{c2}/qF)$) and the bloch waves no longer describe the stationary states of the crystal. The tail of both wavefunctions can now penetrate the previously forbidden band gap region, which allows partial overlap of the electron and hole wavefunctions. This in turn allows absorption of photons with energy below the band gap as shown in figure 2.15(a). This has the effect of red-shifting the absorption bandedge. Above the band gap oscillations are superimposed on the absorption due to the increasing lateral shift of the wavefunctions when performing the overlap integrals for increasing energies.

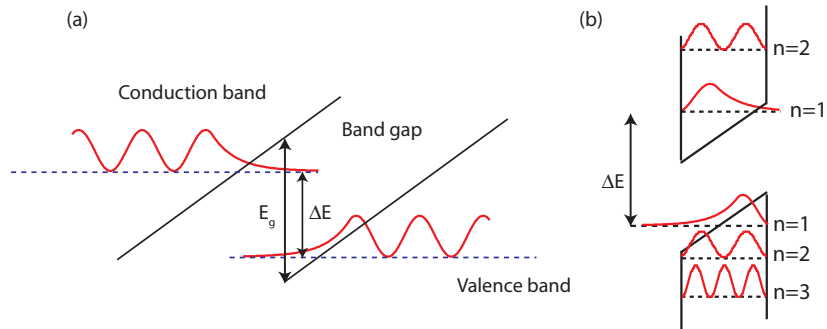


Figure 2.15: (a) Franz-Keldysh effect for bulk direct band gap semiconductors for absorption between eigenstates. (b) The quantum confined Stark effect, showing the spatial separation of the electron and hole wavefunctions.

Franz-Keldysh excitonic effects

In bulk material the presence of excitons drastically alters the absorption feature under application of an electric field. The bound electron and hole exist in a coulombic potential which is tilted by the field. Typical values for modulator devices are 1-10V across an intrinsic region of $1\mu\text{m}$ (10meV across 10nm), which is very large when compared to a typical bulk GaAs exciton diameter with a binding energy of $\approx 4\text{meV}$. Such a large field gives a high probability that the electron and hole can tunnel out of the confining potential very quickly (relative to the exciton orbit time). Such rapid field ionization gives rise to a large lifetime broadening of the exciton. This broadening can be seen to dominate the absorption below the band gap, whilst the exciton feature is washed out [53]. Although

the Franz-Keldysh effect is used successfully in electro-optic waveguide modulators, the effect is not strong enough to be used for high contrast modulators for light perpendicular to the electrical contacts (vertical devices). As such, excitons in bulk material are very weak and the Franz-Keldysh effect is therefore described almost entirely by the slanting of the bands as shown in figure 2.15(a).

2.5.4 The quantum confined Stark effect (QCSE)

The introduction of quantum wells lead to the discovery of a similar shift in the absorption edge under the influence of electric fields perpendicular to the wells. The theory showed this was due to overlap of airy functions describing the now quantum confined states in the conduction and valence bands and the effect was named the quantum confined Stark effect [54](due to similarity to Stark shifts in atomic like levels). The effect is more pronounced in quantum wells due to the large overlap of the highly confined wavefunctions as shown in figure 2.15(b).

The mathematical treatment is relatively straight forward and involves adding a 'small' dipole perturbation to the Hamiltonian ($V' = \lambda U = -qzF$) in the Schrodinger equation. We know the solution to the unperturbed schrodinger equation is a complete set of eigenfunctions (ψ_n) with eigenvalues (E_n) that correspond to the electron and hole states (see equation 2.14). The new Hamiltonian ($H'_0 = H_0 + \lambda U$) gives rise to the modified Schrodinger equation, $(H_0 + V')\psi'_n = \psi'_n E'_n$.

The assumption is that the solutions to the new Hamiltonian can be written as the old wavefunctions plus small corrections, smaller to larger orders. The subscript denotes the state in the following,

$$\psi'_n(\lambda) = \psi_n + \lambda\psi_n^{(1)} + \lambda^2\psi_n^{(2)} + \dots \quad (2.51)$$

$$E'_n(\lambda) = E_n + \lambda E_n^{(1)} + \lambda^2 E_n^{(2)} + \dots \quad (2.52)$$

Once substituted into the Schrodinger equation the terms can be grouped in increasing order as follows,

$$H_0|\psi_n\rangle = E_n|\psi_n\rangle \quad (2.53)$$

$$(H_0 - E_n)|\psi_n^{(1)}\rangle + (V' - E_n^{(1)})|\psi_n\rangle = 0 \quad (2.54)$$

$$(H_0 - E_n)|\psi_n^{(2)}\rangle + (V' - E_n^{(1)})|\psi_n^{(1)}\rangle - E^{(2)}|\psi_n\rangle = 0. \quad (2.55)$$

Clearly the zeroth order is just the equation for the unperturbed case and shows that $\langle\psi_n|$ is an eigenstate of H_0 .

If we now project the first order equation onto the $|\psi_n\rangle$ state we find that the first order correction to the energy is zero due to integration over an asymmetric function $E_n^{(1)} = \langle\psi_n|V'|\psi_n\rangle = 0$. However if we project onto another state $|\psi_p\rangle$ we find there exists a first order correction, as shown in equation 2.56.

$$|\psi_n^{(1)}\rangle = \sum_{n \neq p} \frac{\langle\psi_p|V'|\psi_n\rangle}{E_n - E_p} |\psi_p\rangle \quad (2.56)$$

This correction has contributions (weighted by their energy separation), from all other states of the unperturbed system (except n). Now projecting the 2nd order equation onto $\langle\psi_n|$ and using equation 2.56 we find that the second order correction to the energy is,

$$E_n^{(2)} = \sum_{p \neq n} \frac{\langle\psi_p|V'|\psi_n\rangle\langle\psi_n|V'|\psi_p\rangle}{E_n - E_p} = \sum_{p \neq n} \frac{|\langle\psi_p|V'|\psi_n\rangle|^2}{E_n - E_p} \quad (2.57)$$

This second order energy correction is the change in energy for a state under the influence of the perturbing potential ($V'=qzF$). For very deep wells we can use the eigenfunctions and eigenvalues for the lowest laying levels of the infinite well case (equations 2.16 and 2.17) for the overlap integral in equation 2.57. The result gives the shift in the conduction band state for the electron, however exactly the same thing happens for the holes in valence band. Combining the two gives the shift in energy of the band gap as follows, where $M=m_e+m_h$.

$$E_g(F) = E_g(0) - \frac{2^9}{3^5\pi^6} \frac{q^2 a^4 M F^2}{\hbar^2} \quad (2.58)$$

Now as the electric field pulls the electron wavefunctions to one side of the well and

the hole wavefunctions in the opposite direction (see figure 2.15), the overlap integral is reduced. This has the effect of reducing the magnitude of the absorption close to the bandedge, an effect that is more pronounced in in QWs than in bulk due to the high confinement. This can be seen mathematically and schematically (figure 2.16) below.

$$\alpha(\omega) = \frac{\pi q^2 c \mu_0}{m_0^2 \omega n} |p_{cv}|^2 |\langle \psi_i | \psi_f \rangle|^2 \delta(\hbar\omega - E_{c1} - E_{v1}), \quad (2.59)$$

$|p_{cv}|^2$ accounts for the opposite parity allowed transitions, whilst the δ function is a requirement for the photon energy to equal the difference between initial and final states.

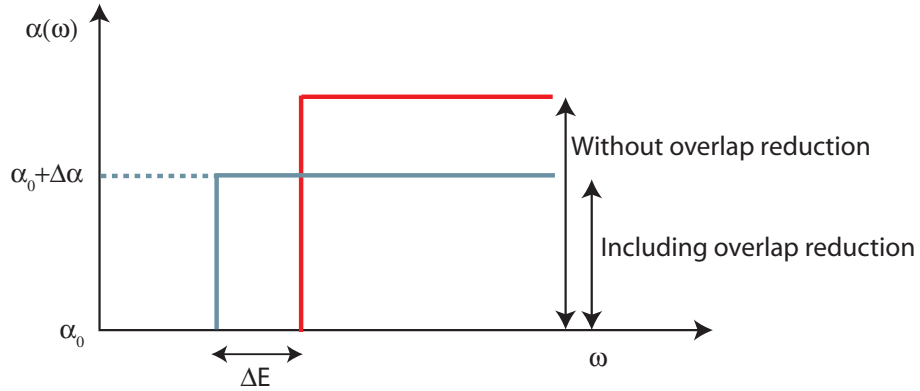


Figure 2.16: Reduction and shift of the absorption due to the quantum confined Stark effect.

QCSE excitonic effects

The above derivation neglects excitonic effects which are an integral part of the QCSE. Firstly, if the field is applied parallel to the QWs the exciton can readily be ionized by the field which gives rise to a broadening in the band edge [55] much like in the the bulk case. A more theoretical treatment of this can be found by Lederman and Dow [56].

In typical modulators however, the field is applied perpendicular to the wells and we see the true QCSE [55]. Whilst the electron and hole of the exciton are pulled to opposite sides of the well, this does not in general ionize the bound system due to the confinement, although the coulombic attraction of the pair is reduced. The contribution to the total reduction in the absorption edge energy is only an additional few meV. Under such orientation, as the well width is increased, the confinement becomes comparable or longer than the bulk exciton diameter and the exciton can become field ionized, whereby the QCSE becomes the Franz-keldysh effect in the classical limit [57].

2.6 Summary

We have introduced the III-V semiconductor materials which will be used in the devices under investigation in this thesis. By combining the active material inside the intrinsic region of a p-i-n heterostructure, electrical contacts can be evaporated onto the samples. This in turn allows electrical fields to be applied across the material. The major carrier escape mechanisms have been introduced from a fundamental description and their relevance to quantum confined structures detailed. In addition, the influence on absorption of reverse electrical fields has been discussed in the classical and quantum confined cases.

References for Chapter 2

- [1] P Y Yu and M Cardona. *Fundamentals of Semiconductors*. Springer, 2nd edition, 1999.
- [2] H D Young. University Physics, eighth edition. *Addison Wesley Publishing*, page p1232, 1992.
- [3] J Gowar. Optical communication systems 2nd edition. *Englewood cliffs, N.J.: Prentice Hall*, 1993.
- [4] S Schmitt-Rink, D S Chemla, and D A B Miller. Linear and nonlinear optical properties of semiconductor quantum wells. *Advances in physics*, 38(2):pp. 89–188, 1989.
- [5] P K Basu. Theory of optical processes in semiconductors bulk and microstructures. *Oxford science publications*, 1997.
- [6] E Rosencher and B Vinter. *Optoelectronics*. Cambridge University Press, Cambridge, 1st edition, 2002.
- [7] M Asada. Intraband relaxation time in quantum-well lasers. *IEEE J. Quantum Electron.*, 25(9):2019–2026, 1989.
- [8] S Hausser, G Fuchs, A Hangleiter, K Streubel, and W T Tsang. Auger recombination in bulk and quantum well InGaAs. *Appl. Phys. Lett.*, 56(10):913–915, 1990.
- [9] M P Kesler and E P Ippen. Subpicosecond gain dynamics in GaAlAs laser diodes. *App. Phys. Lett.*, 51(22):1765–1767, 1987.
- [10] J Mork, J Mark, and C P Seltzer. Carrier heating in InGaAsP laser amplifiers due to two-photon absorption. *Appl. Phys. Lett.*, 64(17):2206, 1994.
- [11] M Kondow, K Uomi, A Niwa, T Kitatani, S Watahiki, and Y Yazawa. GaInNAs: A novel material for long wavelength range laser diodes with excellent high-temperature performance.
- [12] M Weyers, M Sato, and H Ando. Red shift of photoluminescence and absorption in dilute GaInN alloy layers. *Jpn. J. Appl. Phys.*, 31, 1992.
- [13] Z. Pan, L. H. Li, Y. W. Lin, B. Q. Sun, D. S. Jiang, and W. K. Ge. Conduction band offset and electron effective mass in GaInNAs/GaAs quantum-well structures with low nitrogen concentration. *Applied Physics Letters*, 78(15):2217–2219, 2001.
- [14] Y.S. Jalili, P.N. Stavrinou, J.S. Roberts, and G. Parry. Electro-absorption and electro-refraction in InGaAsN quantum well structures. *Electronics Letters*, 38(7):343–344, 2002.
- [15] A. Markus, A. Fiore, J. D. Ganiere, U. Oesterle, J. X. Chen, B. Deveaud, M. Ilegems, and H. Riechert. Comparison of radiative properties of InAs quantum dots and GaInNAs quantum wells emitting around 1.3 μ m. *Applied Physics Letters*, 80(6):911–913, 2002.
- [16] A McWilliams, A A Lagatsky, C G Leburn, P Fischer, C T A Brown, G J Valentine, A J Kemp, S Calvez, D Burns, M D Dawson, M Pessa, and W Sibbett. Low-loss GaInNAs saturable Bragg reflector for mode-locking of a femtosecond Cr⁴⁺:fosterite-laser. *IEEE Photon. Tech. Lett.*, 17(11):2292–2294, 2002.
- [17] E P O'Reilly, A Lindsay, and S Fahy. Theory of the electronic structure of dilute nitride alloys: beyond the band-anti-crossing model. *J Phys. Condens. matter*, 16:S3257–S3276, 2004.
- [18] L. Bellaiche, S. H. Wei, and Alex Zunger. Localization and percolation in semiconductor alloys: GaAsN vs GaAsP. *Phys. Rev. B*, 54(24):17568–17576, Dec 1996.
- [19] James R. Chelikowsky and Marvin L. Cohen. Electronic structure of silicon. *Phys. Rev. B*, 10(12):5095–5107, Dec 1974.
- [20] W. Shan, W. Walukiewicz, J. W. Ager, E. E. Haller, J. F. Geisz, D. J. Friedman, J. M. Olson, and S. R. Kurtz. Band anticrossing in GaInNAs alloys. *Phys. Rev. Lett.*, 82(6):1221–1224, Feb 1999.

- [21] C. Skierbiszewski, P. Perlin, P. Wisniewski, W. Knap, T. Suski, W. Walukiewicz, W. Shan, K. M. Yu, J. W. Ager, E. E. Haller, J. F. Geisz, and J. M. Olson. Large, nitrogen-induced increase of the electron effective mass in $In_yGa_{1-y}N_xAs_{1-x}$. *Applied Physics Letters*, 76(17):2409–2411, 2000.
- [22] K. M. Yu, W. Walukiewicz, W. Shan, J. W. Ager, J. Wu, E. E. Haller, J. F. Geisz, D. J. Friedman, and J. M. Olson. Nitrogen-induced increase of the maximum electron concentration in group III-N-V alloys. *Phys. Rev. B*, 61(20):R13337–R13340, May 2000.
- [23] M. Hofmann, A. Wagner, C. Ellmers, C. Schlichenmeier, S. Schafer, F. Hohnsdorf, J. Koch, W. Stolz, S. W. Koch, W. W. Ruhle, J. Hader, J. V. Moloney, E. P. O’Reilly, B. Borchert, A. Yu. Egorov, and H. Riechert. Gain spectra of (GaIn)(NAs) laser diodes for the $1.3\mu\text{m}$ wavelength regime. *Applied Physics Letters*, 78(20):3009–3011, 2001.
- [24] A. Lindsay and E. P. O’Reilly. Unification of the band anticrossing and cluster-state models of dilute nitride semiconductor alloys. *Physical Review Letters*, 93(19):196402, 2004.
- [25] W M Chen, I A Buyanova, C W Tu, and H Yonezu. Point defects in dilute nitride iii-n-as and iii-n-p. *Physica B*, 376-377:545–551, 2006.
- [26] E. Tournie, M.-A. Pinault, and A. Guzman. Mechanisms affecting the photoluminescence spectra of GaInNAs after post-growth annealing. *Applied Physics Letters*, 80(22):4148–4150, 2002.
- [27] C Reith. Spin relaxation and carrier recombination in GaInNAs multiple quantum wells. *phD Thesis*, page Chapter 5: Carrier lifetime, 2006.
- [28] Klar, P. J. and Grüning, H. and Koch, J. and Schäfer, S. and Volz, K. and Stolz, W. and Heimbrodt, W. and Saadi, A. M. Kamal and Lindsay, A. and O’Reilly, E. P. (Ga, In)(N, As)-fine structure of the band gap due to nearest-neighbor configurations of the isovalent nitrogen. *Phys. Rev. B*, 64(12):121203, Sep 2001.
- [29] G Bastard. *Wave mechanics applied to semiconductor heterostructures*. John Wiley and sons, 1992.
- [30] Arkadiusz Wojs, Pawel Hawrylak, Simon Fafard, and Lucjan Jacak. Electronic structure and magneto-optics of self-assembled quantum dots. *Phys. Rev. B*, 54(8):5604–5608, Aug 1996.
- [31] A. J. Williamson and Alex Zunger. Inas quantum dots: Predicted electronic structure of free-standing versus gaas-embedded structures. *Phys. Rev. B*, 59(24):15819–15824, Jun 1999.
- [32] Lin-Wang Wang, Jeongnim Kim, and Alex Zunger. Electronic structures of [110]-faceted self-assembled pyramidal inas/gaas quantum dots. *Phys. Rev. B*, 59(8):5678–5687, Feb 1999.
- [33] M. A. Cusack, P. R. Briddon, and M. Jaros. Electronic structure of inas/gaas self-assembled quantum dots. *Phys. Rev. B*, 54(4):R2300–R2303, Jul 1996.
- [34] D Bimberg, M Grundmann, and N N Ledentsov. Quantum dot heterostructures. *John Wiley and sons*, 1999.
- [35] Hongtao Jiang and Jasprit Singh. Strain distribution and electronic spectra of inas/gaas self-assembled dots: An eight-band study. *Phys. Rev. B*, 56(8):4696–4701, Aug 1997.
- [36] Qianghua Xie, Anupam Madhukar, Ping Chen, and Nobuhiko P. Kobayashi. Vertically Self-Organized InAs Quantum Box Islands on GaAs(100). *Phys. Rev. Lett.*, 75(13):2542–2545, Sep 1995.
- [37] M. O. Lipinski, H. Schuler, O. G. Schmidt, K. Eberl, and N. Y. Jin-Phillipp. Strain-induced material intermixing of InAs quantum dots in GaAs. *Applied Physics Letters*, 77(12):1789–1791, 2000.
- [38] H. Heidemeyer, S. Kiravittaya, C. Muller, N. Y. Jin-Phillipp, and O. G. Schmidt. Closely stacked InAs/GaAs quantum dots grown at low growth rate. *Applied Physics Letters*, 80(9):1544–1546, 2002.

- [39] O. G. Schmidt and K. Eberl. Multiple layers of self-assembled ge/si islands: Photoluminescence, strain fields, material interdiffusion, and island formation. *Phys. Rev. B*, 61(20):13721–13729, May 2000.
- [40] I. Mukhametzhanov, R. Heitz, J. Zeng, P. Chen, and A. Madhukar. Independent manipulation of density and size of stress-driven self-assembled quantum dots. *Applied Physics Letters*, 73(13):1841–1843, 1998.
- [41] R. Heitz, I. Mukhametzhanov, P. Chen, and A. Madhukar. Excitation transfer in self-organized asymmetric quantum dot pairs. *Phys. Rev. B*, 58(16):R10151–R10154, Oct 1998.
- [42] E. C. Le Ru, P. Howe, T. S. Jones, and R. Murray. Strain-engineered InAs/GaAs quantum dots for long-wavelength emission. *Phys. Rev. B*, 67(16):165303, Apr 2003.
- [43] E. C. Le Ru, A. J. Bennett, C. Roberts, and R. Murray. Strain and electronic interactions in InAs/GaAs quantum dot multilayers for 1300nm emission. *Journal of Applied Physics*, 91(3):1365–1370, 2002.
- [44] P. Howe, E. C. Le Ru, E. Clarke, B. Abbey, R. Murray, and T. S. Jones. Competition between strain-induced and temperature-controlled nucleation of inas/gaas quantum dots. *Journal of Applied Physics*, 95(6):2998–3004, 2004.
- [45] P. Howe, E. C. Le Ru, E. Clarke, R. Murray, and T. S. Jones. Quantification of segregation and strain effects in InAs/GaAs quantum dot growth. *Journal of Applied Physics*, 98(11):113511, 2005.
- [46] H A Bethe. Theory of the boundary layer of crystal rectifiers. *MIT Radiation Laboratory*, Report 43-12, 1942.
- [47] H Schneider and K V Klitzing. Thermionic emission and Gaussian transport of holes in a $GaAs/Al_xGa_{1-x}As$ multiple-quantum-well structure. *Physical Rev. B*, 38(9):6160–6165, 1988.
- [48] S M Sze. Physics of Semiconductor Devices. *Wesley Interscience Publishing*, page pp379, 1969.
- [49] D Ferry. Quantum mechanics: An introduction for device physicists and electrical engineers. *Institute of Physics publishing*, second edition:89, 2001.
- [50] A Larsson, P A Andrekson, S T Eng, and A Yariv. Tunable Superlattice p-i-n Photodetectors: Characteristics, Theory and Applications. *IEEE J. Quant. Elect.*, 24(5):787–801, 1988.
- [51] W Franz and Z Naturforsch. . 13a:487, 1958.
- [52] L V Keldysh, Zh Eskp, and Teor. Fiz. . 34:1138, 1958 Sov. Phys. JETP 7, 788 (1958).
- [53] K. W. Goossen, J. E. Cunningham, and W. Y. Jan. Excitonic electroabsorption in extremely shallow quantum wells. *Applied Physics Letters*, 57(24):2582–2584, 1990.
- [54] D. A. B. Miller, D. S. Chemla, T. C. Damen, A. C. Gossard, W. Wiegmann, T. H. Wood, and C. A. Burrus. Band-edge electroabsorption in quantum well structures: The quantum-confined stark effect. *Phys. Rev. Lett.*, 53(22):2173–2176, Nov 1984.
- [55] D. A. B. Miller, D. S. Chemla, T. C. Damen, A. C. Gossard, W. Wiegmann, T. H. Wood, and C. A. Burrus. Electric field dependence of optical absorption near the band gap of quantum-well structures. *Phys. Rev. B*, 32(2):1043–1060, Jul 1985.
- [56] Frank L. Lederman and John D. Dow. Theory of electroabsorption by anisotropic and layered semiconductors. i. two-dimensional excitons in a uniform electric field. *Phys. Rev. B*, 13(4):1633–1642, Feb 1976.
- [57] D. A. B. Miller, D. S. Chemla, and S. Schmitt-Rink. Relation between electroabsorption in bulk semiconductors and in quantum wells: The quantum-confined franz-keldysh effect. *Phys. Rev. B*, 33(10):6976–6982, May 1986.

Chapter 3

Development of Femtosecond and Broadband Optical Sources

3.1 Introduction

Ultrashort optical pulses were required to study the ultrafast dynamics in waveguide devices in this thesis and to accomplish this an OPO was designed and constructed. A second continuous wave tunable broadband source was required to characterise the absorption of the devices. This was achieved by dispersing ultrashort pulses from a Ti:Sapphire laser through a section of highly nonlinear photonic crystal fibre. The aim of this chapter is to explain the physics involved in constructing and characterising the sources used for both pulsed and continuous wave measurements. The optical parametric oscillator provides a laser source with 250fs pulses tuneable from 1230nm-1600nm, suitable for investigating devices designed for the dispersion minimum of silica ($1.3\mu\text{m}$) and the low loss region of silica ($1.55\mu\text{m}$). These sources allow characterisation of both the absorption features and dynamics of the semiconductor samples.

3.2 Optical parametric Oscillator

The idea of Optical Parametric Oscillators (OPOs) was proposed more than 30 years ago [1]. However, only since the output powers and mode quality of pump lasers has vastly improved over the last decade has the development of these systems as efficient

spectroscopic tools become a practical reality [2]. Another advancement to be explained later, is the ability to periodically pole the domains of a nonlinear crystal avoiding the need to use birefringent materials for parametric generation [3, 4].

The OPO is similar to a normal laser in that it consists of a crystal providing gain surrounded by a pair of mirrors which form a resonating cavity. A high power pump wave (ω_p) is passed through a highly nonlinear crystal which down-converts the high frequency photon into two lower energy photons, asymmetrically conserving energy. The high and low frequency photons are called the signal (ω_s) and the idler (ω_i) respectively, with

$$\omega_p = \omega_s + \omega_i. \quad (3.1)$$

For both the signal and idler to experience gain in the cavity, all three waves must have a constant phase relationship so that their fields add up constructively. This strict condition of phase matching ($\Delta k = 0$) which conserves momentum, coupled with the energy conservation criterion are the fundamental operating principles of parametric generation.

$$\Delta \mathbf{k} = \mathbf{k}_p - \mathbf{k}_s - \mathbf{k}_i = \frac{\omega_p}{c} n_p - \frac{\omega_s}{c} n_s - \frac{\omega_i}{c} n_i = 0 \quad (3.2)$$

where, k and n are the wave vectors and refractive indices of the respective waves. In a typical crystal, waves propagate at different velocities due to dispersion. A $\Delta k \neq 0$ leads to a reduced conversion efficiency because the pump, signal and idler cannot propagate together over the length of the crystal. However birefringent materials have a refractive index that is dependent on the propagation direction and polarisation of the incident wave. It is possible to find such an angle (by rotating) relative to the crystal optical axis whereby all three waves will travel with a fixed phase relationship through the medium. The physical origin of this is the differing atomic bond strengths experienced by waves with orthogonal polarisations. In addition, changing the temperature or pressure also alters the effective refractive index in order to achieve phase-matching.

3.2.1 Coupled wave equations

When the electric field interacting with an optical material becomes comparable to the atomic field strength the relationship between the polarisation and electric field is no

longer linear (see equation 3.3). The important term for us is the second order nonlinear susceptibility $\chi^{(2)}$, which causes 3 wave mixing processes such as parametric generation as well as second harmonic generation (SHG), sum frequency generation (SFG) and difference frequency generation (DFG).

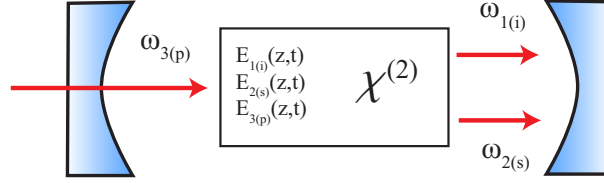


Figure 3.1: 3 wave interaction in a non-linear material exhibiting $\chi^{(2)}$.

$$\mathbf{P} = \epsilon_0[\chi^{(1)}\mathbf{E} + \chi^{(2)}\mathbf{E} \cdot \mathbf{E} + \dots] \quad (3.3)$$

We make the assumptions that the material is a non-absorbing dielectric medium and is non-conductive (no free charge). We can then substitute the polarisation term of interest from equation 3.3 into Maxwell's general non-linear wave equation for propagation in one dimension as follows,

$$\frac{\partial^2 \mathbf{E}}{\partial z^2} = \mu\epsilon \frac{\partial^2 \mathbf{E}}{\partial t^2} + \mu \frac{\partial^2}{\partial t^2} (\epsilon_0 \chi^{(2)} \mathbf{E} \cdot \mathbf{E}). \quad (3.4)$$

The electric field is a sum of the 3 mixing waves and if we manipulate the above, gathering terms relating to each frequency component, we arrive at the following set of coupled equations describing the parametric generation process. We make the assumption that the waves are plane waves and use the slowly-varying amplitude (adiabatic) approximation, in order to write mathematically,

$$\frac{d\mathbf{E}_1(z)}{dz} = i \frac{\omega_1}{n_1 c} d_{eff} \mathbf{E}_3 \mathbf{E}_2^* e^{i\Delta \mathbf{k}z} \quad (3.5)$$

$$\frac{d\mathbf{E}_2(z)}{dz} = i \frac{\omega_2}{n_2 c} d_{eff} \mathbf{E}_3 \mathbf{E}_1^* e^{i\Delta \mathbf{k}z} \quad (3.6)$$

$$\frac{d\mathbf{E}_3(z)}{dz} = i \frac{\omega_3}{n_3 c} d_{eff} \mathbf{E}_2 \mathbf{E}_1 e^{-i\Delta \mathbf{k}z}. \quad (3.7)$$

where $d_{eff} = \chi^{(2)}/2$ is the effective non-linear coefficient. The integration of these equa-

tions is quite complex as all three waves co-exist. However the point to note is that the conversion efficiency and consequently the gain coefficient is rapidly reduced once $\Delta\mathbf{k} \neq 0$.

3.2.2 Quasi-phasematching

Phase-matching using birefringence alone is restrictive as it depends on the relative orientation of polarisation and propagation direction. The interaction length is also limited by Poynting vector walk-off, where the wavevector (\mathbf{k}) and the vector describing the energy flow do not overlap after traveling a finite crystal length [5]. The point at which the maximum signal is generated is known as the coherence length (l_c), when the phase mismatch has reached π . Thereafter the signal begins to back convert and this cycle continues throughout the crystal. One way to correct this is to reverse the polarity of the non-linear coefficient periodically at l_c [6], a technique known as quasi-phasematching (QPM). This has the effect of bringing the waves back into phase and greatly improves the efficiency of the conversion, this is described in figure 3.2.

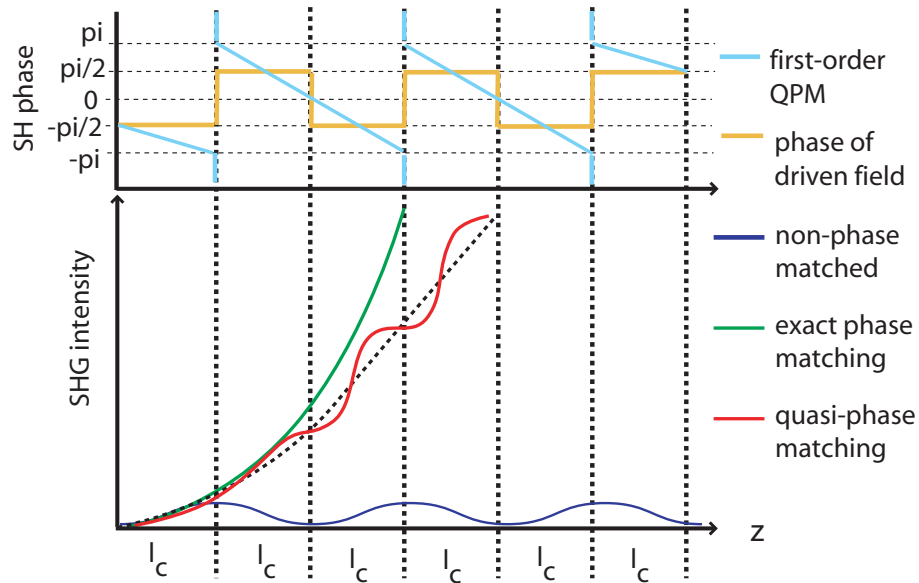


Figure 3.2: Graphical description of signal generation for non-phase matching, birefringent phase matching and quasi-phase matching. In addition the phase-mismatch vs crystal length has been included for clarity.

The phase matching condition now includes a degree of freedom in achieving zero phase mismatch. Λ is the period of modulation also known as the grating period and m is the order of the phasematching process,

$$\Delta \mathbf{k}_{QPM} = \mathbf{k}_p - \mathbf{k}_s - \mathbf{k}_i - \frac{2\pi m}{\Lambda}. \quad (3.8)$$

This flexibility allows the user to choose materials which have high nonlinear coefficients and large transparency regions, allowing the generation of broad wavelength ranges, circumventing some of the limitations found with birefringent crystals.

3.2.3 Optical properties of the gain medium (PPLN)

The OPO was constructed as part of this work and used a periodically poled lithium niobate ($LiNbO_3$) crystal (PPLN), which has a transparency range of 0.33-6 μ m. This allows the generation of wavelengths into the mid-infrared region of the spectrum, and is suitable for producing the wavelengths needed to investigate semiconductor samples in the near infrared (1.3-1.55 μ m).

From inspection of equation 3.8 it can be seen that in order to calculate the quasi-phasesmatching condition, it is necessary to know the precise refractive indices of crystal as a function of wavelength and temperature. The Sellmeier equation used to calculate the refractive indices for PPLN, has been derived from fitting experimental data up to 250 °C over the wavelength range 0.4-5 μ m [7],

$$n^2 = a_1 + b_1 F + \frac{a_2 + b_2 F}{\lambda^2 - (a_3 + b_3 F)^2} + \frac{a_4 + b_4 F}{\lambda^2 - a_5^2} - a_6 \lambda^2. \quad (3.9)$$

Where, $F=(T-T_0)(T+T_0+546.32)$. The reference temperature is $T_0=24.5$ °C and the values of the constants are: $a_1=5.35583$, $a_2=0.100473$, $a_3=0.20692$, $a_4=100$, $a_5=11.34927$, $a_6=1.5334 \times 10^{-2}$, $b_1=4.629 \times 10^{-7}$, $b_2=3.862 \times 10^{-8}$, $b_3=-0.89 \times 10^{-8}$, $b_4=2.657 \times 10^{-5}$.

By using this approximation combined with equation 3.8 for a specific grating period, the pump wavelength tuning curves can be obtained (see fig 3.3). Also for a fixed pump wavelength the temperature tuning curves can similarly be obtained by solving these equations.

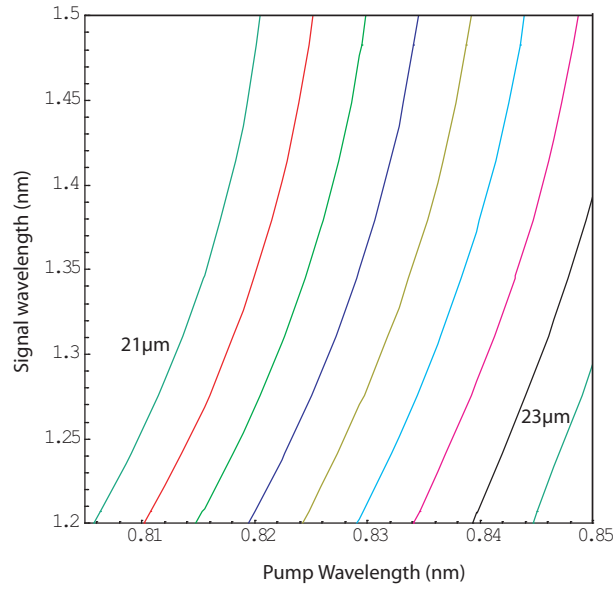


Figure 3.3: Pump wavelength tuning curves for the nine PPLN gratings $21.0\mu\text{m}$ to $23.0\mu\text{m}$ (in steps of $0.25\mu\text{m}$).

The PPLN crystal used in these experiments was 2mm long and contained nine gratings ranging from $21\mu\text{m}$ to $23\mu\text{m}$ in $0.25\mu\text{m}$ steps. It was anti-reflection coated ($R < 1\%$) on the front and rear facets for the pump wavelength range (760-860nm) as well as the signal wavelength range of interest (1.25-1.6 μm). The crystal was mounted in an oven to control the temperature. Fig 3.4 shows a crystal schematic and temperature tuning curves for a few of the gratings, given a pump wavelength of 820nm.

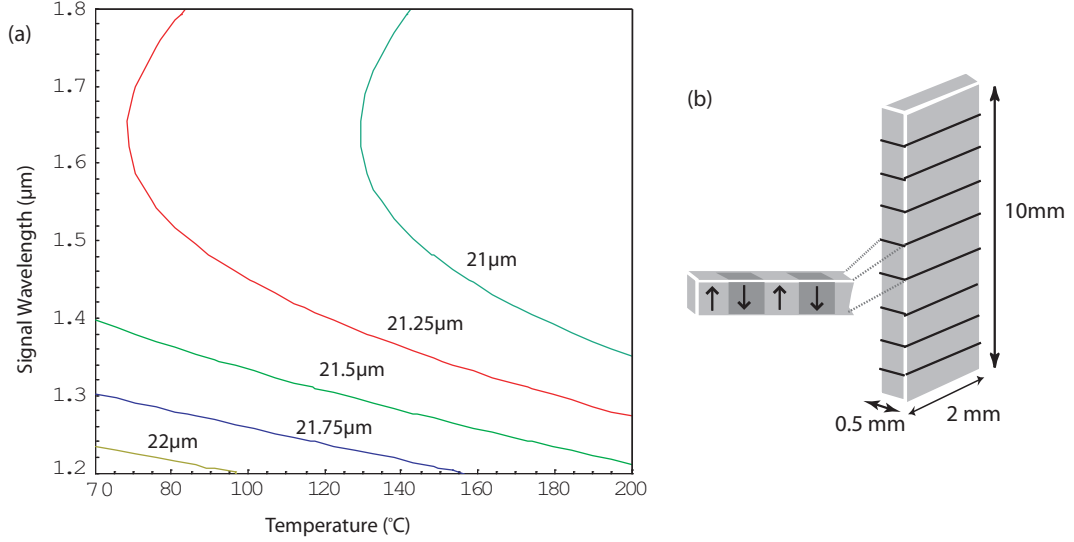


Figure 3.4: (a) Temperature tuning curves for a few of the PPLN grating used, indicating the signal wavelength range attainable. (b) Schematic of the PPLN crystal used.

One further consideration is the required length of the PPLN crystal. Due to the different refractive indices experienced by the three waves, the pump and signal group velocities ($v_{g,p}$ and $v_{g,s}$) will differ and the temporal walk-off will increase through the medium. The crystal length (l_w) (given in equation 3.10) was chosen to approximately match the temporal offset limit given by half the desired pulse-width (τ_p), as the conversion efficiency is reduced thereafter,

$$l_w = \frac{\tau_p}{2(v_{g,p}^{-1} + v_{g,s}^{-1})}. \quad (3.10)$$

Dispersion compensation

The pulses produced in the optical cavity have a finite spectral bandwidth, and therefore upon transit through optical elements in the resonator they become temporally separated by dispersion (as mentioned previously). In extremely high intensity pulses this can also lead to reshaping and break-up. In order to compensate for this, typically positive group velocity dispersion (GVD), OPO cavities need to include some means of negative GVD in order to maintain zero dispersion around the cavity. The common approach is to use a set of 4 prisms, which maintains the spatial separation of the beam [8]. In the OPO constructed for this thesis we used only two prisms, utilising the wavelength dependent

refraction and variable separation between them. The output is spatially separated, which also allows additional bandwidth control by way of a movable slit placed in the cavity.

Using equations for the second order dispersion [9], and the refractive indices for the PPLN and the prism glass (SF14) via the Sellmeier equations we could solve for the zero dispersion point. Using an estimate for the beam size, this gives an approximate separation for the prisms in the cavity. For a wavelength of $1.3\mu\text{m}$ and 6mm of total prism glass, the optimum prism separation was $\approx 28\text{cm}$.

3.2.4 OPO cavity

The asymmetric frequency conversion that leads to generation of signal and idler gives OPOs great flexibility in their spectroscopic application. However the single pass gain for the conversion process is extremely low and for this reason a resonating cavity is required. The design chosen was a singly resonant oscillator (SRO), in which only the signal wave ($1.25\text{-}1.55\mu\text{m}$) was made to oscillate. This has the advantage of increasing the cavity stability as the cavity elements can be optimised for a smaller wavelength range, however the overall gain is reduced and the threshold is increased. The cavity was a 4 mirror 'W' configuration and was synchronously pumped by a femtosecond mode-locked Ti:Sapphire laser, as shown in fig 3.5. The mirror angles were kept to a minimum to avoid losses and astigmatism. This pumping scheme requires precise matching of the cavity lengths of both the Ti:Sapphire laser and OPO cavity (1.83m), to within the pulse duration ($< 60\mu\text{m}$). This is so that when the signal pulse returns to the crystal after successive cavity round trips, it meets an incoming Ti:Sapphire pulse which replenishes the gain.

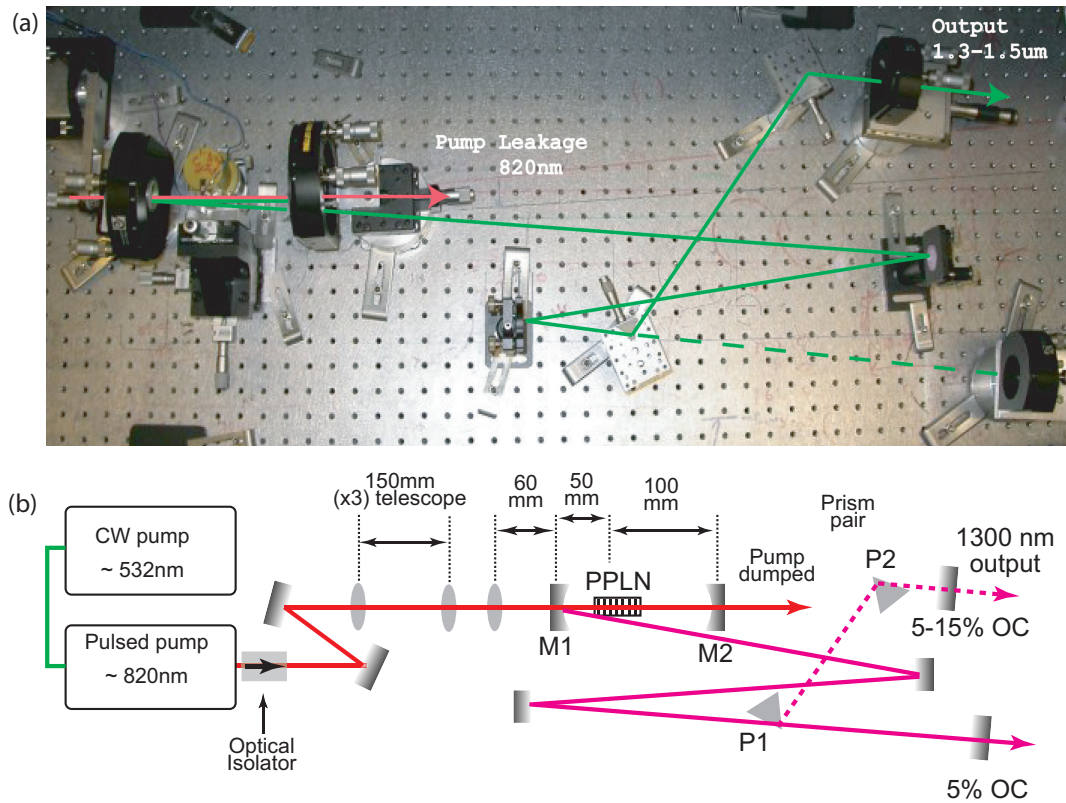


Figure 3.5: (a) Photograph of the completed fs OPO used for time-resolved measurements in this thesis. (b) Schematic of fs OPO indicating the elements involved.

Any mismatch in cavity length reduces the conversion efficiency however, adjusting the length via the output coupler gives an added flexibility in wavelength tuning. In order to optimise the focussing, a telescope was placed outside the cavity which magnifies the beam diameter ($3\times$) prior to focussing into the PPLN, with a diameter $\sim 30\mu\text{m}$. A non-reciprocal (Faraday) Isolator was placed between the pulsed laser and the OPO in order to prevent pulses returning to the pump laser and affecting the mode-locking.

Alignment

Initially the telescope, focusing lens, mirror M1 and the PPLN crystal are placed in the pump beam. When a Ti:Sapphire pump pulse passes through the crystal blue light is generated (due to frequency doubling in the crystal) in the forward and backward direction. The angle of the PPLN is adjusted to send this blue light back as far as possible on the line of the pump beam. The second cavity mirror (M2) is now added in order to reflect the forward converted blue light back through the crystal onto M1. This mirror is now

adjusted to direct the two blue spots in the forward direction but to the side of the crystal. These two blue spots are required to be collinear (see fig 3.6) in the far field and this is achieved with the adjustment of M2 (near field) and M1 (far field).

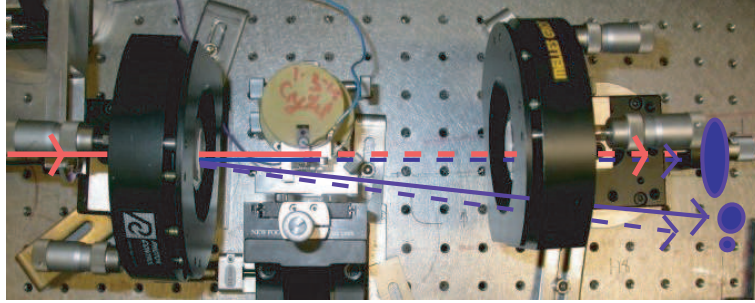


Figure 3.6: Photograph of PPLN in the resonator indicating the frequency doubled blue light which is critical for aligning the resonator and obtaining oscillation.

The remaining mirrors are inserted into the cavity and a 98% output coupler (OC) is used to approximately length match the cavity to that of the pump laser. A pin hole is used to adjust the weakly focussed blue spots back as close to the PPLN as possible, overlapping in both the forward and backward directions. Now the length of the cavity is finely adjusted until oscillation is achieved, indicated by a green/red flash due to frequency conversion of the resonant signal wavelength in the PPLN.

P1 is inserted at Brewster's angle to pick off a small amount of the pump laser whilst maintaining oscillation of the cavity. The second prism P2 is placed $\sim 28\text{cm}$ away to direct the pump beam towards a second OC (output = 85%). With the use of a pinhole and an infrared detection card the OC is adjusted to send the beam back to P1. More prism glass can now be inserted in the beam path until oscillation just stops. The second OC is now adjusted to instigate oscillation of the second cavity. Once the second cavity is stable the OPO was enclosed in a box with a removable lid to reduce air currents and stabilise the output further.

3.2.5 The pump laser system

The development of stable pump sources has been paramount to the development of OPO's since the early 90's, using Nd:YAG [3] and more importantly Ti:Sapphire [4] lasers. The discovery of Kerr lens modelocking [10], which is responsible for sustaining stable fs pulses

in Ti:Sapphire, lead to a plethora of femtosecond OPO developments due to the vast improvement in stability. In addition, the replacement of gas lasers (Argon ion) with all solid state equivalents for pumping of the Ti:Sapphire lasers has also dramatically increased the overall pumping efficiency by way of improved beam quality.

Ti:Sapphire femtosecond laser

Ti:Sapphire ($Al_2O_3 : Ti^{3+}$) is a sapphire crystal doped with titanium ions, which exhibits a vibronic spectrum allowing a large wavelength tuning range (600-1100nm). This large bandwidth can also be utilised to generate ultrashort pulses. It absorbs in the wavelength range 400-600nm, however the efficiency is highest between 514-532nm. In this regard pumping with Argon ion (514.5nm), frequency doubled Nd:YAG or Nd:VO₄ (532nm) is more common, the later having higher beam quality. The laser used to the pump the OPO in this thesis was a Spectra Physics (Tsunami) model which is kerr lens modelocked to produce 150fs pulses at a repetition frequency of 82MHz. The modelocking mechanism is started and stabilised by way of an intracavity acousto-optic modulator. A set of four intra-cavity prisms is used for pulse compression and dispersion compensation in the laser.

CW laser

The Ti:Sapphire pump laser was itself pumped via a continuous wave Spectra Physics (Millenia V). It consists of a Nd:VO₄ crystal (1064nm), frequency doubled by way of birefringent phasematching in an intracavity Lithium Triborate (BBO) crystal giving 5W at 532nm. This is itself pumped via diode bars of 20W at 815nm, supplied to the laser head via optical fibres.

3.2.6 Pulse diagnostics

Two photon absorption (TPA) autocorrelator

In order to have real time measurements of sub-picosecond pulses it is not possible to use conventional photodetectors, as they simply do not have the required response time (typically 50GHz). The common method to measure ultrashort optical pulses is the autocorrelation technique (a comprehensive explanation can be found in Diels [11]). The autocorrelation function compares the correlation between two identical pulses with a

variable time delay between them. In practice the time delayed replica pulses are generated by splitting a laser pulse train using a Michelson interferometer. The correlation is recorded as the overlapping pulses probe an intensity dependent nonlinearity in some chosen material. One retroreflector of the interferometer was mounted on an oscillating loudspeaker, whilst the other is mounted on an x,y,z translation stage for beam alignment. The two beams recombine and are focussed onto a TPA detector (InGaAsP photodetector) allowing them to interfere, as shown in figure 3.7. The benefit of using a commercial semiconductor detector is the low cost and small footprint on the bench [12].

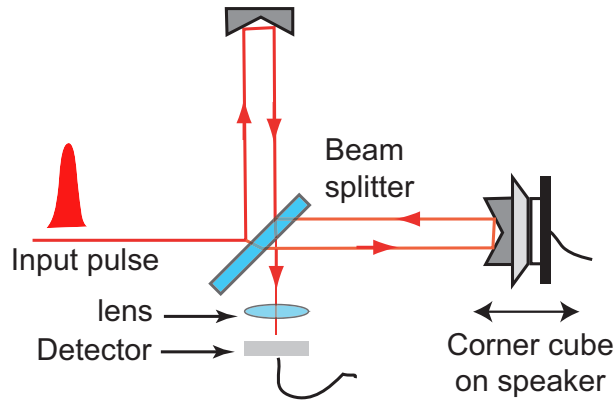


Figure 3.7: Schematic of the autocorrelators used in estimating the pulse durations of the Ti:Sapphire and OPO lasers. Two such setups were built with suitable TPA detectors for 820nm and 1300nm respectively.

The detector signal was displayed on an oscilloscope, triggered by the electrical signal driving the loud speaker. A zero delay between the pulses gives a maximum TPA signal and when there is no overlap of pulses the detector gives a background signal. The autocorrelator is calibrated by translating the usually stationary retroreflector with a micrometer and observing the movement of the signal on the oscilloscope. The one assumption that must be made with an autocorrelation is the pulse shape, which is usually taken as either Gaussian or $sech^2$.

With unlimited bandwidth resolution it is possible to record interferometric autocorrelations, when considering the electric field envelopes of the overlapping pulses as follows,

$$\mathbf{E}(t) + \mathbf{E}(t - \tau). \quad (3.11)$$

Where τ is the delay introduced between the two pulses. The optical field can be expressed mathematically with a carrier frequency ω_0 and a phase $\phi(t)$,

$$\mathbf{E}(t) = A(t) \cos[\omega_0 t + \phi(t)]. \quad (3.12)$$

The signal generated by the intensity profile of the overlapping pulses in the nonlinear material, contains rapidly varying terms around ω_0 and $2\omega_0$. In our case the slow frequency response of the system only allows detection of terms around zero frequency. Consequently the autocorrelator records the time-averaged intensity autocorrelation revealing no phase information as,

$$g(\tau) = 1 + \frac{2 \int_{-\infty}^{\infty} [I(t)I(t - \tau)] dt}{\int_{-\infty}^{\infty} I(t)^2 dt}. \quad (3.13)$$

Ideally the intensity autocorrelator is symmetric about zero delay and has a peak to background ratio of 3:1. The full width at half maximum (FWHM) can be expressed as follows, where $\Delta\tau_p$ is the pulse duration, Δt_i is the measured autocorrelation and k_i is the deconvolution factor relating the shape to the optical field envelope,

$$\Delta\tau_p = \frac{\Delta t_i}{k_i}. \quad (3.14)$$

As no information is available regarding the optical phase, one way to assess the frequency chirp in the pulses is to compare the time-bandwidth product (TBP) ($\Delta\nu\Delta\tau_p$) with that for a chirp free (transform limited) pulse. For a given pulse shape these parameters are given below. Both the Ti:Sapphire and OPO pulses exhibited values close to the transform limit with pulse durations of 200fs and 250fs respectively.

Field envelope	k_i	$\Delta\tau_p\Delta\nu$
Gaussian	1.414	0.441
<i>sech</i> ²	1.543	0.315

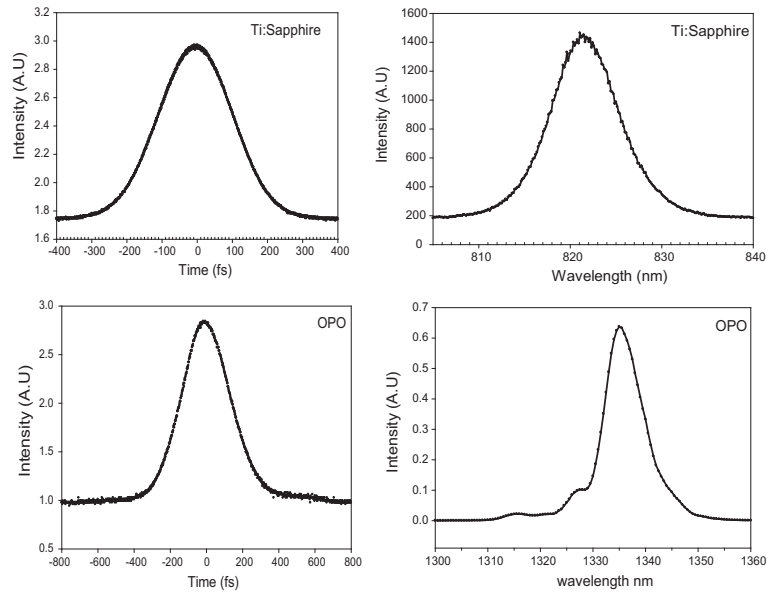


Figure 3.8: Typical intensity autocorrelations and spectra obtained for the Ti:Sapphire and OPO pulses. With gaussian fitting TBP values were 0.558 and 0.441 respectively.

Spectral measurements

For measuring the spectra of the Ti:Sapphire pulses, an Ocean Optics silicon spectrometer was used. This also allowed realtime monitoring of the modelocking process. To monitor the spectra of the OPO laser, a Rees 241 IR spectrometer was used. After initially connecting to an oscilloscope, this allowed realtime measurement of the spectra and subsequent adjustment of the cavity elements in order to maintain approximately transform limited pulses. The REES spectrometer works in the range 800-1600nm and recorded spectra, but offered low resolution. For high resolution measurements (such as those in fig 3.10) a 1/4m monochromator was used with a germanium detector at the output. This last setup however was not practical for real-time monitoring.

3.3 Characterisation of the OPO

In order to measure the spatial beam profile of the OPO output once collimated, a germanium detector was placed on a x,y translation stage with a pin hole fixed to the front. The detector was translated through the horizontal and vertical centre of the beam and the data fitted with a Gaussian profile, as shown in fig 3.9.

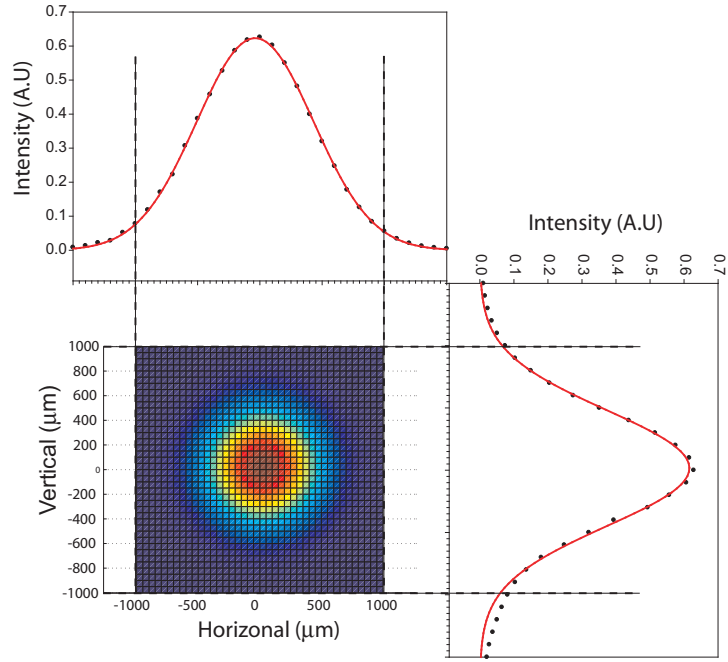


Figure 3.9: Horizontal and vertical profile of OPO beam, fitted with a Gaussian function.

3.3.1 Length tuning

It was found that cavity length tuning, gave a more readily accessible amount of wavelength selection than changing between gratings. For a pump wavelength of 820nm and grating of $21.25\mu\text{m}$ the pulse spectra and corresponding autocorrelations are shown in fig 3.10.

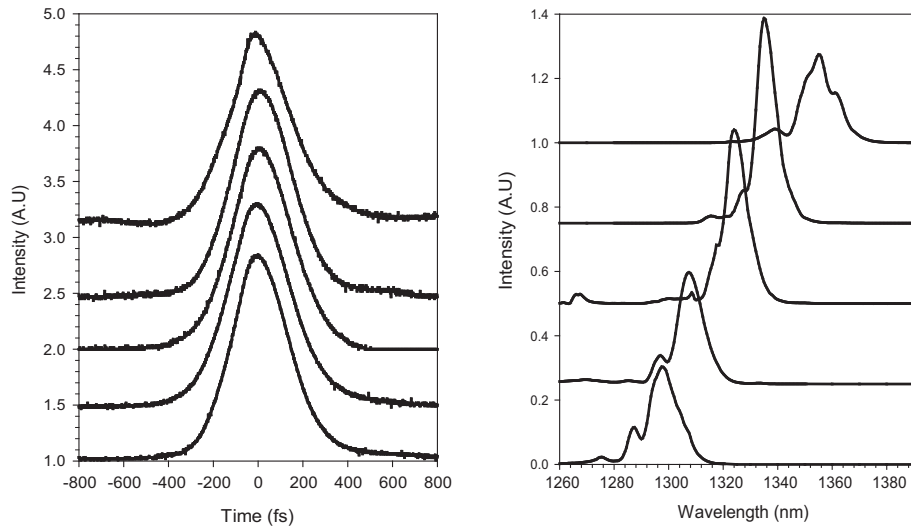


Figure 3.10: Autocorrelations and associated spectra for a range of OPO outputs using only the length to tune the wavelength.

The reason the spectra appear relatively chirp free over a small wavelength range from changing the cavity length alone is due to the small amount of positive group delay dispersion (GDD) in the PPLN crystal. As the cavity increases the resonant wavelength increases and this reduces the net GDD. However as this is further increased the pulses acquire chirp which needs to be compensated for with the intracavity prisms. However fig 3.10 was recorded for a fixed prism pair and indicates the available tunability from length tuning alone.

3.3.2 Power measurements

For the grating ($\Lambda = 21.25\mu\text{m}$) the output was measured on a calibrated power meter over the full extent of the wavelength tuning range. The results are shown in fig 3.11 below.

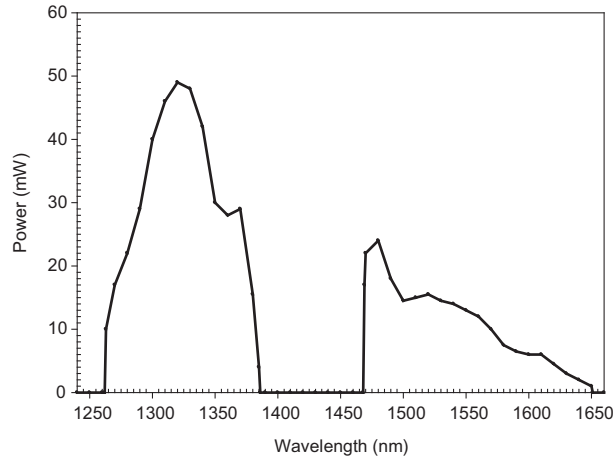


Figure 3.11: Output power for the OPO laser as a function of wavelength with grating $21.25\mu\text{m}$.

The power output versus wavelength, by length tuning follows the typical reflectivity spectra of the mirror coatings. This particular grating and temperature of 150°C was typically used for measurements of samples in the $1.3\mu\text{m}$ due to the high output power, using a 15% output coupler. One observation was the large amount of visible green light produced at wavelengths around the dip of 1500nm (see fig. 3.11), accounting for approximately $2/3$ of the output power at at this wavelength. One explanation for this could be third harmonic generation (THG) of the signal (which is the only resonant wave in the cavity) caused by high order quasi-phases matching. Similar results have been reported previously where high order second harmonic generation (SHG) of the resonant pump was accountable [13].

3.3.3 Grating and temperature tuning

Temperature tuning was performed from 100 – 200 °C. The results were taken at a pump wavelength of 820nm for a few of gratings around 21.0 μ m. It must be noted that the curves predicted by the Sellmeier equation approximation, indicate the maximum of the normalised gain coefficient. This falls off rapidly either side of the black curve as mentioned previously.

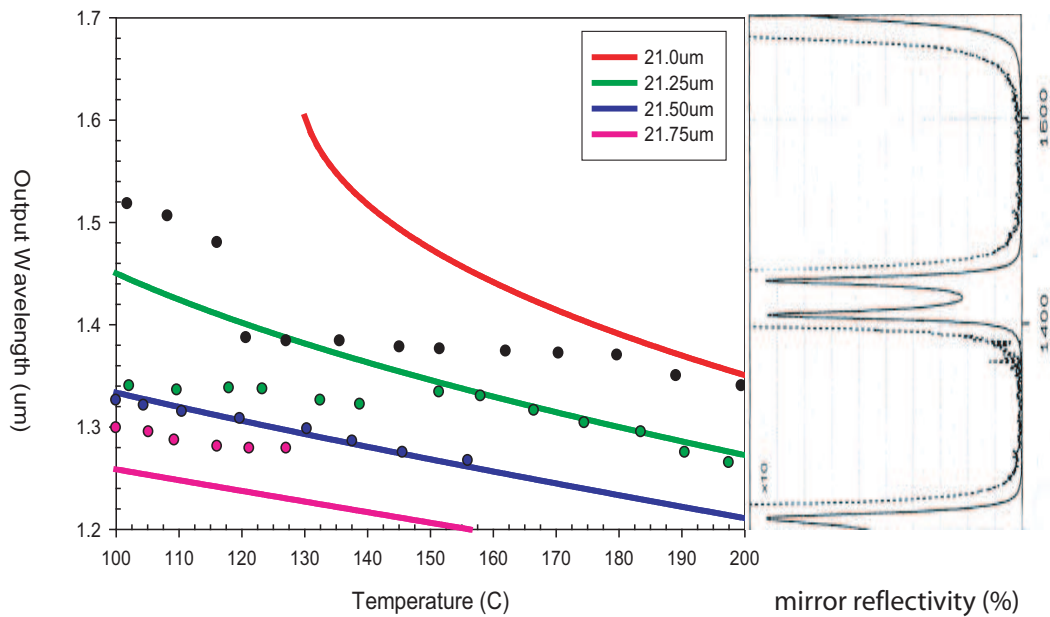


Figure 3.12: Temperature tuning curves for a sample of gratings used including experimental data for the PPLN crystal. Included on the right side is the bandwidth data for the high reflection coatings used on the OPO mirrors.

The experiential points plotted in fig 3.12 refer to the most stable wavelengths achievable after length tuning. The variation of the signal wavelength follows the direction and the rate of the temperature tuning predicted by the Sellmeier equation (solid lines in fig. 3.12). However, by considering the bandwidth limitations imposed by the mirror coatings, the upper wavelength limit is actually due to the cut off in reflectivity rather than the reduction in gain of the PPLN. To this end the temperature tuning is more useful for fine adjustment of the wavelength required.

3.4 Supercontinuum generation for linear measurements

In order to carry out broadband absorption measurements in the semiconductor samples, a microstructured optical fibre was pumped with 20fs pulses from a Ti:Sapphire laser. The pulses experience extremely large dispersion which generates an almost continuous wave spectrum from 400-1600nm. With the inclusion of a 1/4m monochromator, this created a tuneable source with suitable power for optical transmission measurements.

3.4.1 Dispersion in optical fibre

Dispersion is the temporal separation of waves propagating in a material due to the frequency dependence of the system properties. There are generally two types of dispersion: Material dispersion and Waveguide dispersion. The former is a consequence of the wavelength dependence of the material by way of the refractive index. The latter is dispersion due purely to geometrical reasons, independent of the frequency response of the material itself.

For waves confined laterally in waveguides such as optical fibres, there exists transverse modes. This introduces the idea of modal dispersion where a number of different transverse modes may co-exist for a particular frequency and they propagate at different rates due to their different geometrical paths through the fibre. A special case of this is polarisation mode dispersion (PMD) which is when two modes travel at different rates due to imperfections that break the symmetry of the waveguide. This can occur naturally due to birefringence (when the polarisation state of a mode can be resolved into two orthogonal components which propagate at different rates) or artificially by engineering the core of the waveguide. In the special case of a single transverse mode (single mode fibre) which contains different wavelengths, the longer wavelengths have more power in the evanescent cladding mode than in the core. As a consequence the waveguiding diminishes as the effective index in the core approaches that of the cladding, this is termed intramodal dispersion as opposed to intermodal dispersion mentioned above for the case of multiple transverse modes.

In single mode fibres the zero-dispersion wavelength is the point at which material dispersion and waveguide dispersion cancel one another. In optical communications the

index profile of fibre is altered to make the waveguide dispersion more negative and thus moving the zero-dispersion point from its natural value of 1310nm, closer to the absorption minimum of 1550nm [14].

3.4.2 Nonlinearities in optical fibre

As mentioned previously, the polarisation is dependent on both linear and nonlinear effects. When intense fields are present nonlinear susceptibilities can be excited. SiO₂ fibres are amorphous and therefore have inversion symmetry, so $\chi^{(2)} = 0$ and therefore $\chi^{(3)}$ becomes the lowest order nonlinearity to be excited. The $\chi^{(3)}$ gives rise to the Kerr effect giving and intensity dependent refractive index (n_2) where,

$$n = n_0 + n_2 I = n_0 + \left(\frac{n_2}{A_{eff}} \right) P. \quad (3.15)$$

Firstly, parametric (energy conserving) processes can be described by a real nonlinear susceptibility. These include Third harmonic generation (THG), Cross-phase modulation (XPM) and Self-phase modulation (SPM). The processes that have a complex susceptibility are inelastic scattering processes, namely Stimulated Brillouin Scattering (SBS) and Stimulated Raman Scattering (SRS). These latter processes occur when intense light beams interact with acoustic and optical phonons respectively [15]. An input photon is destroyed and a lower frequency photon is generated through the stokes field, and this wave modulates the refractive index in turn modulating the phase of the input light. The threshold power of SRS is much greater than that of SBS, as is the gain bandwidth (typically 40THz and 100MHz respectively). However neither contribute significantly to continuum generation. The nonlinear coefficient mentioned above $n_2(m^2W^{-1})$ is related to the nonlinear parameter $\gamma(W^{-1}km^{-1})$ as follows [16],

$$\gamma = \left(\frac{\omega n_2}{c A_{eff}} \right) = \left(\frac{2\pi n_2}{\lambda A_{eff}} \right). \quad (3.16)$$

Where c is the speed of light and A_{eff} is the effective area of the optical fibre. Typical values for the nonlinear coefficient of optical fibre are $2 - 3 \times 10^{-20} m^2 W^{-1}$. Dopants, for example bismuth, can be added to the core to increase the nonlinear parameter as high as $1360 W^{-1} km^{-1}$ [17]. In addition the core and cladding can be engineered to change the

effective area of the fibre by changing the index profile of the mode [18]. One extreme example of this is microstructured fibre, which incorporates a photonic crystal structure in order to tightly confine the transverse optical mode.

3.4.3 Microstructured fibre and continuum generation

The first demonstration of continuum generation in microstructured fibre used 100fs pulses and produced an output from 400nm - 1600nm [19]. The photonic crystal fibre (PCF) used in our work is an engineered single mode waveguide, consisting of a silica core surrounded by a holey cladding. This dramatically increases the index contrast and thus lowers the effective area. The core is doped with GeO_2 and the zero-dispersion wavelength is shifted to approximately 750nm, such that optical pumping of this fibre with a Ti:Sapphire laser occurs in the anomalous dispersion regime. The reason for this is due to soliton generation, which occurs via the interplay of SPM and anomalous group velocity dispersion (GVD). When the length of fibre is such that the nonlinear phase shift due to SPM is counteracted by the dispersion shift due to the GVD, then a pulse will travel down the fibre showing no appreciable broadening behaviour (Soliton). The solution to the nonlinear Schrodinger equation (NLSE) then gives the soliton order as,

$$N = \left(\frac{\gamma T_0^2 P_0}{|\beta_2|} \right)^{1/2}. \quad (3.17)$$

Where P_0 is the input power, T_0 is the soliton width, whilst β_2 is the two photon cross section in the NLSE. Solitons experience a power dependent shift to longer wavelengths due to the Raman effect, known as the Soliton self-frequency shift (SSFS) [15]. This alone can be used to generate a tuneable Stokes field for the use in time resolved coherent anti-stokes Raman scattering (CARS), which has many uses in molecular spectroscopy [20]. If on the other hand, significantly higher powers are launched into a fibre the fundamental soliton breaks up to form higher order solitons which are narrower and individually red-shifted. At the same time they emit nonsolitonic (Cherenkov) radiation [21], which for the anomalous dispersion regime is shifted to shorter wavelengths. Each high order soliton exhibits this where the radiation field is phase-matched to the soliton. These spectra then overlap in frequency generating a continuum. An example of the output spectrum from

such a commercially available PCF fibre pumped by 20fs Ti:Sapphire laser pulses, which was used for transmission measurements in chapter 5 is shown in fig. 5.7.

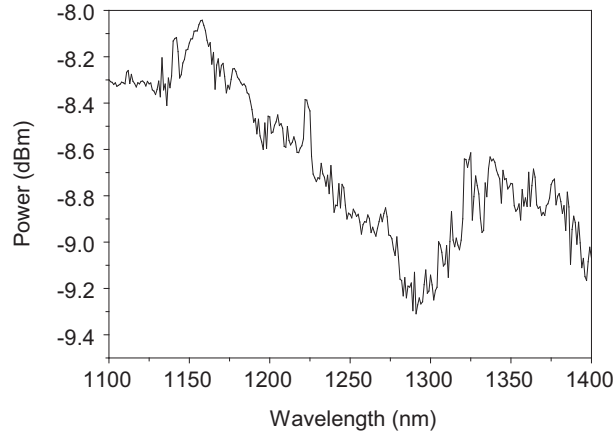


Figure 3.13: Supercontinuum spectrum from FEMTOWHITE 800 pumped with 400mW Ti:Sapphire laser with 20fs pulses at 780nm

The FEMTOWHITE 800 comprises a 12cm length of microstructured single mode PCF ($\gamma = 95W^{-1}km^{-1}$ at 750nm) enclosed in an aluminium casing 1" in diameter, to allow clamping via standard optic mounts. Due to the high energy of pulses incident on the device ($>10nJ$), the fibre is thermally collapsed in the end regions to increase the damage threshold to that of fused silica. The spot size in the raw fibre is $1.6\mu m$, which increases to $2.3\mu m$ before the final $100\mu m$ is collapsed up to the facets. This allows the focussed spot size at the facet to be $50\mu m$. This also stops the ingress of contamination to the microstructure and allows the facets to be cleaned. Coupling into and out of the device using Ti:Sapphire pulses was achieved via 40x/60x aspheric microscope objectives respectively.

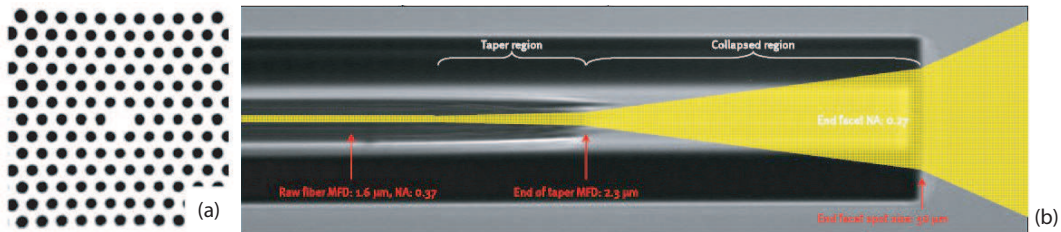


Figure 3.14: (a) Optical microscope picture of a typical single-mode fibre with zero-dispersion around 800nm with hole size $0.5\mu m$. (b) Cut-away schematic of the FEMTOWHITE 800 showing the collapsed region of fibre. Pictures reproduced from Crystal Fibre documentation.

3.5 Summary

The development of the optical sources used for characterising semiconductor samples in this thesis have been detailed. Appreciation of recent developments creating stable solid state pump lasers and microstructured fibres has led to the realisation of such sources. The OPO system was fully characterised and optimised by various tuning parameters explained above. This gives access to a pulsed source of 250fs duration with 50mW of average power in the spectral range 1.25-1.35 μ m for pump probe measurements. The broadband continuum was generated by using a 20fs Ti:Sapphire laser pumping a microstructured optical fibre to give a usable spectrum 1100-1400nm for transmission measurements.

References for Chapter 3

- [1] K Burneika, M Ignatavichyus, V Kabelka, A Piskarskas, and A Stabinis. Parametric light amplification and oscillation in KDP with mode-locked pump. *IEEE J. Quantum Electron.*, 8:574, 1972.
- [2] M H Dunn and M Ebrahimzadeh. Parametric generation of tunable light from continuous-wave to femtosecond sources. *Science*, 286:1513–1517, 1999.
- [3] L E Myers, R C Eckardt, M M Fejer, R L Byer, W R Bosenberg, and J W Pierce. Quasi-phase-matched optical parametric oscillators in bulk periodically poled $LiNbO_3$. *J. Opt. Soc. Am. B*, 12(11):2102–2116, 1995.
- [4] D T Reid, G T Kennedy, A Miller, W Sibbett, and M Ebrahimzadeh. Widely tunable, near-to mid-infrared femtosecond and picosecond optical parametric oscillators using periodically poled $LiNbO_3$ and $RbTiOAsO_4$. *IEEE J. Sel. Top. Quantum Electron.*, 4(2):238–248, 1998.
- [5] E Hecht. *Optics*. Addison Wesley publishing, 4th edition, 2003.
- [6] Y J Ding and J B Khurgin. Second harmonic generation based on quasi-phase matching: A novel configuration. *Optics Lett.*, 21(18):1445–1447, 1996.
- [7] D H Jundt. Temperature-dependent Sellmeier equation for the index of refraction, n_e , in congruent lithium niobate. *Opt. Lett.*, 22(20):1553–1555, 1997.
- [8] R L Fork, O E Martinez, and J P Gordon. Negative dispersion using pairs of prisms. *Opt. Lett.*, 9(5):150–152, 1984.
- [9] R L Fork, C H Brito Cruz, P C Becker, and C V Shank. Compression of optical pulses to six femtoseconds by using cubic phase compensation. *Opt. Lett.*, 12(7):483–485, 1987.
- [10] D E Spence, P N Kean, and W Sibbett. Regeneratively initiated self-mode-locked Ti:Sapphire laser. *Opt. Lett.*, 16(42), 1991.
- [11] J-C Diels and W Rudolph. *Ultrashort laser pulse phenomena*. Academic Press, London, 1996.
- [12] D T Reid and W Sibbett. Commercial semiconductor devices for two photon absorption autocorrelation of ultrashort light pulses. *Opt. Photonics News*, 9(5):SupL6–8, 1998.
- [13] C McGowan, D T Reid, Z E Penman, M Ebrahimzadeh, W Sibbet, and D H Jundt. Femtosecond optical parametric oscillator based on periodically poled lithium niobate. *J. Opt. Soc. Am. B*, 15(2):694, 1998.
- [14] L G Cohen, C Lin, and W G French. Tailoring zero chromatic dispersion into the 1.5-1.6 μ m low-loss spectral region of single-mode fibres. *IEE Elect. Lett.*, 15(12):334–335, 1979.
- [15] G P Agrawal. *Nonlinear fiber optics* 3rd edition. Academic press, 2001.
- [16] L Prigent and J-P Hamaide. Measurement of fiber nonlinear kerr coefficient by four-wave mixing. *IEEE Phot. tech. lett.*, 5(9):1092–1094, 1993.
- [17] N Sugimoto, T Nagashima, T Hasegawa, and S Ohara. Bismuth-based optical fiber with nonlinear coefficient of $1360W^{-1}km^{-1}$. *Optical fiber communication conference 2004*, 2004.
- [18] K P Hansen and R E Kristiansen. Supercontinuum generation in photonic crystal fibers. *Crystal fibre: Application note*, 2006.
- [19] J K Ranka, R S Windeler, and A J Stenz. Visible continuum generation in air-silica microstructure optical fibers with anomalous dispersion at 800nm. *Optics letters*, 25(1):p25–p27, 2000.
- [20] D A Sidorov-Biryukov, E E Serebryannikov, and A M Zheltikov. Time-resolved anti-Stokes Raman scattering with a femtosecond soliton output of a photonic crystal fiber. *Optics Letters*, 31(15):p2323–p2325, 2006.
- [21] N Akhmediev and M Karlsson. Cherenkov radiation emitted by solitons in optical fibers. *Physical review A*, 51(3):p2602–p2607, 1994.

Chapter 4

Characterisation and Fabrication of active waveguide devices

4.1 Introduction

In order to successfully investigate electric field effects in active waveguides, some basic characterisation of the electrical and optical properties was carried out. Three devices were ultimately used in this thesis. The first was a quantum-dot-in-well (DWELL) p-i-n waveguide supplied by Ioffe Institute, St Petersburg, Russia. The second was a bilayer quantum dot p-i-n waveguide supplied from Imperial College, London. The final device was fabricated as part of this work at St Andrews, using a MQW GaInNAs wafer supplied by the Optoelectronic Research Centre (ORC) at the Technical University of Finland. This chapter will introduce the devices used for subsequent reverse bias measurements and their characterisation under forward bias, this being essential in order to obtain useable devices. The measurements begin by investigating the isolated dots in a quantum well (DWELL) as the active region. Thereafter we look at the strain engineered bilayer QDs for extending the wavelength emission beyond $1.3\mu\text{m}$. Finally GaInNAs MQWs emitting at $1.3\mu\text{m}$ are used as active material and the fabrication of these devices will also form part of this chapter.

4.2 Experimental setup: Spontaneous emission (SE)

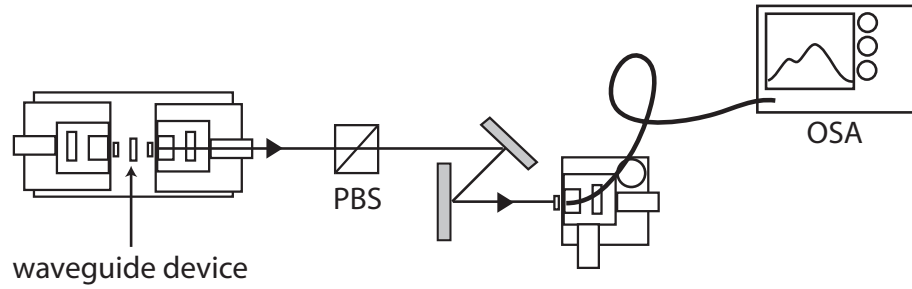


Figure 4.1: Schematic for the measurement of spontaneous emission (SE) from waveguide samples, using TE and TM polarised beams. The optical spectrum analyser (OSA) is calibrated and gives absolute power.

The spontaneous emission (SE) was measured directly with the use of a polarising beam splitting cube (PBS) and an optical spectrum analyser (OSA) as shown in figure 4.1. The devices were mounted on copper fixings and then on a brass mount which contained a thermo-electric cooling element coupled to a thermistor placed close to the device. This maintained the device at room temperature. Electrical probes combined with a constant current source provided the electric bias via gold contacts on the devices. A 40x aspheric lens was used to couple the light out of the device and directed through the PBS to a fibre mounted on a xyz translation stage (to optimise the coupling). A large area germanium detector was used to optimise the coupling and focus the ASE into the fibre, before being connected to the OSA. The OSA contains a diffraction grating and detector calibrated to give absolute power. This gave an improved measurement technique to that of some previous measurements, using a monochromator and germanium detector. In fact figure 4.4(a) shows SE for all polarisations on the DWELL device indicating an inherent problem of TE and TM with a monochromator and detector set-up. In order to normalise the SE being detected through a monochromator it is essential to calibrate the grating with a known source. However gratings are polarisation sensitive and differ in their response to TE and TM light. It was not possible to achieve a TE or TM white light source for calibration due to the limited spectral bandwidths of the polarisers used with the halogen lamp. One is essentially left with a spectral artifact in the ASE spectrum that can not be corrected for and this may mask an actual feature of interest in the sample.

4.3 Sample 101: InAs-InGaAs-GaAs DWELL

Initially, In(Ga)As-GaAs self assembled QDs do not emit beyond approximately $1.2\mu\text{m}$, due to the critical thickness (1.7ML) of InAs that can be deposited before 3D islands begin to form. This lead to a process known as Atomic-Layer-Epitaxy (ALE) where the deposition alternates between Ga and In with a pause of a few seconds under As flux. This allows a greater amount of material to be deposited and forms larger dots, which extends the wavelength [1, 2]. The downside to this is the lower density of dots ($\approx 1.3 \times 10^{10}\text{cm}^{-2}$) which allows the ground state transition to saturate and leads to the lasing transition migrating to the first excited state [3].

Another alternative was proposed by a number of groups which involved the use of a strain reducing cap layer of InGaAs or InAlAs. The reason for this is to control the amount of strain-induced bandgap shift. Free standing dots on GaAs can emit up to $1.53\mu\text{m}$, whilst covering with GaAs matrix, gives a large blue shift with emission at approximately $1.2\mu\text{m}$. This technique was demonstrated with $\text{In}_{0.2}\text{Ga}_{0.8}\text{As}$ giving emission at $1.35\mu\text{m}$ [4]. Along with other work involving the use of QDs in large bandgap material (such as AlGaAs), this demonstrated that the energy level emission of dots was sensitive to the matrix material. Using InGaAs as opposed to AlGaAs was shown to increase the corresponding emission wavelength of InAs dots and this lead to the demonstration of dot-in-a-well (DWELL) QD lasers [5, 6]. It is also believed that strain fields promote the collection of In from the InGaAs to the InAs dots which has the effect of growing slightly larger dots adding to the red-shift of emission, and this is known as 'stimulated decomposition'. This effect can be further promoted by reducing the temperature during the InAs dot deposition stage only, and is known as activated alloy phase separation (AAPS) [7]. The benefit of the DWELL growth method in general, is that the density of dots is comparable to self-assembled QDs grown on GaAs ($5 \times 10^{10}\text{cm}^{-2} - 7 \times 10^{10}\text{cm}^{-2}$). This therefore allows ground state lasing for higher cavity losses, whilst still retaining the extremely low current densities associated with the electrical pumping of QD lasers.

The QD sample used in this thesis was a p-i-n InAs dot-in-a-well (DWELL) waveguide structure, 1.1mm in length with a $6\mu\text{m}$ ridge width. Grown on a Si doped GaAs substrate, the structure is shown in figure 4.2(a). The active region comprised five periods of 2.5

monolayers (ML) of InAs, with 5nm of $In_{0.15}Ga_{0.85}As$ capping (which is approximately the dot height). Following this there is 33nm of GaAs buffer material which avoids electrical coupling of the dot layers. The quantum dots were 15nm in diameter and 5nm in height with a density in each layer of $5 \times 10^{10} cm^{-2}$. Including the active layers, the width of the intrinsic region was $d = 360nm$. Gold contacts were deposited on the top and bottom of the device for electrical contact via probes and the device was mounted p-side up on a copper element. This aided the heat transfer from the device under forward bias conditions.

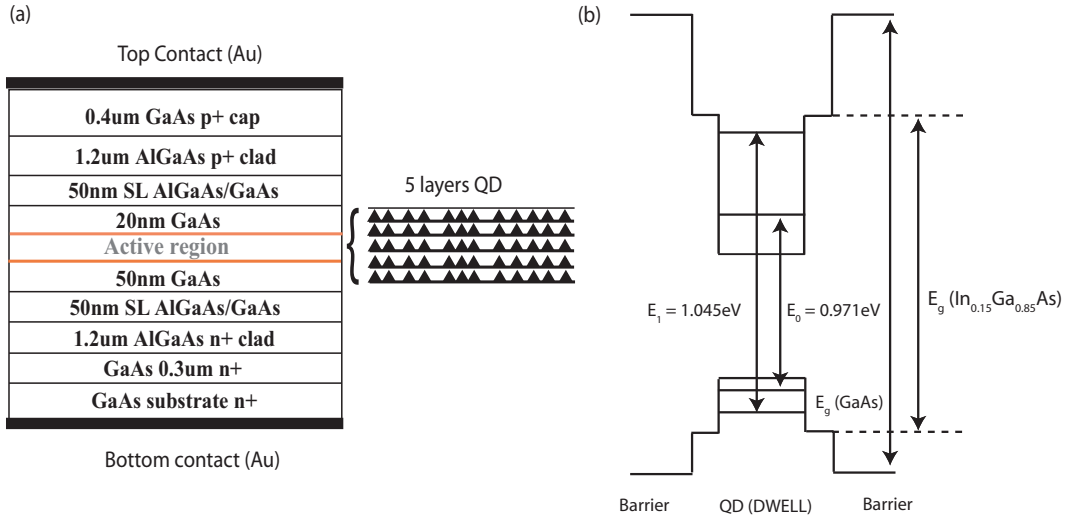


Figure 4.2: (a) Schematic of the wafer used for processed waveguide QD device (sample 101). (b) Schematic of the energy diagram (not to scale).

4.3.1 Spontaneous emission results

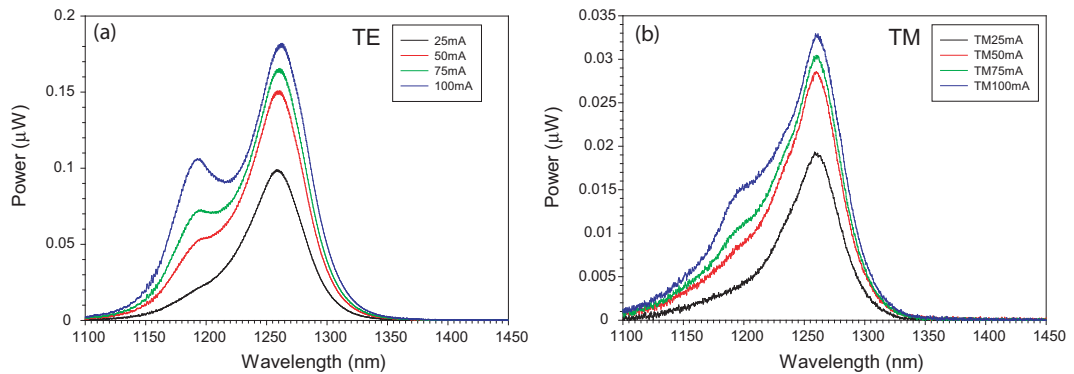


Figure 4.3: Spontaneous emission from (DWELL) QD waveguide (a) TE polarisation and (b) TM polarisation.

The SE spectra show that the emission is predominantly TE polarised which indicates the heavy hole transition. Two peaks are clearly discernable as the ground state at 1280nm and the first excited state at 1190nm. We see no evidence of emission from the wetting layer of the QDs which we attribute to efficient carrier capture into the dots. The facets were not high-reflection coated which explains the lack of lasing up to 100mA, however the excited state emission is still very well suppressed up to high current density ($J = 1515 Acm^{-2}$). One important point to note is the lack of thermal band-gap shift to lower energies.

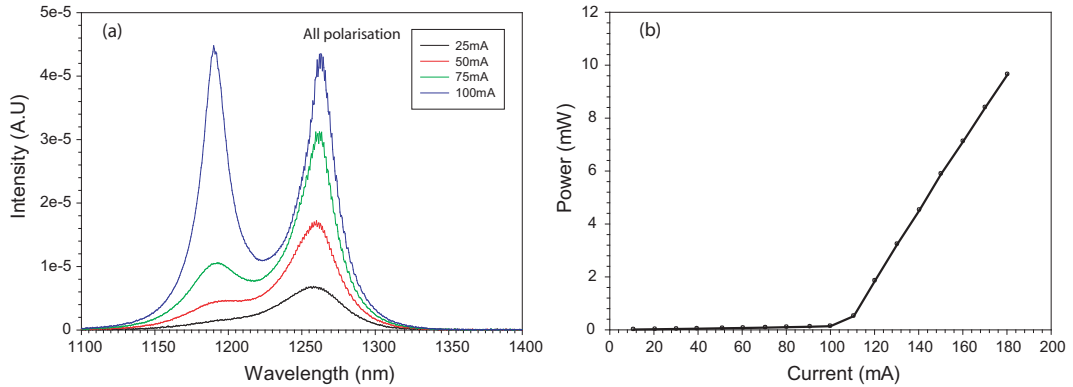


Figure 4.4: (a) Spontaneous emission for all polarisations from (DWELL) QD waveguide (that was damaged). (b) Intensity vs Current curve showing the threshold lasing for the excited state at 104mA of a (DWELL) QD waveguide.

Figure 4.4 shows results for an identical QD device which suffered breakdown of the electrical junction early in this work. The specifications are identical to sample 101 above and show excited state lasing with high threshold current density ($J_{th} = 1575 Acm^{-2}$). However before lasing was initiated, the device showed no signs of thermal roll-over up to levels of threshold current injection (104mA). The amount of amplified spontaneous emission depends on competing processes such as non-radiative recombination events (eg Auger recombination). As more carriers are injected via electrical bias, the increased population of carriers allows more carrier scattering to occur and the non-radiative processes begin to dominate. These results indicate good thermal properties of the material from which the devices were fabricated. As both devices were cleaved from the same sample, these latter results are relevant, in order to indicate the general material quality.

4.4 Sample 102: InAs-GaAs Bilayer QD

InAs/GaAs quantum dots (QD) are proving useful as the active region in a plethora of low threshold optoelectronic devices for operation in the technologically important communications band around $1.3\mu\text{m}$. In particular, the need for greater gain in the active region of such devices has focused attention on the growth of vertically coupled dots [8]. However, for closely placed dot layers the strain fields lead to undesirable In-Ga intermixing in the upper layer and strain relaxation of the lower dot layer [9] making it difficult to control the emission wavelength. Strain-engineered bilayer structures on the other hand, can provide enhanced long wavelength emission and a narrower inhomogeneous line-width with a higher peak gain [10].

The device used in this thesis was a p-i-n structure containing three QD bilayers [10] embedded in an intrinsic GaAs region 500nm thick surrounded by n and p-doped AlGaAs cladding layers. The bilayers have a ground state (GS) photoluminescence (PL) emission at 1340nm. The bilayers were grown by deposition of 2.4 ML of InAs at 0.014 MLs^{-1} onto an annealed GaAs surface at 480°C to form the seed QD layer. This was capped with a 10nm GaAs spacer layer at the same temperature before annealing the surface and then reducing the temperature to 467°C , to deposit 3.3 ML of InAs at the same growth rate, forming the larger QDs of the upper layer. The upper layer was capped with 15nm of GaAs before raising the temperature to 580°C for subsequent GaAs growth. The samples were then processed into ridge waveguide devices 5 - $15\mu\text{m}$ wide, 1mm in length with Au contacts evaporated on the top and bottom and mounted p-side up. GS emission from an isolated seed layer is observed at $\sim 1240\text{nm}$ at room temperature. Injected carriers captured by the seed layer rapidly tunnel into excited states of the larger dots in the upper layer and subsequently relax to the GS which has a transition wavelength of 1340nm.

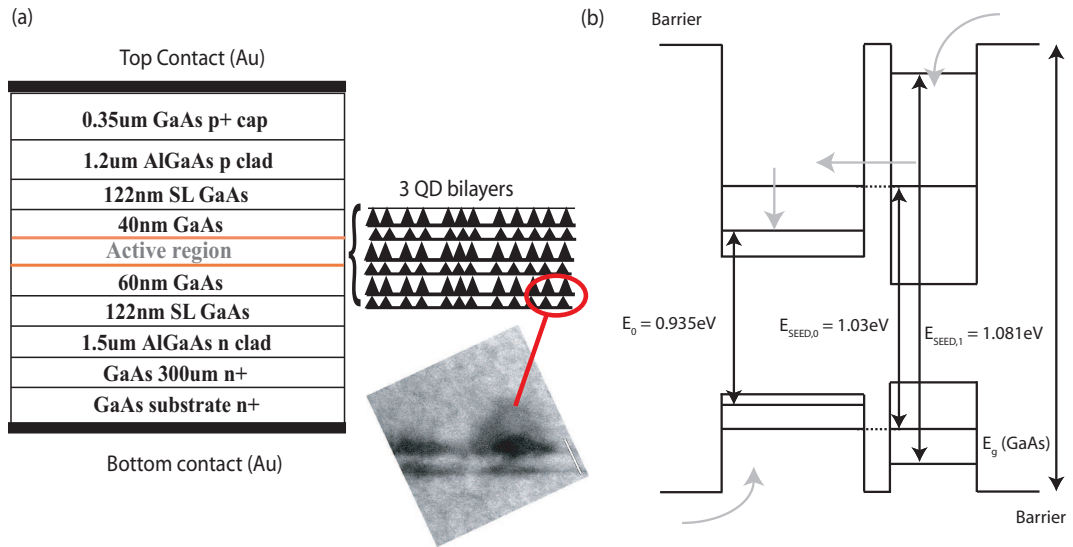


Figure 4.5: (a) Schematic of the wafer used for processed waveguide bilayer QD device (sample 102). TEM image of the bilayer dots (inset). (b) Schematic of the energy diagram (not to scale) for one period of bilayer QDs.

The intermediate layer of GaAs between the first and second layer of dots gives a distance of approximately 5nm between the tip of the first dots and the second layer, which allows for electrical coupling of the system (figure 4.5(b)). The wavefunctions extend over the two dots and allow for rapid capture of electrons from the n-side (under forward bias), whilst holes from the p-side can be directly captured by the larger dots.

4.4.1 Spontaneous emission results

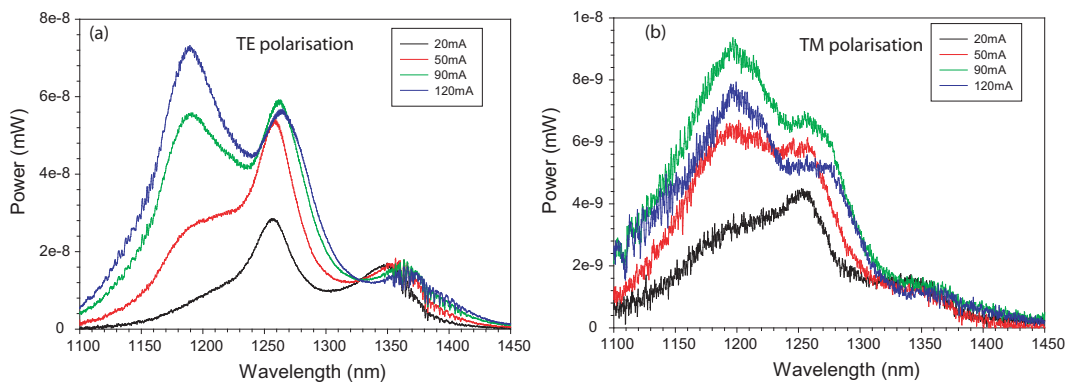


Figure 4.6: Spontaneous emission from a bilayer QD waveguide for (a) TE polarisation and (b) TM polarisation.

From figure 4.6(a) we can see the ground state transition from the larger QDs in the second layer, corresponding to absorption at 1330nm ($E_0 = 0.935eV$). Thereafter the transitions corresponding to absorption of the seed layer ground state at 1240nm ($E_{SEED,0} = 1.003eV$) and that of the excited state at 1150nm ($E_{SEED,1} = 1.081eV$) are identifiable. Again heavy hole transitions appear to dominate the ground state emission due to the preferential TE SE. The ground state can be seen to saturate at moderate current density as the emission from the seed layer excited state indicates. No lasing was identified from this device up to 120mA. This was due in part to the un-coated facets as well as the low gain associated with the relatively low density of the quantum dots ($2 \times 10^{10}cm^{-2}$) and the fact that the device was only 1mm in length.

Figure 4.6 shows the characteristic red-shift of the transitions associated with band-gap shrinking. This arises from the increased thermal energy provided by injection of carriers via electrical bias. As the thermal energy increases, the interatomic spacing gets larger due to the increase in atomic vibrations. An increased interatomic spacing given by the linear expansion coefficient of such material (GaAs), leads to a decrease in the potential seen by the electrons and hence a reduction in the bandgap energy as follows.

$$E_g(T) = E_g(0) - \frac{\alpha T^2}{T + \beta}, \quad (4.1)$$

where α and β are fitting parameters.

4.5 Sample 103: GaInNAs MQW

GaInNAs MQWs have become a very interesting material in the research community [11] due to their ability to extend the wavelength range beyond $1.3\mu m$ in GaAs based devices. It is very different from most III-V quaternary alloys as the nitrogen forms an impurity level in the material, unlike becoming an integral part of the crystal structure. However through conduction band anticrossing, this leads to a direct bandgap semiconductor which exhibits radiative recombination.

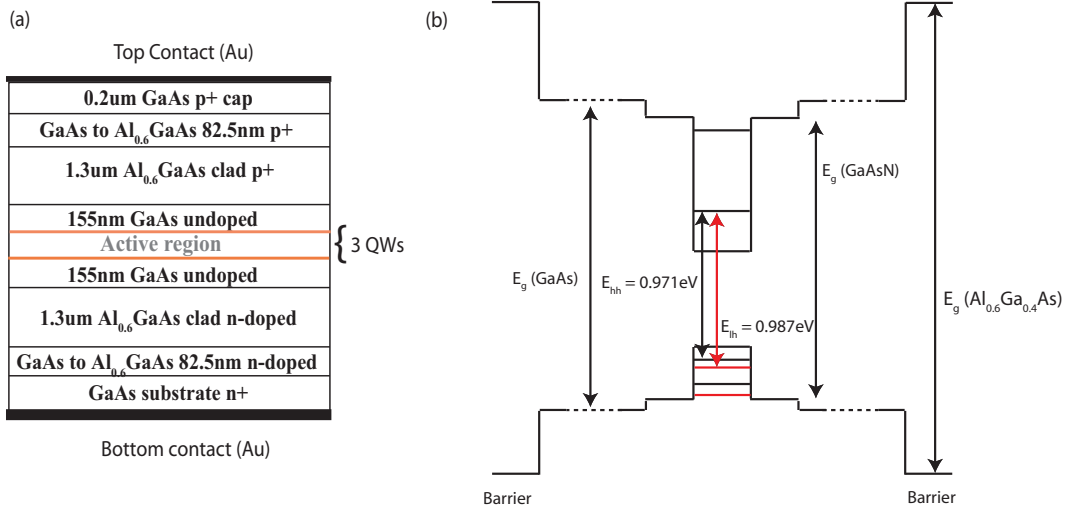


Figure 4.7: (a) MQW GaInNAs wafer structure used for processing waveguide devices. (b) Energy level diagram (not to scale) showing the light hole and heavy hole transitions for one period of MQW structure.

4.5.1 Mode solving with effective index

The lateral variation of refractive index confines optical modes, most notably in optical fibres and waveguides. The change in dielectric susceptibility alters the permittivity of the material and makes up part of Maxwell's equations describing the transverse electric and magnetic fields for such systems. These equation can be readily solved numerically, and one such commercial package that does this is FIMMWAVE, which was used in the design of the GaInNAs waveguides. By systematically changing the etch depth and the ridge width of the design, the supported optical modes can be evaluated.

4.5.2 Photolithography and Ion beam milling

To prepare the sample for processing we initially wash in acetone and then iso-propanol (IPA), before drying in N₂. A dehydration bake at 150 – 200 °C, can also be applied to drive off any adsorbed water from the surface. The sample was glued to a glass slide (for ease of handling) using electron beam photoresist (PMMA). The patterning photoresist (SR1818) was then applied using a spin coating machine, consisting of a vacuum chuck (a hollow metal disk connected to a vacuum pipe) which holds the sample in place. Resist was applied to the sample with a pipette and then a motor spins the sample to 5000rpm for 60s, leaving approximately 1% of the resist remaining on the sample. The resist thickness (T_r)

is critical for good photolithography and is determined by the viscosity and the spin speed by $T_r \propto 1/\sqrt{\omega}$ [12]. Next the sample is placed on a hot plate at 100 °C for 30s in a process called soft baking. This drives off most of the resist solvents leaving approximately 5%. Hard baking (> 100 °C) is undesirable as it can start to drive photo activate mechanisms in the resist leading to dissolution before exposure. The sample is then placed in contact with a chrome/glass mask in the UV exposure machine. The mask used had a mark space ratio of $5\mu\text{m}$ to $95\mu\text{m}$ in order to pattern $5\mu\text{m}$ ridge waveguides. The sample should be in close contact (observing Newton rings just at the edges of the sample and mask) to avoid damaging the resist with force. The sample was then exposed for 30s to the UV lamp, removed and placed in developer (MF319) for 30s. Thereafter it was placed in de-ionised water for 30s and dried with N_2 . The photolithography step is shown in figure 4.8.

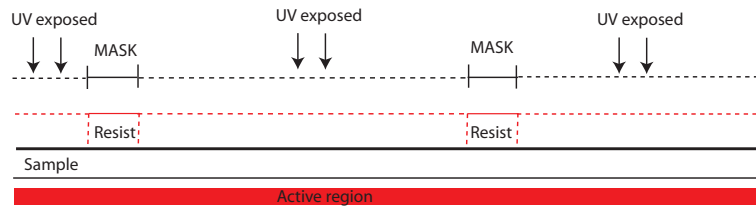


Figure 4.8: Patterning with positive photoresist (SR1818) using UV lamp and chrome/glass mask. Subsequent developing (MF319) leaves a suitable embedded mask on the sample for plasma etching.

photoresist developing

A typical positive resist (exposure to UV breaks the chemical down) consists of a thick resin (Novalac) and a photo activated chemical (PAC) which is usually one of the aromatic polymers known as diazoquinones (DQ), which includes a matrix element nitrogen attached to the benzene ring. This is not itself soluble in a base solution ($\text{pH} > 7$). When exposed to UV light however the nitrogen is freed from the ring leaving a highly reactive site. The adjacent carbon above this site moves out of the ring creating a carbonyl group ($\text{C}=\text{O}$) and a stable ketene by way of the Wolff rearrangement [13]. Upon contact with water (which contains the developing solution) this forms carboxylic acid when a hydroxide group attaches to the carbonyl group. Carboxylic acid on the other hand is soluble in a base solution. The developer (typically KOH or NaOH in water) penetrates the exposed resist and forms a gel, whereby it reacts with the carboxylic acid to form amines and

metallic salts, and is consumed by the reaction. It is therefore necessary to use fresh replenished developer when processing multiple samples. The nitrogen released in the aforementioned reaction also agitates this mechanism and enhances the dissolution [14]. The purpose of the de-ionised water wash after development is to stop this reaction and wash away the gel and salts leaving a high contrast ratio. The unexposed resist is essentially unchanged as the developer does not penetrate here. This then leaves a suitable pattern for plasma etching of sub micron features. At this point the pattern is investigated under a low power lamp and microscope. If the pattern is damaged in any way the sample can be washed in acetone and IPA and the process started again.

Chemically Assisted Ion Beam Etching (CAIBE)

Ion beam milling is a process of etching at typically low pressure of 1mtorr ($\approx 1 \times 10^{-3}mbar$) which involves no chemical reactions with the target. The erosion rate does not vary much for different materials and is therefore ideal for quaternary materials such as InAlGaAs. The most common mechanism uses the Kaufman source, which gives independent control over the ion kinetic energy (target acceleration voltage) and the ion flux (confining magnetic field). A plasma is formed by accelerating electrons through low pressure argon (Ar) gas, where the breakdown voltage is proportional to the pressure and the electrode spacing given by Paschen's law. The ions are then accelerated to a cathode grid which has the target (sample) mounted above it. The mechanism of ablation is known as sputtering. This process lies in between high energy bombardment which gives rise to ion implantation and low energy bombardment ($< 10eV$) where adsorption takes place. Sputtering takes place when ions penetrate several atomic layers, giving up most of their energy in rearranging the physical nature of the material and ejecting atomic clusters in the process. Approximately 95% is atom like, whilst the remainder is diatomic molecules [15]. Upon striking the cathode (target) some of the energy generates secondary electrons which are accelerated away from the target, themselves being absorbed by gas atoms in the chamber, subsequent relaxation releases optical photons that produce a distinctive glow. Due to the ion beam traveling vertically, the erosion takes place on horizontal planes. If the photoresist mask has formed sloped sides (which is common in the development phase) this is transferred to the etch and the side walls are sloped. One way to reduce this is

to introduce a reactive species into the chamber close to the target, and the process is then known as Chemically assisted ion beam etching (CAIBE). Chlorine for example will adsorb to the side walls and the argon ions will then cause decomposition and substrate damage in these areas, giving more control to the formation of straight walls. It must be noted that this does not provide the same level of selective etching as is the case with true chemical etching, however as mentioned earlier this is a robust etch process used for many ternary and quaternary compounds.

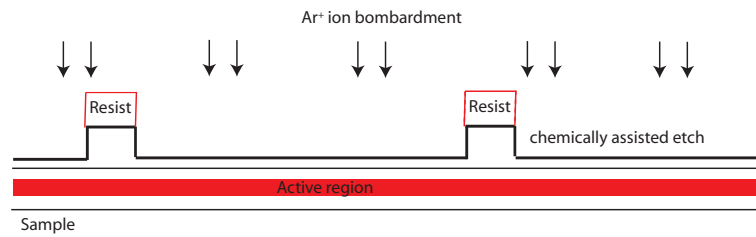


Figure 4.9: Sputtering of Ar ions ejects atomic clusters which etches the sample in the vertical direction.

The sample was etched using a recipe of gun voltage and parameters previously used for etching InGaAs material, due to low percentage of nitrogen in the MQW material. The sample is loaded into a side chamber at atmospheric pressure which is then sealed and pumped down to 10^{-3} mbar. It can then be transferred under this small vacuum to the main chamber which is subsequently pumped down to ultra high vacuum (10^{-9} mbar). Thereafter the Ar and Cl flow rates and the various parameters adjusted accordingly. Once the etching process is complete the procedure is reversed to remove the sample and the remaining photoresist removed with acetone. The etch depth can then be assessed using a mechanical scanning probe (DECKTAK). The sample was then ready to be electrically insulated.

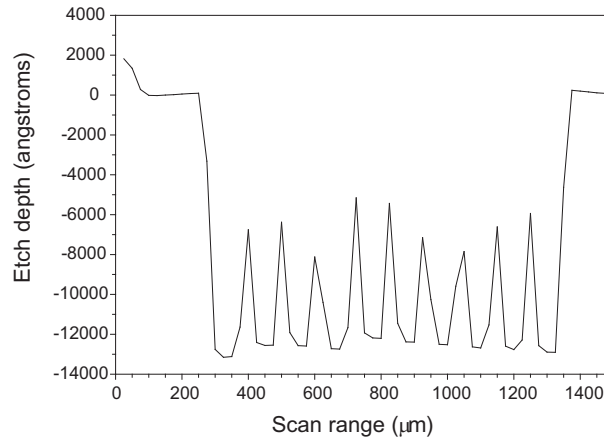


Figure 4.10: Measurement of the actual etch depth after CAIBE processing.

Insulating and patterning

Next the sample is again stuck to a glass slide with PMMA for ease of handling (the wafer samples were typically 1cm x 0.5cm). We now spin the negative photoresist (SU8) at 4000rpm for 60s (dependent on viscosity) to leave a coating approximately $1\mu\text{m}$ thick. SU8 is an epoxy resist (two carbon groups and an oxygen atom joined in a ring), which under UV illumination polymerizes to leave an electrically insulating membrane. After spinning the resist we place the sample on a hot plate for 60s to boil off most of the solvent. The next step is to hard bake at 180°C for 5mins in the oven, which has two effects. Firstly the intense heat causes refilling of the resist into the corners of the etch to make sure there is good electrical isolation. Secondly the small amount of resist on the top of the waveguide ridge forms a crust. This crust is then removed with actone on a cotton bud wiped along the ridges and inspected under a microscope.

We then spin on lift-off resist (LOR), which is a softer positive resist than SR1818. This required 60s at 5000rpm to leave a few hundred nanometers of resist, the sample is placed on the hot plate for 60s to release the solvents and then exposed to UV light. We now carry out an identical photoresist step with SR1818 on top of the LOR, however we used a mask with a larger mark space ratio (typically $40\mu\text{m}$ to $60\mu\text{m}$) displaced so the exposed region overlaps the $5\mu\text{m}$ ridges on the sample. Upon developing, the exposed SR1818 is removed as normal and the LOR underneath is eroded at a greater rate, thus producing an under-etch as seen in figure 4.11.

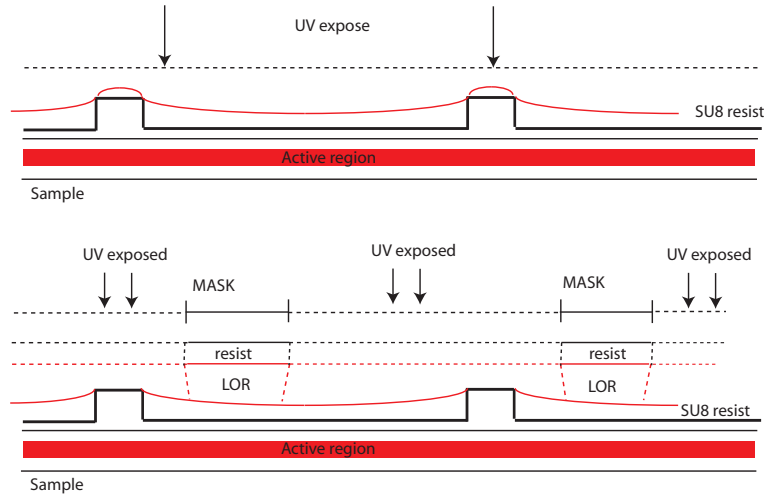


Figure 4.11: Electrical isolation and photolithography stages prior to evaporation of electrical contacts.

4.5.3 Contacts and cleaving

The sample undergoes an acid wash before the contacts can be applied. This involves a 1:1 ratio of HCl to water (typically 30ml of each in a large beaker), where the sample is agitated for 60s and then rinsed in de-ionised water prior to drying with N_2 . This removes any surface contamination which may affect the metallic bonding and electrical conductivity of the ohmic contacts. The sample is initially designed with high concentrations of p and n doping close to the front and back surfaces. This is to make the depletion region between the metal/semiconductor interface as small as possible. This allows carriers to tunnel through the barrier, not being limited by thermionic emission, which minimises the contact resistance.

The contacts are applied by evaporation, which is a less aggressive approach than sputtering (used for silicon technologies). The main reason for this is due to the poor step coverage in evaporation and by using the lift-off resist mentioned above, layers of metal can be deposited which tend to break at abrupt steps in the surface topology. Thereafter acetone is used to remove the lift-off resist, as shown in figure 4.12. The samples are attached to a plate positioned in the top of the chamber whilst solid sources of the component materials are placed in heated crucibles at the bottom of the chamber. Once sealed shut a diffusion pump creates a vacuum of less than $1 \times 10^{-6} \text{ mbar}$ in the chamber. When the sources are heated via electrical coils a vapour forms, whereby component

atoms travel in straight lines to the target and deposit as a film. Multiple crucibles are operated sequentially, using mechanical shutters to prevent contamination of each film being evaporated. In the bottom of the chamber there is a quartz crystal which oscillates at its resonant frequency. As material of a known molecular mass is deposited on it, the frequency changes and the deposition rate can be monitored. The mass evaporation rate of a material is given by the Langmuir expression, where P_e is the equilibrium vapour pressure of the crucible material and M is the molecular mass. Assuming that temperature of the charged vapor is constant, integrating over the constant crucible area gives the rate of mass loss as,

$$R_{ml} = \sqrt{\frac{M}{2\pi k_b}} \frac{P_e}{\sqrt{T}} A. \quad (4.2)$$

The deposition rate is then this mass loss per unit area divided by the film mass density (ρ). Low rates requiring low pressure to keep out contamination are preferable to high rates of deposition where high temperature differentials allow the vapour to condense into larger droplets leading to poor film coverage.

The top and bottom contacts were evaporated in separate steps, requiring the chamber to be pumped down to 1×10^{-6} mbar each time. Manually controlled mechanical shutters start and stop the deposition process. The top contacts consisted of 20nm of Nickel followed by 20nm of Gold. The back contacts require a more robust contact as they are typically bonded to another metal surface when the device is finally in operation. This consisted of 14nm Gold, 14nm Germanium, 14nm Gold, 11nm Nickel and then finally 200nm of Gold again.

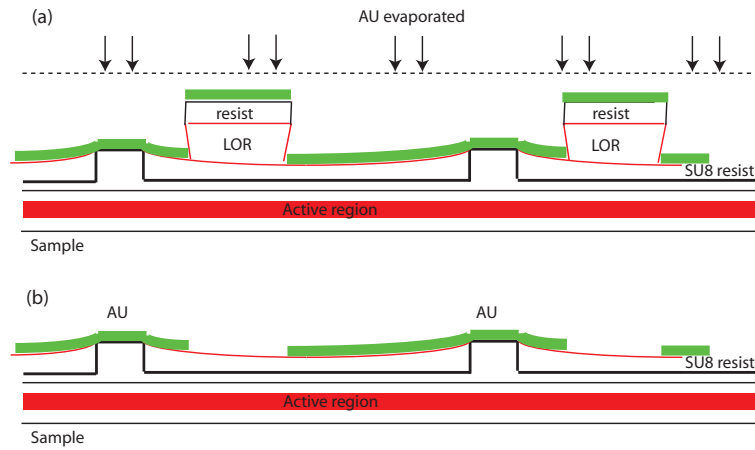


Figure 4.12: Removal of lift-off resist by agitation in acetone, leaving electrically isolated waveguides.

The samples were removed and then agitated in acetone for periods of 30s to systematically remove all of the lift-off resist. Finally they were cleaved using a diamond tipped scribe and broken along the natural crystal plane using a razor blade on a spring loaded platform. Devices were cleaved at lengths from $400\mu\text{m}$ to 1.5mm . Also two batches of devices were tested, one with a 900nm etch depth and the other with an etch depth of 1300nm (almost to the active region). Figure 4.13 shows Scanning Electron Microscope (SEM) images of the finished devices.

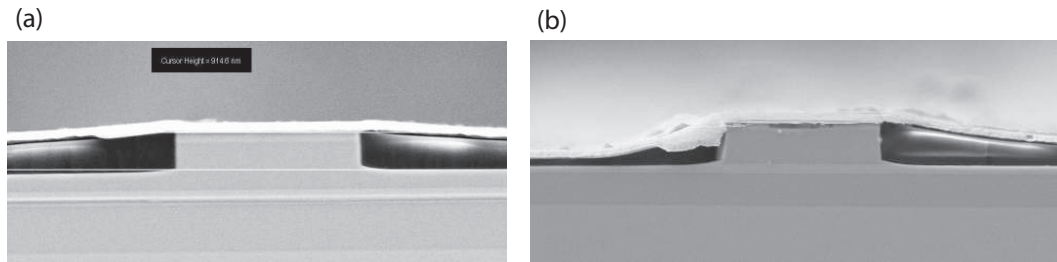


Figure 4.13: (a) Scanning electron microscope images of shallow etched 915nm GaInNAs waveguide and (b) deeply etched 1300nm GaInNAs waveguide.

In order to investigate the output characteristics the devices were mounted a copper/brass mount incorporating a thermoelectric cooler arrangement to maintain the device at room temperature. Using a calibrated power meter instead of the OSA in figure 4.1 the current vs power output was obtained. The major difference was that the current source used to drive the diodes was pulsed with a period of $30\mu\text{s}$, where the duty cycle

(pulse width to period ratio) was varied. To record the current vs voltage characteristics a 10Ω resistor was placed in series with the device and the voltage drop over the resistor was recorded on an oscilloscope. For the deep etched devices a similar setup was used however no series resistor was required due to the nature of the current source and the setup was fully computer controlled via a Labview program from a laptop.

4.5.4 Output (IL) and Voltage (IV) results (950nm etch)

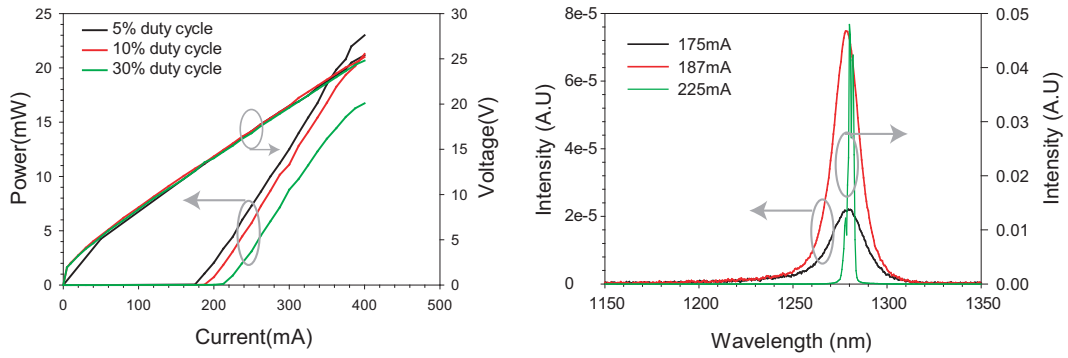


Figure 4.14: (a) Current vs Output power and Current vs Voltage characteristics of shallow etched $500\mu\text{m}$ waveguides. (b) ASE and lasing transition for same device.

Figure 4.14(a) shows the onset of lasing for three of the $500\mu\text{m}$ long shallow etched devices. As the duty cycle was increased from 5% to 30% the threshold current increased, whilst the output power dropped for the same level of current, suggesting internal heating of the device. In fact there is evidence of the onset of thermal rollover in the 30% duty cycle. The current vs voltage curve under ideal conditions should be exponential (as described in chapter 2) and from inspection of the results gives evidence of a superimposed current vs voltage trend in figure 4.14(a) which gives further evidence of an internal resistance path. For this reason all possible steps were taken to aid the thermal conduction between the device and the mount whilst a second set of devices were processed with a deeper etch, to assist current injection to the active region. Figure 4.14(b) shows the ASE and the lasing transition for pulsed current.

4.5.5 Output (IL) results (1300nm etch)

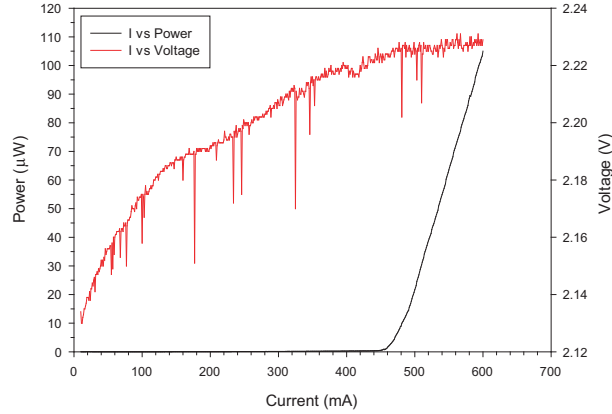


Figure 4.15: Current vs Output power and Current vs Voltage for deeply etched 1.5mm long GaInNAs waveguide.

Figure 4.15 shows lasing characteristics for one of the deep etch devices which was 1.5mm in length. The current density is 1/3 of that used in the 500 μ m shallow etch devices and so we could expect the threshold lasing to require approximately three times the current. The source used a 30 μ s current period with 1.5 μ s pulse (duty cycle = 5%) giving a lasing threshold of 480mA, 2.67 times that of the shorter devices. This shows only a small improvement and the current vs voltage characteristics still indicate the existence of internal resistance. We attribute this the non-radiative traps in the GaInNAs material [16]. However we believe this is acceptable as the devices are to be operated under reverse bias conditions and it has been shown that modulators are more tolerant of defects within materials.

4.6 Summary

In this chapter the electro-optic output characteristics have been established for a range of samples to be used in linear and nonlinear measurements to follow. In addition a description has also been outlined for the fabrication of simple planar waveguides. Most of the specific details regarding the process parameters used in the fabrication of the GaInNAs samples have been omitted. This is to outline the reasoning behind the processing steps that can be applied to almost all of the GaAs based III-V ternary and quaternary compounds. Many of the steps require trial and error and fine tuning to gain particular

results, for example specific thicknesses of resist films and etch depths.

References for Chapter 4

- [1] K Mukai, N Ohtsuka, M Sugawara, and S Yamazaki. Self-Formed $In_{0.5}Ga_{0.5}As$ Quantum Dots on GaAs Substrates Emitting at $1.3\mu m$. *Jap. J. Appl. Phys.*, 33:L1710–L1712, 1994.
- [2] R. P. Mirin, J. P. Ibbetson, K. Nishi, A. C. Gossard, and J. E. Bowers. $1.3\mu m$ photoluminescence from InGaAs quantum dots on GaAs. *App. Phys. Lett.*, 67(25):3795–3797, 1995.
- [3] D. L. Huffaker, G. Park, Z. Zou, O. B. Shchekin, and D. G. Deppe. $1.3\mu m$ room-temperature GaAs-based quantum-dot laser. *Applied Physics Letters*, 73(18):2564–2566, 1998.
- [4] K Nishi, H Saito, S Sugou, and J-S Lee. A narrow photoluminescence linewidth of 21 meV at $1.35\mu m$ from strain-reduced InAs quantum dots covered by $In_{0.2}Ga_{0.8}As$ grown on GaAs substrates. *App. Phys. Lett.*, 74(8):1111–1113, 1999.
- [5] G T Liu, A Stintz, H Li, K J Malloy, and L F Lester. Extremely low room-temperature threshold current density diode lasers using InAs dots in $In_{0.15}Ga_{0.85}As$ quantum well. *Elec. Lett.*, 35:1163–4, 1999.
- [6] Xiaodong Huang, A. Stintz, C.P. Hains, G.T. Liu, J. Cheng, and K.J. Malloy. Efficient high-temperature CW lasing operation of oxide-confined long-wavelength InAs quantum dot lasers. *Electronics Letters*, 36(1):41–42, 2000.
- [7] M V Maximov, L V Asryan, Yu M Shernyakov, A F Tsatsul'nikov I N Kaiander, V V Nikolaev, A R Kovsh, S S Mikhrin, V M Ustinov, A E Zhukov, Zh. I Alferov, N N Ledentsov, and D Bimberg. Gain and threshold characteristics of long wavelength lasers based on InAs/GaAs quantum dots formed by activated alloy phase separation. *IEEE J. Quantum Elec.*, 37(5):676–682, 2001.
- [8] D Bimberg, M Grundmann, and N N Ledentsov. Quantum dot heterostructures. *John Wiley and sons*, 1999.
- [9] M. O. Lipinski, H. Schuler, O. G. Schmidt, K. Eberl, and N. Y. Jin-Phillipp. Strain-induced material intermixing of InAs quantum dots in GaAs. *Applied Physics Letters*, 77(12):1789–1791, 2000.
- [10] E. C. Le Ru, P. Howe, T. S. Jones, and R. Murray. Strain-engineered InAs/GaAs quantum dots for long-wavelength emission. *Phys. Rev. B*, 67(16):165303, Apr 2003.
- [11] M Kondow, K Uomi, A Niwa, T Kitatani, S Watahiki, and Y Yazawa. GaInNAs: A novel material for long wavelength range laser diodes with excellent high-temperature performance.
- [12] Dietrich Meyerhofer. Characteristics of resist films produced by spinning. *Journal of Applied Physics*, 49(7):3993–3997, 1978.
- [13] S A Campbell. *The science and engineering of microelectronic fabrication*. Oxford University Press, 2nd edition, 2001.
- [14] W Hinsberg, C Willson, and K Kanazawa. Use of quartz crystal microbalance rate monitor to examine photoproduct of effects on resist dissolution. *Proc. SPIE Resist Technology*, 6:539, 1985.
- [15] L I Maissel and R Glang. *Handbook of thin film technology*. McGraw-Hill, New York, 1970.
- [16] S Tomic, E P O'Rielly, R Fehse, S J Sweeney, A R Adams, A D Andreev, S A Choulis, T J C Hosea, and H Riechert. Theoretical and experimental analysis of $1.3\mu m$ InGaAsN/GaAs lasers. *IEEE J. Sel. Top. Quan. Elec.*, 9:p1228, 2003.

Chapter 5

Linear characterisation and Electro-refraction

5.1 Introduction

The following chapter presents the linear characterisation of field effects in the semiconductor samples studied in later time-resolved experiments. This is achieved by optical transmission and photocurrent measurements as a function of wavelength and applied field. An outline of the various optical sources used for linear measurements is presented. Additionally the electrically induced refractive index change associated with the quantum confined Stark effect is quantified for one of the samples. This is carried out by solving numerically the Kramers-Kronig dispersion relation and allows for an estimate of the electrically induced phase change in such waveguide structures.

5.2 Investigation of the quantum-confined Stark effect

The discovery of the quantum confined Stark effect (QCSE) [1] in GaAs quantum wells (QW) lead to an enhanced quadratic electro-optic effect, produced by the large band shift when subjected to an electric field perpendicular to the QW. This electro-absorption was immediately exploited directly as an intensity modulator. A later demonstration at the communications wavelength of $1.55 \mu\text{m}$ used an InGaAs/InP waveguide device [2]. As quantitatively described in chapter 2 the Franz-Keldysh effect and more specifically

the QCSE, has further been used successfully in integrated laser-modulators at 2.5Gb/s, 10Gb/s and 40Gb/s [3, 4, 5]. Additionally the change in refractive index associated with the electro-optic absorption change, due to the QCSE was evaluated for potential use in phase modulators [6]. In fact phase modulation was subsequently achieved in an In-GaAs/InP waveguide device at $1.55\mu\text{m}$ [7].

The last decade has seen research into a plethora of optical devices based on quantum dot (QD) heterostructures [8], most notably, lasers and optical amplifiers for high speed communication systems. However less attention has been given to electro-absorption modulators [9] in this material system, with the potential for optical switching at $1.3\mu\text{m}$.

In order to experimentally determine the electrically induced change in absorption associated with the quantum confined Stark effect (termed because we are also dealing with 0D and 2D confinement), we used the photocurrent generated via optical injection in each of the waveguide samples. This is a simple and direct method based on absorption over all transitions where there is a significant dipole moment. As such this allows the reduction in absorption associated with the reduced overlap for increasing reverse fields to also be measured. We have carried out such measurements not only in quantum dot structures, but also GaInNAs multiple quantum wells. Another reason for measuring the Stark shift is to be able to choose the optimum wavelength and polarisation for the pump and probe measurements in chapter 6.

5.3 Photocurrent measurements

In order to obtain absorption information over a large wavelength range we used a 250W halogen white light source combined with a $1/2\text{m}$ monochromator. This was then passed through a mechanical chopper (MC) to modulate the light before passing through a polarising beam splitting (PBS) cube to give TE or TM polarised light. The beam was then coupled into the device mounted on an xyz micro manipulation (waveguide) stage via a 30x aspheric lens. This setup was used for all three samples. Prior to placing samples in the setup, the lamp spectrum was recorded and was used for normalisation of the photocurrent signal measured later. A short wavelength filter is also used to remove any second or higher diffraction orders in the monochromator grating, which give undesirable

photocurrent signals (noise). The photocurrent was recorded via phase-sensitive detection by measuring the induced voltage across a resistor of known value placed in series with the diode under reverse bias. This allows measurement of the photocurrent at applied reverse bias. This setup is shown in fig. 5.1.

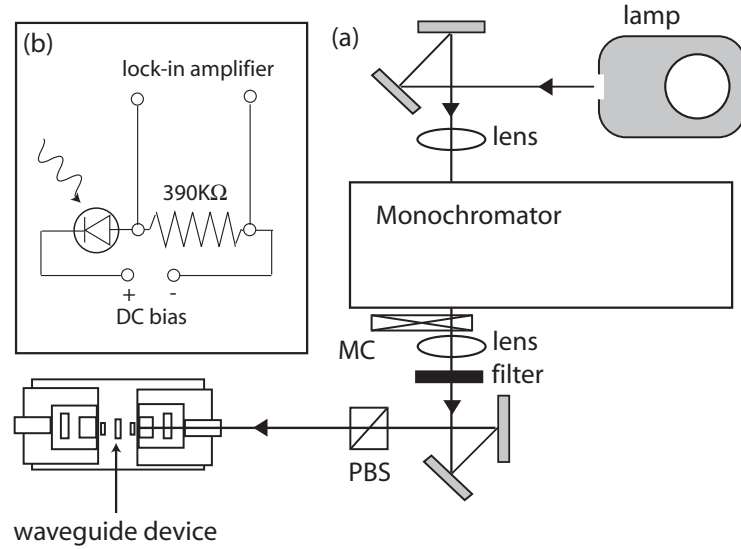


Figure 5.1: (a) Experimental setup for photocurrent measurements using a halogen lamp. (b) Circuit diagram indicating how the photocurrent is recorded via lock-in detection.

The free carriers generated from the absorption of photons across the diode band gap generates a current in the external circuit. Initially under reverse bias the diode and resistor form a potential divider, the resistance of the diode is $\sim 1\text{-}2\text{M}\Omega$ and almost all of the DC bias voltage is dropped across the diode. This means that if a suitably large (but small relative to the diode) resistor is chosen, the photocurrent will generate a measurable voltage across the resistor that can be recorded by the lock-in amplifier at the frequency of the mechanical chopper ($\sim 130\text{Hz}$). If the resistor is too large the field across the diode will drop and also any thermal noise in the photocurrent will also be amplified.

5.3.1 Results for single QDs: Sample 101

In the case of the isolated (single layered) QDs without anti-reflection coatings on the facets, the absorption was found to be very small and very little field dependency of the photocurrent was measured. The experimental setup was as described above however, the photocurrent at no applied field was measured directly across the p-i-n device by

connecting the lock-in amplifier to the n-side and p-side via electrical probes. The results are shown in figure 5.2.

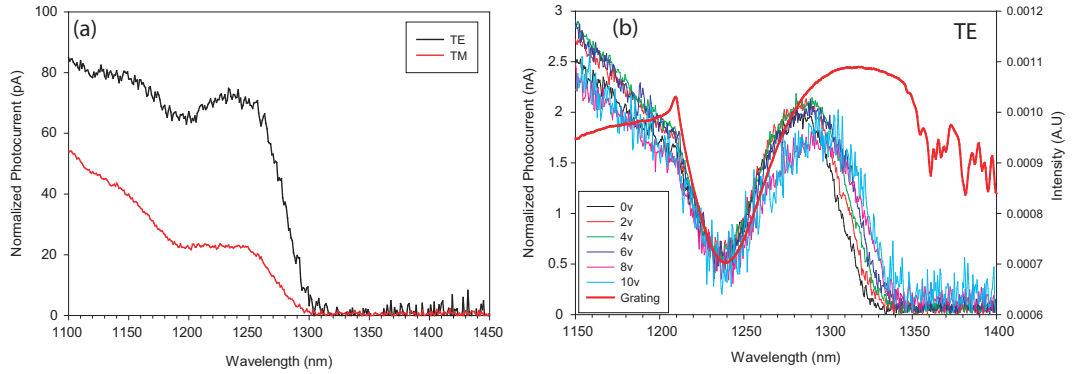


Figure 5.2: (a) Normalized photocurrent measurements for TE and TM polarised light in a waveguide comprising single DWELL QDs, without anti-reflection coating and (b), with anti-reflection coatings. Also shown is the grating response to TE polarised light as measured.

In the above figure there is also field dependent photocurrent measurements for a device processed with the same material but with anti-reflection coatings applied to the facets. The measurements in this case were for reverse bias voltages up to 10V (corresponding to a field of 270KV/cm). This is only given as a comparison to show the increase in generated photocurrent when a higher intensity of light is present inside the cavity of the device. For the case of TM light the absorption was too low to measure a field dependency but from figure 5.2(a) it is clear that the QD transitions are strongly TE polarised (field parallel to layers), indicating they have predominantly heavy-hole characteristics [10, 11]. For TE polarised light there is a clear shift in the absorption edge of approximately 11meV (15nm at 1280nm). However, the characteristic reduction in photocurrent that is normally seen is not clear due to the photocurrent noise in the measurement. This initial result shows very little broadening in the absorption feature of the QDs, and could be due to the higher confinement in the direction of field (dot height of 5nm). These results are in quantitative and qualitative agreement with previous work on similar dots [12], showing a Stark shift of ~ 17 meV with no obvious broadening. The measurements from literature were based on a fitting model for the transition energy $E = E_0 + pF + \beta F^2$. The first term is the energy at $F=0$ (zero field), the second term is due to the permanent dipole due to the finite separation of the electron and hole, and the final term is the induced polarization of the

dots in the presence of an applied field (the quantum confined Stark effect, as outlined in chapter 2). It was also found in this work as well as by Raymond et al. for AlInAs/AlGaAs QDs [13], that the Stark shift is asymmetric about the $F=0$ point. As a slight forward bias is applied (field from apex to base of the dot) there is an initial blue shift, which we ourselves have not investigated. This has been attributed to the confinement of the electron wavefunction as it is driven to the apex. This suggests that the dipole is reversed, in contradiction with previous theoretical models [14, 15, 16], which indicate that the hole wavefunctions are confined to the base of the dot, whilst the electron wavefunction exists above. One possibility for this reversal could be due to indium enrichment at the apex due to strain fields during the growth of quantum dots. In fact these effects have been carefully exploited to grow larger dots in adjacent layers for the purpose of long wavelength emission. More recent measurements with preferentially charged excitons [17](ie 2 holes + 1 electron, 3 holes + 1 electron) have given more evidence to suggest that the dipoles in QDs are oriented from base to apex. This indicates that such field dependent photocurrent spectroscopy measurements provide substantial assistance to theoretical models used to describe quantum confined structures.

The QCSE in QDs is generally expected to be reduced compared with QWs due to the smaller dimension in the direction of the electric field. This is due to the smaller potential drop across the dot and the greater difficulty of perturbing more strongly confined states. To increase the interaction length one can grow larger dots, or vertically coupled dots [18] as demonstrated by Ser et al. [19]. These later measurements were carried out by optical propagation with a halogen lamp in the growth direction, where the extent of the active region is only a few microns.

5.3.2 Results for Bilayer QDs: Sample 102

Field dependent room temperature photocurrent (PC) measurements were recorded using a $390\text{K}\Omega$ resistor in series with the p-i-n device under reverse bias voltages up to 10V (corresponding to an internal field of $200\text{KV}/\text{cm}$). Light from the halogen lamp, filtered by the monochromator and polariser was then coupled into the waveguide via a 40x aspheric lens. The PC was measured using lock-in detection and the results are shown in figure 5.3

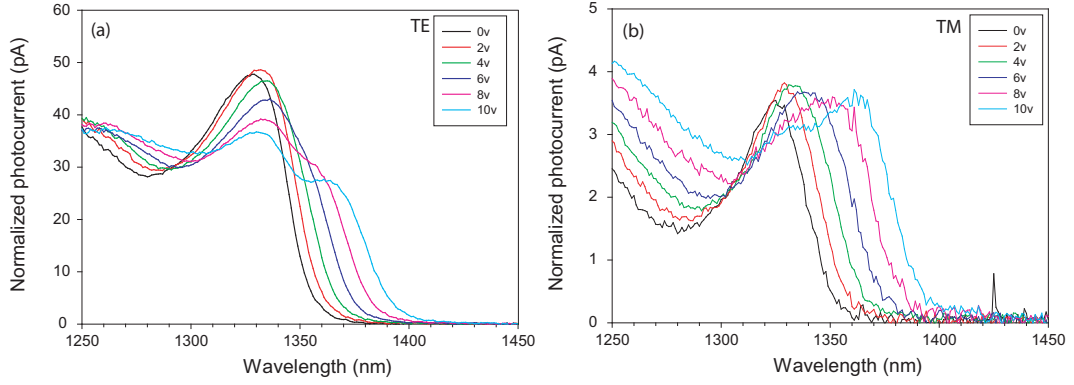


Figure 5.3: (a) Normalized photocurrent measurements for polarised light in a waveguide comprising Bilayer QDs without anti-reflection coating for TE light, (b) TM light.

The traces exhibit a broadening and a shift of the absorption peak, characteristic of the reduced binding energy of the electron-hole pair, separated by the electric field. The measured shift of up to 40nm at 1340nm is large compared with isolated QDs and is tentatively attributed to the reduced lateral confinement in the growth and field direction for such large dot sizes (~ 9 nm height). In addition there is a doublet in the absorption feature, which begins to appear at around -6V. We attribute this to the separation of the light and heavy hole exciton, which is normally unresolvable in such highly quantum confined systems. The magnitude of the longer wavelength absorption feature is greater for the case of TM polarised light and this suggests a larger quantum confined Stark shift for the light hole exciton, relative the heavy hole exciton.

5.3.3 Results for GaInNAs MQWs: Sample 103

Field dependent room temperature PC measurements were recorded again using a $390\text{K}\Omega$ resistor in series with the p-i-n device under reverse bias voltages up to 7 V (corresponding to an internal field of 190 KV/cm). The reduction in the intrinsic region of the MQW devices limits the voltage that can be applied before the zener breakdown point is reached. The PC was again measured using lock-in detection and the results are shown in figure 5.4.

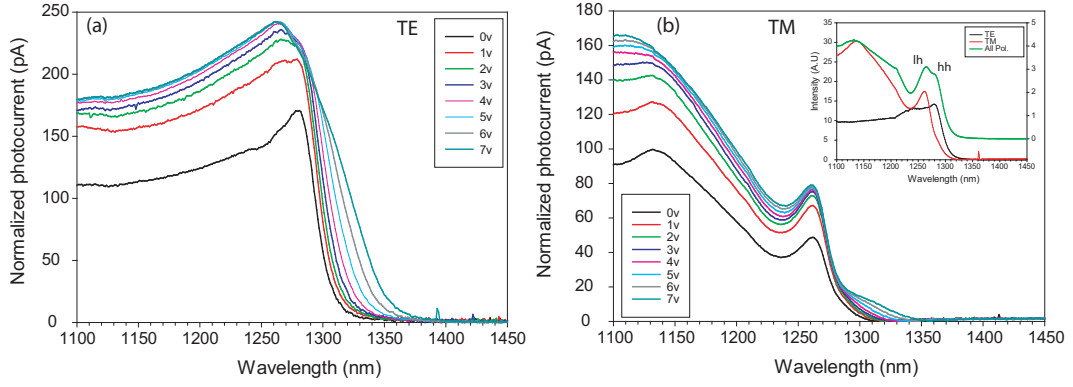


Figure 5.4: (a) Normalized photocurrent measurements for polarised light in a waveguide comprising GaInNAs MQWs without anti-reflection coating for TE light, (b) for TM light. The inset shows the presence of light hole and heavy hole excitons.

There is a clear shift of the absorption edge of 30nm at 1300nm for increasing fields, and although the light and heavy hole excitons are not very discernable, the excitonic feature is still clear at high reverse fields. In contrast to Stark shifts measured with light perpendicular to the GaInNAs QWs [20], we do not see the shift correspond to a drop in absorption due to the wave function overlap reduction. However, these shifts compare favourably with other measurements of the QCSE in GaInNAs MQWs at 1300nm, where thermal annealing was also shown to increase the absorption by a factor of ~ 2 [21]. The most noticeable effect here is the increasing photocurrent over all wavelengths as the reverse bias is increased. This is attributed to the poor collection efficiency of photogenerated carriers, normally seen at low fields. In the case of GaInNAs, the presence of an impurity level (nitrogen doping) leads to a great amount of non-radiative recombination [22]. However, for high fields this recombination should be impeded. From inspection of the energy band structure (chapter 4). There is a large band offset between the GaAs separate confinement hetrostructure (SCH) and the AlGaAs p and n doped regions. In this particular structure it is $\sim 500\text{meV}$, which is a more likely reason for reduced collection of free carriers. The inset of figure 5.4(b) also shows the presence of light and heavy hole exciton transitions. The heavy hole transition incurs the greatest shift in energy as it is most highly confined.

5.4 Optical transmission measurements (I): Tuneable laser

The use of photocurrent measurements is extremely useful in free-space configuration, when the light is perpendicular to the plane of the QWs. It is then simple to extract the field-dependent absorption changes, but requires the assumption of 100% quantum efficiency [20]. However, this approximation is insufficient for waveguide devices as we have scattering and radiation losses to consider. One way to assess the modal absorption is to carry out transmission measurements through the waveguide sample. This presents the problem of finding a source with suitable power to leave an optically detectable signal after propagation through a few hundred microns of semiconductor material. We chose the isolated QD device (sample 101) for this investigation, due to the low absorption ascertained from the previous photocurrent measurements.

The initial source used for transmission measurements on the device was a tuneable InGaAsP distributed feedback (DFB) laser diode, coupled with a tuneable grating. Due to the gain bandwidth of the solid-state diode, the output was clamped to give $290\mu\text{W}$ across a full wavelength range of 1250-1360nm. The spectrum was recorded with an optical spectrum analyser (OSA) and found to be stable in time, which circumvented the need for real time normalisation of the input power to the device.

5.4.1 Experimental setup

The DFB laser and grating give a coherent tuneable output which is passed through a $\lambda/2$ waveplate and a polarising beam splitter to obtain TE or TM polarised light. The beam is then coupled via a 30x aspheric lens into the device which is stuck to a copper mount on top of a thermo-electric cooler (TEC) to maintain the device at room temperature. The beam is modulated via a mechanical chopper ($\sim 130\text{Hz}$) and both the input power (P_{in}) and output power (P_{out}) of the device are recorded by phase-sensitive detection via a germanium detector. For each reverse bias applied a measure of P_{out} is taken over the full wavelength scan. The transmission can then be obtained from comparison with the initial scan of P_{in} .

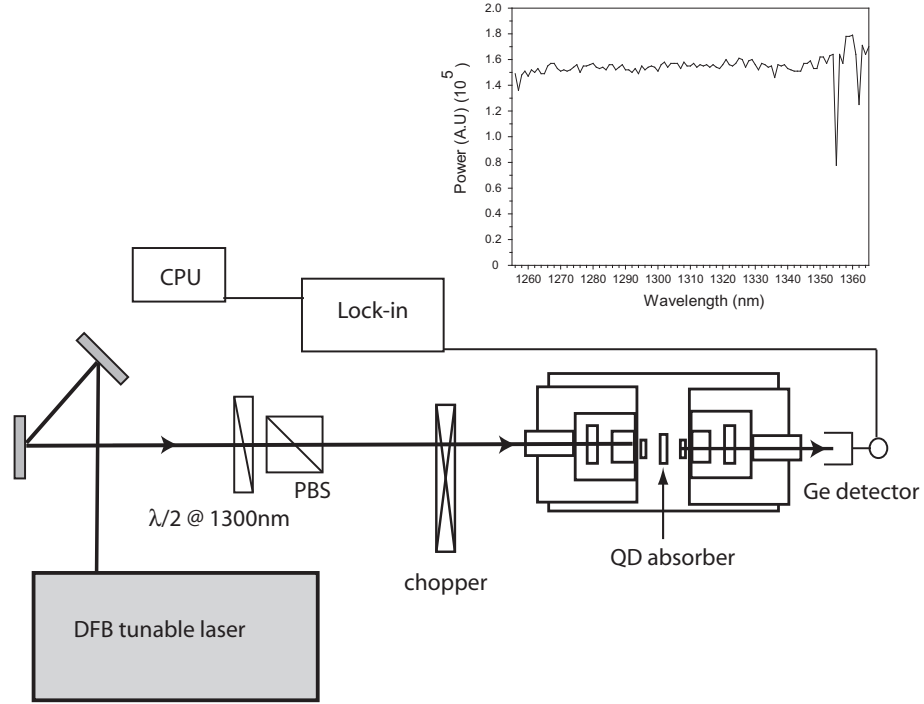


Figure 5.5: Experimental setup for transmission measurements on waveguide structures using the tuneable DFB laser diode source

5.4.2 Absorption results for single QDs: Sample 101

The transmission loss can be split into an intrinsic part (α_i) which includes waveguide losses from radiation and scattering and absorption in the active region (α_m). The latter is weighted by the confinement factor (Γ) and depends on the applied field. The transmission loss is defined as

$$T(V) = \frac{P_{out}}{P_{in}} = C e^{-\alpha_i L} e^{-\Gamma \alpha_m(V) L}, \quad (5.1)$$

where C accounts for the coupling ratio into and out of the device. Measurements were carried out for voltages up to -10V (corresponding to a field of 270KV/cm). From equation 5.1, the overall transmission loss can be obtained as $\ln(1/T(V))$ and is shown in fig. 5.6.

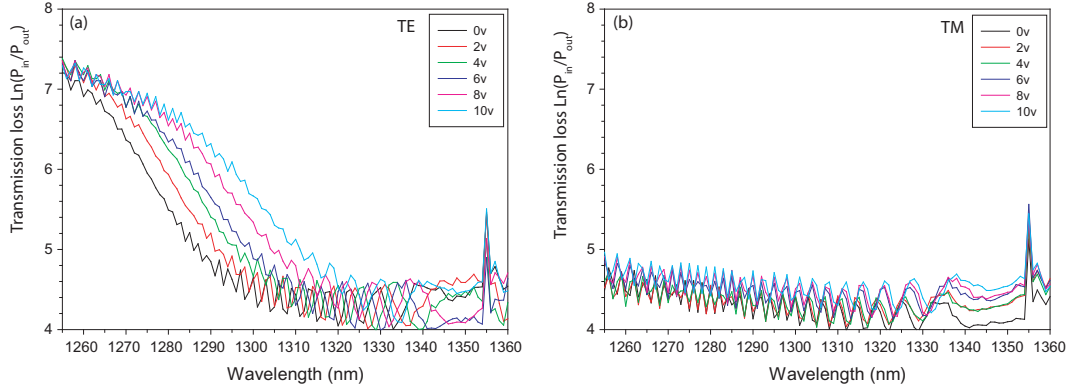


Figure 5.6: (a) QCSE measured for TE and (b) TM polarised light

The results indicate a Stark shift of $\sim 20\text{nm}$ which is relatively small compared with typical values in QWs. However as previously mentioned, the dimension are much reduced in QDs. The fringes superimposed in fig. 5.6 are due to fabry perot effects in the laser. We see virtually no absorption for the case of TM polarised light for the wavelength range used, indicating the lack of a heavy hole transition which we would expect when considering the selection rules (chapter 2). Although we have quantitatively measured the field dependent absorption, it is limited to a narrow wavelength range and does not give a clear picture of absorption over the entire band edge. This highlights the need for a broadband source with suitable power to measure optical transmission through such devices.

5.5 Optical transmission measurements (II): Tuneable supercontinuum

One solution to this problem is to use a photonic crystal fibre (PCF) continuum generator (see chapter 3), which has suitable power to allow optical transmission measurements through the 1.1mm InAs-InGaAs planar waveguide modulator (sample 101).

5.5.1 Transmission setup with real-time normalisation

The supercontinuum was generated in a 12 cm length of single mode PCF (Femtowhite 800^{TM}) with a zero-dispersion wavelength of 750 nm, pumped by a 20 fs Ti:Sapphire laser at 80 MHz. The large non-linear dispersion in the germanium-doped silica fiber is attributed to a combination of self-phase modulation (SPM), cross-phase modulation

(XPM), third harmonic generation (THG) and four-wave mixing (FWM) [23]. These non-linear mechanisms as well as the solitons generated, are very sensitive to fluctuations in the pump power and therefore real-time normalization of the spectrally filtered continuum was implemented. This was achieved using two identical germanium detectors with phase sensitive detection (see figure 5.7). As the monochromator wavelength is scanned in the 1100-1400 nm range, detector 1 (D1) monitors a fraction of the input power (reflected from a glass slide), while simultaneously detector 2 (D2) measures the output power (P_{out}) from the device. An initial calibration scan with D2 placed before the sample is used to calculate the input powers (P_{in}) from the D1 signal in each of the subsequent transmission measurements. In all measurements reported here we used TE polarized light (optical electric field parallel to the well layers and along the larger dimension of the dots). This was due to the large shift demonstrated for this polarisation in previous measurements with the tuneable laser source.

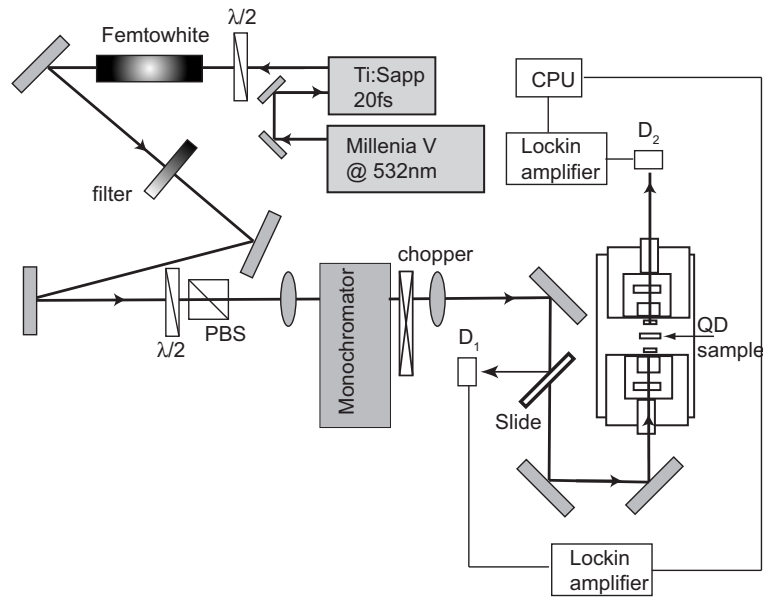


Figure 5.7: Supercontinuum generator (FEMTOWHITE 800TM) combined with monochromator to give tuneable broadband source used for transmission measurements in an InAs QD sample at 1.3 μ m.

5.5.2 Absorption results for single QDs: sample 101

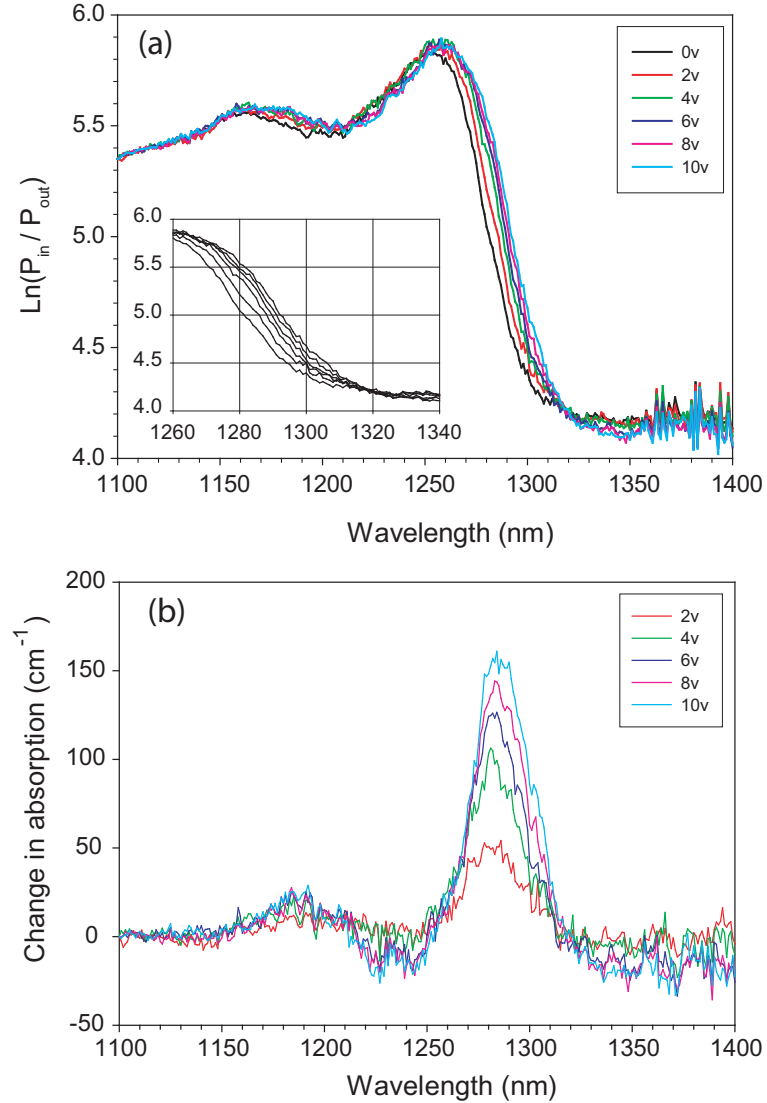


Figure 5.8: (a) Field dependent loss in an InAs QD modulator showing the quantum confined Stark effect at reverse bias (0-10V), (inset) highlighted region of band-edge. (b) Change in absorption due to applied reverse bias for the ground state and first excited state.

Optical transmission experiments through the QD device were carried out for a range of reverse applied biases (0-10V), corresponding to electric fields of 0-270KV/cm. Figure 5.8(a) shows the measured transmission loss, $\text{Ln}(P_{in}/P_{out})$. From the inset of this figure we see a Stark shift of 15 nm (11 meV) at the ground state of 1280nm (969meV). In comparison, quantum confined Stark shifts have been demonstrated in QW material at $1.3\mu\text{m}$ of $\sim 25\text{meV}$ at a field of 150KV/cm [24]. Field induced broadening of the exciton

transition is smaller in QWs than in bulk due to the confinement in the direction of the field. In figure 5.8(a), however, we believe the inhomogeneous quantum dot size distribution is masking any field dependent broadening associated with the separation of an electron-hole bound pair. In this figure we also observe a feature associated with the first excited state at 1170nm (1.056eV) (indicated by independent amplified spontaneous emission measurements, see chapter 4). However the corresponding field dependent absorption change appears to be small and therefore not clearly resolved. If this was a shift due to the QCSE of the excited state it would in fact blue shift.

There are several absorption and loss processes existing within a waveguide modulator as mentioned previously. We assume that free-carrier absorption (FCA) and inter-valance band absorption (IVBA) are small compared to both radiation loss through the evanescent mode (α_{rad}) and scattering loss (α_{scat}) in the waveguide [25]. Considering Beer's Law we can describe the field dependent transmission as,

$$T(V) = \frac{P_{out}}{P_{in}} = C e^{-\alpha_i L} e^{-\Gamma(\alpha_{QD,0} + \Delta\alpha_{QD,V})L}. \quad (5.2)$$

Again C accounts for the coupling losses at the input and output facets, α_i accounts for the waveguide losses ($\alpha_i = \alpha_{rad} + \alpha_{scat}$). In equation 5.2 the material absorption has been split into absorption at zero volts plus a field dependent part ($\alpha_m = \alpha_{QD,0} + \Delta\alpha_{QD}$). Finally Γ is the confinement factor and L is the device length. One advantage of having measured T(V) is that $\Delta\alpha(V)$ can be measured and the change in refractive index Δn can be estimated from it. From inspection of equation 5.2 the field induced change in absorption in the QD material is extracted by the division T(V)/T(0),

$$T(V)/T(0) = e^{-\Gamma\Delta\alpha_{QD,V}L}. \quad (5.3)$$

In these calculations, an estimate of the confinement factor was used, $\Gamma = 0.03$. Note, however that assumptions regarding intrinsic and coupling losses are not required, as they cancel out.

5.5.3 Refractive index results for isolated QDs

Along with absorption change ($\Delta\alpha$) comes a change in the refractive index (Δn), dictated by causality, which can be exploited in optical phase modulation. This is mathematically described by the Kramers-Kronig relations [26] as explained in chapter 1. In addition, The rule dictating that all changes in absorption must sum to zero has previously been experimentally shown to lay within 0.3% for AlGaAs MWQs up to fields of 200KV/cm, when the spectral range covers the n=2 subband edge [27].

$$\Delta n(\omega) = \frac{c}{\pi} P \int_0^\infty \frac{\Delta\alpha(\omega')}{\omega'^2 - \omega^2} d\omega, \quad (5.4)$$

where P denotes the principal value of the integral. For every frequency ω , the integral is calculated over the whole range of ω' . As shown in figure 5.8(b), $\Delta\alpha$ is non-zero over a limited spectral range allowing us to evaluate the refractive index change numerically [28](see Appendix). This justifies the need for such a broadband source.

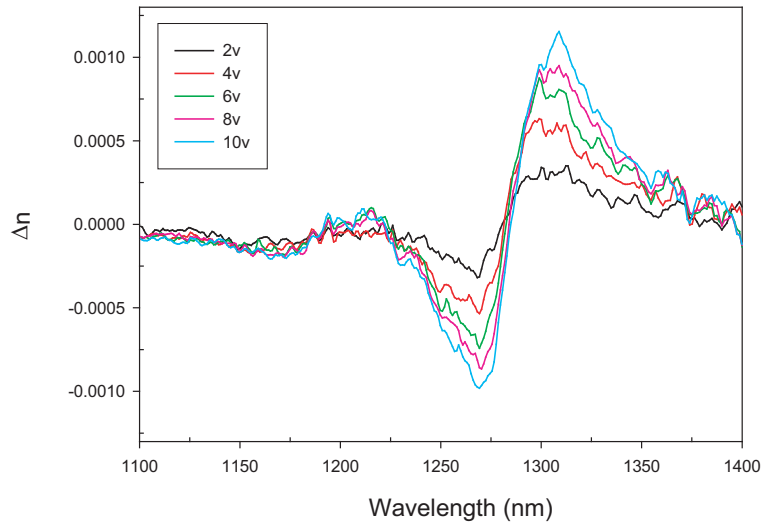


Figure 5.9: Field dependent refractive index change calculated via the Kramers-Kronig relation using the data in figure 5.8(b).

Figure 5.9 shows the spectral dependence of the electro-refraction, calculated via Kramers-Kronig relations (see Appendix), applied to the measured absorption changes in figure 5.8(b). A maximum change of 1.5×10^{-3} occurs below band-gap, at the low absorption point where such devices are operated. We estimate the corresponding phase change through the device to be 0.2rads (0.06π) at 1300nm ($\Delta\phi = \Gamma(2\pi/\lambda)\delta nL$), see

Coldren and Corzine [29]. Also, the maximum absorption change of 150 cm^{-1} was measured at 1280nm (-10V), where insertion loss is approximately 21dB, and corresponds to a contrast ratio of 2.1 dB [9],

$$\begin{aligned} [on/off]dB &= -10\log_{10}\left(\frac{P_{in}}{P_{out}}\right) \\ &= 4.34\Gamma\Delta\alpha L. \end{aligned} \tag{5.5}$$

These values are small compared with typical QW waveguides ($\sim 200\mu\text{m}$ long). However, it must be stressed that the device under study comprises only 5 layers of active material, and is relatively short (1.1mm) for a QD device. By considering longer devices, using a greater number of dot layers, or by enhancing the QCSE via optimized design, we believe optical modulators based on such material are possible. In addition the rapid carrier escape in quantum dots (see for example [30]) should reduce the electro-absorption saturation and the power dependent degradation of the frequency response in such devices.

5.6 Summary

We have qualitatively compared the QCSE in isolated QDs, bilayer QDs and GaInNAs MQW samples grown on GaAs substrates at the technologically important telecommunications wavelength of $1.3\mu\text{m}$. The motivation was to demonstrate the potential for such materials to be used in electro-absorption modulators exhibiting good thermal characteristics (low T_0). Additionally this information is necessary when carrying out pump probe measurements.

We have also characterised the field dependent absorption and associated electro-refraction in a waveguide modulator, comprising 5 layers of isolated InAs quantum dots. This was achieved through optical transmission measurements using a supercontinuum generator as the broadband source, and real-time normalisation with phase-sensitive detection. This versatile technique allowed us to extract the field dependent absorption changes and associated electro-refraction, key to characterising QCSE-based modulators. The experimental technique demonstrates an easy way to characterise a series of such

waveguide modulators robustly. The results show a quantum confined Stark shift of the ground state with no significant broadening of the transition. At an applied field of 270KV/cm (-10V) the dot ground state red-shifts by 11meV (15nm at 1280nm), giving a maximum refractive index change of 1.5×10^{-3} below the band gap. This shows the potential of quantum dots for GaAs based intensity and phase modulators at $1.3\mu\text{m}$ as an alternative to an InP based platform.

References for Chapter 5

- [1] D. A. B. Miller, D. S. Chemla, T. C. Damen, A. C. Gossard, W. Wiegmann, T. H. Wood, and C. A. Burrus. Electric field dependence of optical absorption near the band gap of quantum-well structures. *Phys. Rev. B*, 32(2):1043–1060, Jul 1985.
- [2] U Koren, T L Koch, H Presting, and B I Miller. InGaAs/InP multiple quantum well waveguide phase modulator. *Appl. Phys. Lett.*, 50(7):368–370, 1986.
- [3] M Aoki, N Kikuchi, K Sekine, S Sasaki, M Suzuki, T Taniwatari, Y Okuno, A Takai, and T Kawano. Low drive voltage and extremely low chirp integrated electroabsorption modulator/DFB laser for 2.5 Gbit/s 200 km normal fibre transmission. *Electronic Letters*, 29:pp. 1983–1984, 1993.
- [4] K Wakita, O Mitomi, I Kotaka, S Nojima, and Y Kawamura. High-speed electrooptic phase modulators using InGaAs/InAlAs multiple quantum well waveguides. *IEEE Ph Tech. Lett.*, 1(12):pp441–442, 1989.
- [5] M Aoki, N Kikuchi, K Sekine, S Sasaki, M Suzuki, T Taniwatari, Y Okuno, A Takai, and T Kawano. Low drive voltage and extremely low chirp integrated electroabsorption modulator/DFB laser for 2.5 Gbit/s 200 km normal fibre transmission. *Electronic Letters*, 29:pp. 1983–1984, 1993.
- [6] Joseph S. Weiner, David A. B. Miller, and Daniel S. Chemla. Quadratic electro-optic effect due to the quantum-confined stark effect in quantum wells. *Applied Physics Letters*, 50(13):842–844, 1987.
- [7] J E Zucker, T L Hendrickson, and C A Burrus. Electro-optic phase modulation in GaAs/AlGaAs quantum well waveguides. *Appl. Phys. Lett.*, 52(12):945–947, 1988.
- [8] D Bimberg, M Grundmann, and N N Ledentsov. Quantum dot heterostructures. *John Wiley and sons*, 1999.
- [9] K Wakita. *Semiconductor Optical Modulators*. Kluwer Academic Publishers, 1998.
- [10] K L Hall, E R Thoen, and E P Ippen. *Semiconductors and Semimetals*, volume 59, chapter 2 Nonlinearities in Active Media. Academic Press, 1999.
- [11] G Bastard. *Wave mechanics applied to semiconductor heterostructures*. John Wiley and sons, 1992.
- [12] P. W. Fry, I. E. Itskevich, D. J. Mowbray, M. S. Skolnick, J. J. Finley, J. A. Barker, E. P. O’Reilly, L. R. Wilson, I. A. Larkin, P. A. Maksym, M. Hopkinson, M. Al-Khafaji, J. P. R. David, A. G. Cullis, G. Hill, and J. C. Clark. Inverted electron-hole alignment in inas-gaas self-assembled quantum dots. *Phys. Rev. Lett.*, 84(4):733–736, Jan 2000.
- [13] S. Raymond, J. P. Reynolds, J. L. Merz, S. Fafard, Y. Feng, and S. Charbonneau. Asymmetric Stark shift in $Al_xIn_{1-x}As/Al_yGa_{1-y}As$ self-assembled dots. *Phys. Rev. B*, 58(20):R13415–R13418, Nov 1998.
- [14] M. Grundmann, O. Stier, and D. Bimberg. InAs/GaAs pyramidal quantum dots: Strain distribution, optical phonons, and electronic structure. *Phys. Rev. B*, 52(16):11969–11981, Oct 1995.
- [15] M. A. Cusack, P. R. Briddon, and M. Jaros. Electronic structure of inas/gaas self-assembled quantum dots. *Phys. Rev. B*, 54(4):R2300–R2303, Jul 1996.
- [16] Craig Pryor. Eight-band calculations of strained InAs/GaAs quantum dots compared with one-, four-, and six-band approximations. *Phys. Rev. B*, 57(12):7190–7195, Mar 1998.
- [17] J. J. Finley, M. Sabathil, P. Vogl, G. Abstreiter, R. Oulton, A. I. Tartakovskii, D. J. Mowbray, M. S. Skolnick, S. L. Liew, A. G. Cullis, and M. Hopkinson. Quantum-confined stark shifts of charged exciton complexes in quantum dots. *Physical Review B (Condensed Matter and Materials Physics)*, 70(20):201308, 2004.

- [18] N N Ledentsov, V A Shchukin, M Grundmann, N Kirstaedter, J Bohrer, O Schmidt, D Bimberg, V M Ustinov, A Yu Egorov, A E Zhuov, P S Kop'ev, S V Zaitsev, N Yu Gordeev, Zh I Alferov, A I Borovkov, A O Kosogov, S S Ruvimov, P Werner, U Gosele, and J Heydenreich. Direct formation of vertically coupled quantum dots in Stranski-Krastanow growth. *Phys. Rev.B*, 54(12):8743, 1996.
- [19] J-H Ser, Y-H Lee, J-W Kim, and J-E Oh. Direct observation of strong quantum-confined stark effect in vertically-stacked quantum dots at room temperature. *Jpn. J. Appl. Phys.*, 39:L518–L520, 2000.
- [20] Y.S. Jalili, P.N. Stavrinou, J.S. Roberts, and G. Parry. Electro-absorption and electro-refraction in InGaAsN quantum well structures. *Electronics Letters*, 38(7):343–344, 2002.
- [21] V. Lordi, H. B. Yuen, S. R. Bank, and J. S. Harris. Quantum confined Stark effect of GaInNAs(Sb) quantum wells at 1300-1600nm. *Applied Physics Letters*, 85(6):902–904, 2004.
- [22] S Tomic, E P O'Rielly, R Fehse, S J Sweeney, A R Adams, A D Andreev, S A Choulis, T J C Hosea, and H Riechert. Theoretical and experimental analysis of 1.3 μ m InGaAsN/GaAs lasers. *IEEE J. Sel. Top. Quan. Elec.*, 9:p1228, 2003.
- [23] G P Agrawal. Nonlinear fiber optics 3rd edition. *Academic press*, 2001.
- [24] J. E. Zucker, I. Bar-Joseph, B. I. Miller, U. Koren, and D. S. Chemla. Quaternary quantum wells for electro-optic intensity and phase modulation at 1.3 and 1.55 μ m. *Applied Physics Letters*, 54(1):10–12, 1989.
- [25] J Shim, B Liu, J Piprek, and J E Bowers. An improved approach of optical loss measurement using photocurrent and optical transmission in an electroabsorption modulator. *IEEE Ph. Tech. Lett.*, 16(6):pp10–12, 2004.
- [26] D C Hutchings, M Sheik-Bahae, D J Hagan, and E W Van Stryland. Kramers-Krönig relations in nonlinear optics. *Opt. Quant. Electron.*, 24:1–30, 1992.
- [27] M. Whitehead, G. Parry, K. Woodbridge, P. J. Dobson, and G. Duggan. Experimental confirmation of a sum rule for room-temperature electroabsorption in gaas-algaas multiple quantum well structures. *Applied Physics Letters*, 52(5):345–347, 1988.
- [28] V Lucarini, J J Saarinen, and K-E Peiponen E M Vartiainen. Kramers-Kronig relations in optical material research. *New York Springer*, 2005.
- [29] L A Coldren and S W Corzine. *Diode Lasers and Photonic Integrated Circuits*. Wiley, New York, 1995.
- [30] D. B. Malins, A. Gomez-Iglesias, S. J. White, W. Sibbett, A. Miller, and E. U. Rafailov. Ultrafast electroabsorption dynamics in an InAs quantum dot saturable absorber at 1.3 μ m. *App. Phys. Lett.*, 89(17):171111, 2006.

Chapter 6

Nonlinear Electro-absorption dynamics

6.1 Introduction

In chapter 5 we measured the field dependent shift of the bandedge in quantum dots and quantum wells. This effect (QCSE), has been widely used to implement optical modulators in communication systems. In the present chapter we will deal with the temporal dynamics of the absorption in these devices, with a view to their applications in switching and mode-locking. This chapter will focus on the experimental pump-probe technique used to measure the time dependent absorption dynamics. The first measurements investigate the field and temperature dependence of the absorption recovery in InAs dot-in-well (DWELL) quantum dots. Following this, the field-dependence is investigated for InAs/GaAs bilayer quantum dots, and finally for GaInNAs multiple quantum wells. All three waveguide devices are described in chapter 4. The use of this technique gives insight into the carrier escape dynamics which ultimately dictate the performance of absorption modulators.

6.2 Pump-probe technique

When investigating semiconductor nonlinearities, it is essential to resolve the dynamic changes of the carrier densities. This can be achieved by measuring their effective lifetime. The carrier densities can be modified via electrical or optical injection, escape or

recombination and this has the effect of changing the photon energy (wavelength) at which absorption and gain occur [1]. Time domain pump-probe (otherwise known as differential transmission spectroscopy) techniques have been used for the study of ultrafast material dynamics for the last 25 years, in varying degrees of complexity. One remarkable example is the extensive research into the nonlinear gain dynamics of both QW and QD semiconductor optical amplifiers [2, 3]. On the other hand, the nonlinear absorption dynamics are important for understanding electro-absorption modulators, and saturable absorbers to be used in mode-locked semiconductor lasers.

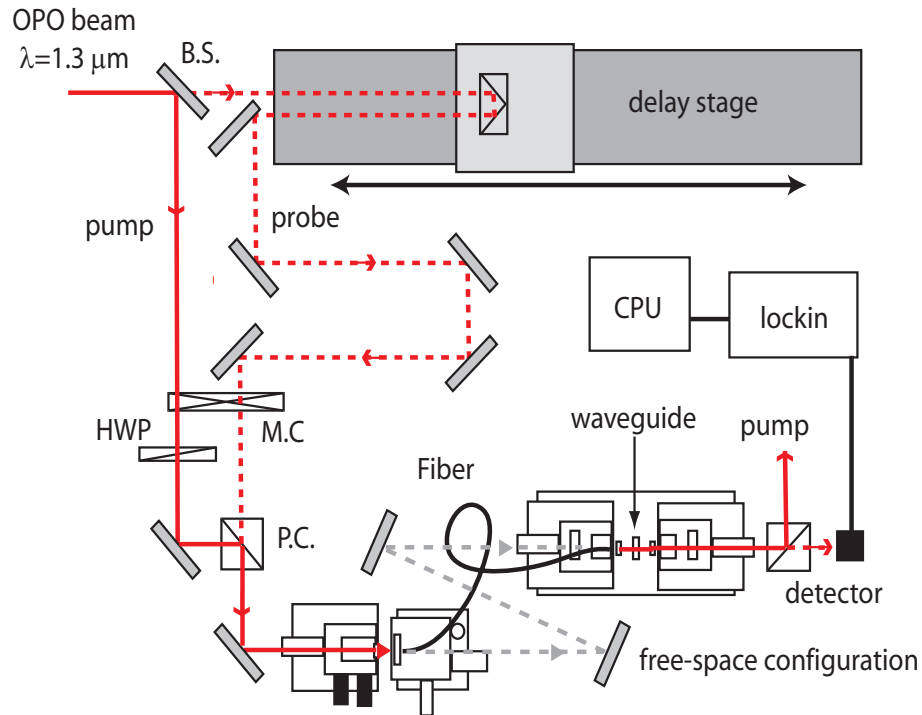


Figure 6.1: Degenerate Pump-probe setup. Pump and probe are orthogonally polarised and arrive at the modulator with a time delay determined by the translation stage. After passage through the device the pump is filtered and the modulated probe is collected by the phase sensitive detector apparatus.

The semiconductor nonlinearities can be characterized by using a strong optical pulse (Pump) to induce a carrier density change by either absorption or stimulated emission. Thereafter the change in transmission of a weaker pulse (probe) is measured by introducing a delay between the two pulses via a computer controlled delay stage, as shown in figure 6.1. The change in transmission of the probe can be related to the carrier lifetime (τ_r) in the framework of a simple two-level system approach as,

$$\frac{d\Delta N}{dt} = -\frac{\Delta N}{\tau_r} \quad (6.1)$$

$$\Rightarrow \Delta T \propto \exp\left(-\frac{t}{\tau_r}\right) \quad (6.2)$$

Here, ΔN refers to the change in carrier population with respect to the value at equilibrium (N_0) generated by the pump. A $1/e$ fit then yields the recovery time (τ_r), where the temporal resolution of the measurement is determined by the pulse duration.

The experimental setup used for all samples in this chapter is detailed in figure 6.1. The pulses were produced from a tuneable OPO (as detailed in chapter 3) with a pulse duration of 250fs and repetition rate of 82MHz. This allowed 12ns for the device to recover completely between successive pump pulses. The output spectrum of the OPO is monitored in realtime and its length is tuned to oscillate at the specific ground state transition of interest (around 1300nm for the devices measured). The beam is then split via a beam-splitter, after which one weak beam (probe) travels to a corner cube reflector on the computer controlled delay stage. The second stronger beam (pump) proceeds via a half wave plate (HWP), which rotates the polarisation to the TM plane (perpendicular to the growth plane of the devices). This allows orthogonally polarised pump and probe to be separated after propagation through the device. Filter wheels in both pump and probe arms allow for the adjustment of beam intensities (with typical pump:probe ratio >10:1) as the probe needs to be kept in the linear regime and care is taken so it does not also saturate the absorption of the device under investigation. A double mechanical chopper (MC) modulates one beam at f_1 and the other at f_2 , so the pump induced change in probe transmission (ΔT) for positive probe delays can be detected at the difference frequency $f_{dif} = f_1 - f_2$, in order to reduce the noise. The pump and probe recombine via a polarising beam-splitting cube (PBS) and are launched into a polarising maintaining fibre (minimum dispersion at 1300nm), thereafter entering the waveguide device via a 40x aspheric lens. The output from the device is collected via a 20x aspheric lens and passes through a polarising beam-splitter which rejects the remaining pump beam. The modulated probe beam is then collected by a large area germanium detector and the differential probe signal at f_{dif} is recorded by phase detection. The lock-in amplifier takes the detected signal and

the chopper reference and multiplies the two together. As both signals are modulated at the same frequency, the filtered DC component of their product is proportional to the integrated power of the differential probe signal.

6.2.1 Ultrafast carrier dynamics

The following work focusses on devices measured in absorption, however it is important to explain the features present in pump probe traces for the transparency and gain regimes also. Figure 6.2 shows all three modes of operation of active semiconductor waveguides, in particular the semiconductor optical amplifier.

When the pump and probe initially meet at zero delay, there is an overall step in the probe transmission which follows the profile of the pulse. This occurs in all three regimes of operation due to TPA (between pump and probe), and the direction of the step depends on whether the device is in gain or absorption.

In addition to this, there is a large carrier density generated over a narrow spectral range which gives rise to spectral hole burning (SHB) on the order of 150-200fs. This maybe outwith the resolution limits used in the following experiments, however the effect is to locally bleach a spectral hole in the material. In absorption (6.2(a)) this increases the probe transmission locally in time until carrier-carrier scattering generates a new quasi-fermi distribution. The same occurs in the gain regime (6.2(c)) but with a net decrease in probe transmission due to the local availability of empty states. The slight fluctuation which occurs shortly after zero delay in the case of transparency (6.2(b)) is due to an effect known as the 'spectral artifact', which links the gain and refractive index [4]. In all cases SHB is delayed from zero delay due to the finite scattering time of carriers.

Looking at the longer timescale upto 2ps, there is an asymmetry to the overall change in transmission feature. Carrier heating and subsequent cooling are the mechanisms responsible for this, as the new distribution couples to the lattice temperature via electron-phonon interactions. This can be seen in all three regimes in figure 6.2.

The final feature is the the long lived recovery occurring from band filling, which is not fully shown in fig 6.2, and appears truncated. For the case of absorption the change in probe transmission is increased due to the filling of states from absorption of the pump pulse. Conversely for the gain case, the pump depletes carriers via stimulated emission

and thus the probe transmission is decreased. At transparency, the stimulated transitions are balanced with the absorption, giving no net gain and hence no long lived change in probe transmission.

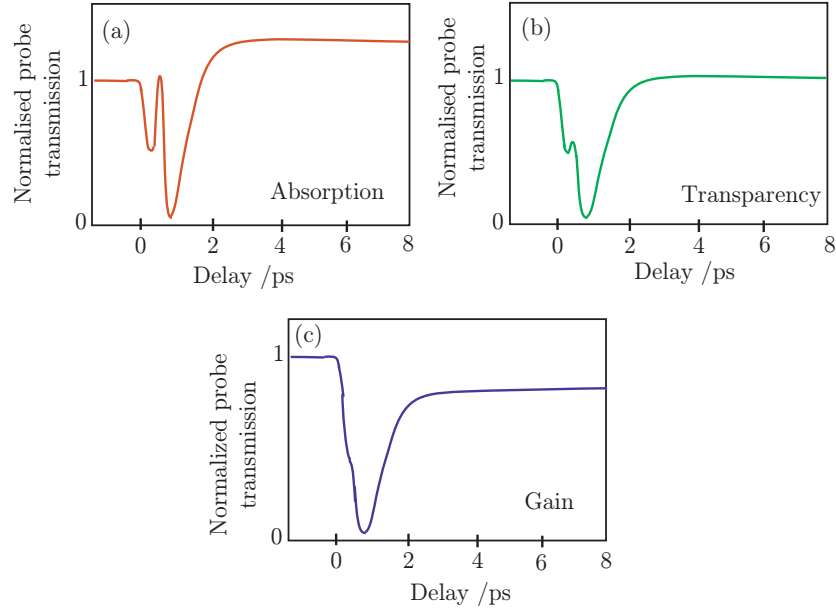


Figure 6.2: (a) Examples pump-probe traces for absorption, (b) transparency and (c) gain.

For quantitative analysis of such processes, it is common to implement a curve fitting method using impulse functions [5, 6]. The purpose of which is to separate the transmission changes with different time constants for the overall absorption (or gain) trace. The method involves generating a response function for the semiconductor, containing terms for each of the ultrafast carrier mechanisms mentioned above. This is subsequently correlated with a function describing the autocorrelation of a gaussian pulse (as generated by the OPO), and this gives a trace. By comparing with the experimental trace, a least squares fitting procedure can be used to obtain characteristic times for the individual processes. Initially times are chosen as educated guesses based on the exponential trace.

6.2.2 Waveguide coupling efficiency

Semiconductor nonlinearities are power dependent and it is essential to know how much of the input power is coupled into the devices. Two methods were used, fibre coupling and free-space coupling.

Fibre coupling

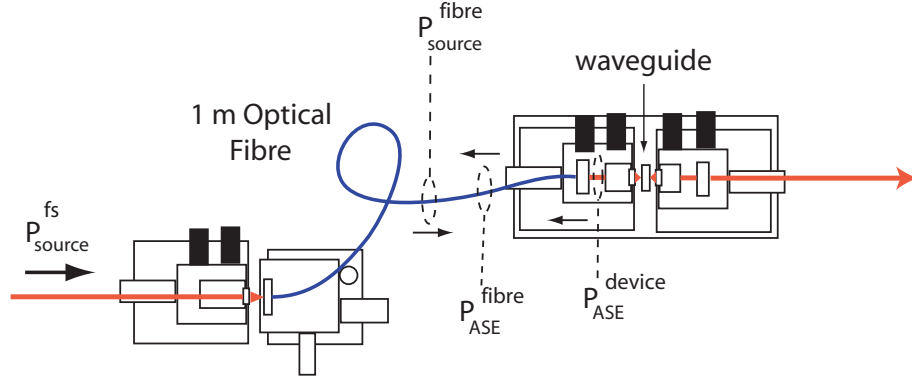


Figure 6.3: Schematic for fibre coupling light into waveguides.

The device was mounted on a brass block with silver conductive paint and placed in between two xyz translation blocks, which hold the input (40x aspheric) and output (20x aspheric) micro lenses. A thermoelectric cooler sandwiched between the brass mount and the waveguide stage is maintained at 25 °C using a thermistor positioned close to the device and a PID controller. To ease the day to day alignment after subsequent relaxing of the mechanical mounts the pump and probe were initially fibre coupled to the input side of the device. In order to estimate the efficiency of this coupling, we evaluated the coupling efficiency of both the femtosecond source and the amplified spontaneous emission (ASE), by applying forward bias to the device, into each end of the polarisation maintaining fibre. Using a calibrated Melles Griot power meter the ASE is measured before and after propagating through the fibre, using a fibre coupled germanium detector and oscilloscope for optimisation. A similar method on the source input side of the fibre gives the following relations,

$$\eta_{device \rightarrow fibre} = \frac{P_{ASE}^{fibre}}{P_{ASE}^{device}} \quad (6.3)$$

$$\eta_{fs \rightarrow fibre} = \frac{P_{source}^{fibre}}{P_{source}^{fs}}. \quad (6.4)$$

Similar approaches have been used elsewhere [7] and it can be seen that the overall coupling efficiency can be obtained by multiplying the individual contributions together

giving,

$$\eta_{total} = \left[1 - \left(\frac{n_{device} - 1}{n_{device} + 1} \right)^2 \right] \times \left(\frac{P_{ASE}^{fibre}}{P_{ASE}^{device}} \right) \times \left(\frac{P_{source}^{fibre}}{P_{source}^{fs}} \right). \quad (6.5)$$

The first term on the right hand side of equation 6.5 is the transmission through the facet due to the absence of anti-reflection coatings, having a typical value of 70%. In addition typical values for $\eta_{device \rightarrow fibre}$ and $\eta_{fs \rightarrow fibre}$ were 3% and 37% respectively, giving an overall coupling coefficient of $\eta_{total} \approx 0.08\%$.

Free-space coupling efficiency

For some of the measurements it proved difficult to couple sufficient ASE from the device to the fibre and we used free-space coupling, where the fibre and its assembly was replaced by two mirrors as seen in figure 6.1. The input was optimised by measuring the photocurrent in the device using electrical probes, whilst the ASE device output was aligned as far back in the optical setup as possible using pin holes.

In order to estimate the free-space coupling efficiency we used data from photocurrent measurements carried out with the continuum generator (see chapter 5). The photocurrent generated in a waveguide can be written as follows, where η is the quantum efficiency and P_{abs} is the amount of power that is absorbed by the material (in this case QDs),

$$I_{ph} = \frac{q\eta}{\hbar\omega} P_{abs}. \quad (6.6)$$

The power that is absorbed is only a fraction of that which is lost in the waveguide by both material (α_{QD}) and intrinsic losses (α_i) from scattering, radiation and free-carrier absorption. Therefore we can write,

$$P_{abs} = CP_{in} \left(\frac{\Gamma\alpha_{QD}}{\alpha_i + \Gamma\alpha_{QD}} \right) [1 - e^{-\alpha_i L - \Gamma\alpha_{QD} L}]. \quad (6.7)$$

In the above expression C is the coupling coefficient, P_{in} is the power at that facet and Γ is the waveguide confinement factor. From previous measurements in chapter 5, we know that the absorption coefficient ($\Gamma\alpha_{QD}$) due to the QDs at 1280nm is $16cm^{-1}$. Typical intrinsic losses found from the literature for waveguides are $15-17cm^{-1}$ [8, 9]. If

we therefore combine equations 6.6 and 6.7 and rearrange to find C we have,

$$C = \frac{I_{ph}\hbar\omega}{q\eta P_{in}} \left(\frac{\alpha_i + \Gamma\alpha_{QD}}{\Gamma\alpha_{QD}} \right) [1 - e^{-\alpha_i L - \Gamma\alpha_{QD} L}]^{-1}. \quad (6.8)$$

The first term on the RHS was found from direct photocurrent measurements giving 0.01. The second term gives the fraction of power absorbed by the QDs and has a value of ≈ 2 , whilst the last term becomes negligible by making the assumption that all of the power is absorbed in the device. This is a valid approximation as very little light emission was detected from the back of the waveguide at 1280nm. The coupling coefficient is therefore estimated as 0.02 (2%), which was extremely useful when selecting the input power for pump and probe in similar devices using free-space coupling.

6.3 Time dependent carrier escape in InAs Dots-in-a-well (DWELL)

When it comes to quantum dots, the interest in ultrafast carrier dynamics has in the past tended to focus on lasers [10], and optical amplifiers for applications in high speed systems [11]. Carrier capture into excited states, relaxation via carrier-carrier scattering and carrier-phonon interactions have been well documented [12, 13]. However, less effort has been devoted to the investigation of the carrier escape mechanisms relevant to saturable absorber type devices. This is in contrast to the extensive work previously carried out in InP based QW devices. In particular saturable absorbers comprising QD material have been used as mode-locking elements in solid state and semiconductor lasers [14, 15]. With the application of a reverse bias on the QD absorber region sub-picosecond pulses have been reported from passively mode-locked lasers (MLL) at $1.3\mu\text{m}$, where pulse shortening was observed by increasing the reverse electrical bias [16, 17]. To date, the carrier dynamics in InAs QD p-i-n structures have been investigated typically via deep level transient spectroscopy (DLTS)[18], time-resolved photoluminescence (TRPL) [19] and by a combination of photocurrent and photoluminescence measurements [20, 21]. In those studies, thermionic emission and tunneling were identified as the major escape mechanisms. DLTS is a capacitance transient thermal scanning technique [22] whereby an electrical pulse is sent to the junction bias and the capacitance transient recovery is

then measured. TRPL is applied in the optical domain, however the excitation is not degenerate with the specific transitions of interest.

The QD DWELL device was bonded as mentioned above and kept at room temperature throughout the following measurements. Electrical probes on both the p-side and n-side of the device were used to apply the reverse bias across the p-i-n junction. By using the pump-probe method we directly map out the field dependent absorption recovery, requiring no measurement of electrical transients, so that the results are independent of the time taken for carriers to drift to the electrical contacts. We carried out DTS on the above sample for reverse applied voltages ranging from 0 to 10V (270KV/cm). The measured traces are shown in figure 6.4.

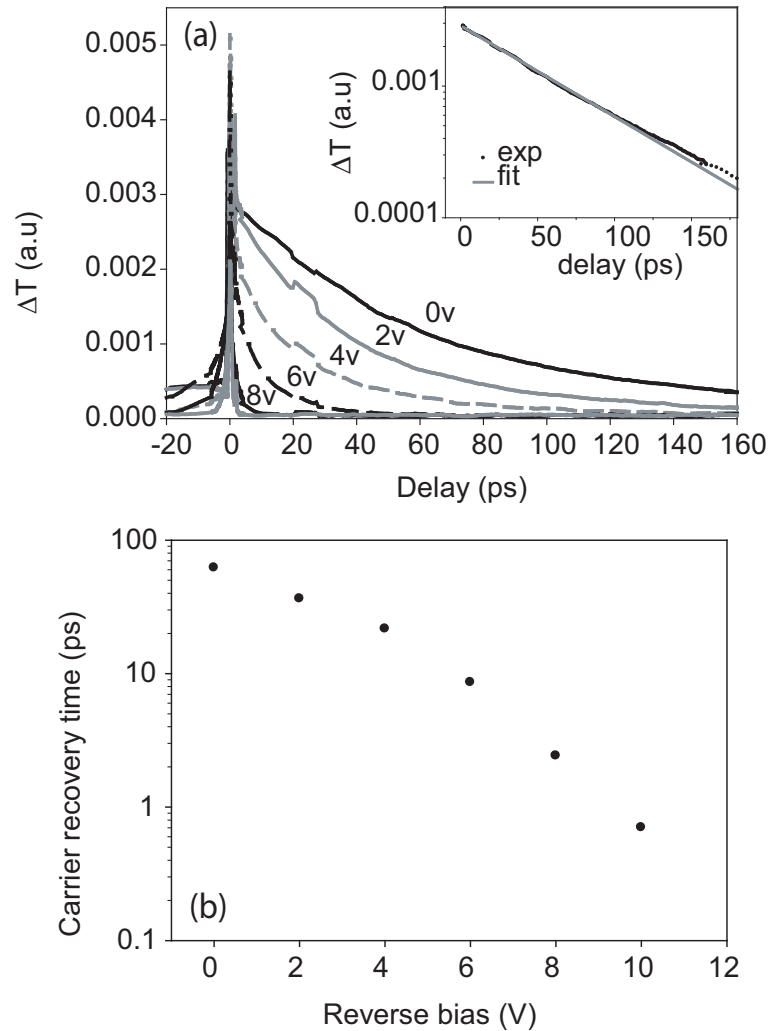


Figure 6.4: (a) Time resolved pump-probe traces for increasing reverse bias on the QD saturable absorber, and single exponential fit for 0V (inset). (b) Absorption recovery times from exponential fitting.

The pump and probe pulse energies employed were 580fJ and 58fJ respectively. The strong pump pulse therefore causes absorption saturation through band-filling and gives rise to a step-like increase in probe transmission. Interestingly, we see no evidence of field screening effects in the leading edge of the traces [23] which leads us to believe that any such effect is minimal due to the low density of photo-generated carriers in the dots (dot density $\approx 5 \times 10^{10} \text{cm}^{-2}$). The spike observed at zero delay can be attributed to interference between the overlapping probe pulses and the leaked TE polarised component of the pump pulses.

With increasing probe delay, the transmission decays as photo-generated electrons and holes either escape or recombine. We found that the measured absorption recoveries fit best to a single exponential of the type $\exp(-t/\tau)$ in a simple rate equation model (6.2), where τ is the recovery time [inset Fig. 6.4(a)]. As depicted in Fig. 6.4(b), the recovery time decreases by almost two orders of magnitude from 62ps to 700fs as the reverse applied voltage varies from 0V to 10V. These results suggest that the dynamic response of our device is limited by one type of carrier only, in contrast to measurements reported in other QD structures with no applied bias [24]. The reason for this is the difference in effective mass of electrons and holes. As the confinement band offset is asymmetric in such structures ($\Delta E_c : \Delta E_v = 70 : 30$) [21] it would be logical to infer that the escape rates for electrons and holes would be different.

From inspection of 6.4(b), the trend of the absorption recovery times versus voltage deviate from a straight line relationship (which would be the case if only one exponential rate was responsible), indicating the presence of multiple processes. We consequently determine a series of overall rates $\Gamma (=1/\tau)$, which can be expressed as the sum of contributions from recombination (Γ_{rec}), thermionic emission (Γ_{th}), and tunneling (Γ_{tun}) mechanisms given by,

$$\Gamma = \Gamma_{rec} + \Gamma_{th} + \Gamma_{tun}. \quad (6.9)$$

The short recovery time measured at zero applied field, 62ps, suggests that the contribution of recombination processes is not significant at room temperature (given the nanosecond recombination times typically reported in similar material systems [25]).

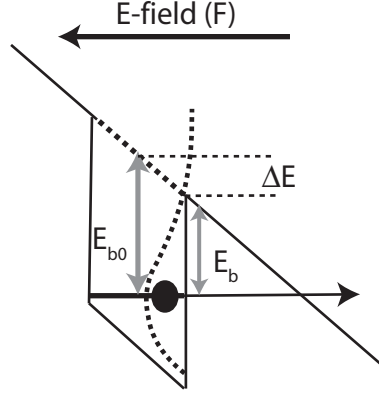


Figure 6.5: Schematic depicting the electric field effects on the quantum dot state.

The effect of an applied reverse field is three-fold. Firstly, it causes a lowering of the barrier height

$$\Delta E = E_{b0} - E_b = a|q|\frac{F}{2} \quad (6.10)$$

where a is the dot height and q is the electron charge. F is the electric field, calculated as $F = (V + V_{bi})/d$, where V is the applied reverse voltage and V_{bi} is the measured built-in potential (0.8V). Secondly, the carrier confinement energies are red-shifted due to the quantum confined Stark effect (QCSE). CW transmission measurements (see chapter 5) yielded a maximum ground state stark shift of 18meV (to which both electrons and heavy holes contribute) at 10V reverse bias. This shift is negligible compared to the linear change in the barrier height found from equation 6.10, and is therefore not taken into account in the discussion to follow. Thirdly, the applied field causes the formation of a triangular barrier. For high applied fields the width of this barrier can decrease sufficiently to allow carriers to tunnel from the ground state, as discussed in chapter 2.

At low bias, tunneling processes are highly improbable and thermionic emission is expected to be the dominant carrier escape mechanism. We assume a common thermally activated emission rate equation [26] modified only by the linear reduction in the barrier height. Similar approaches have been extensively used for the thermionic emission of carriers from quantum wells [27].

$$\Gamma_{th} = \Gamma_0 \exp \left[\left(\frac{aqV}{2d} \right) \frac{1}{k_b T} \right], \quad (6.11)$$

where Γ_0 is the rate for no applied voltage ($V = 0$). k_b and T are the Boltzmann constant and absolute temperature, respectively.

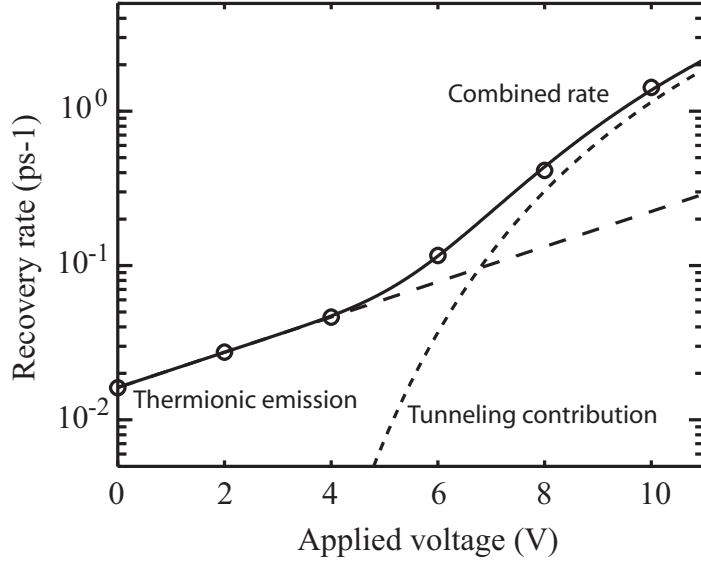


Figure 6.6: Rate equation fitting for pure thermionic emission, tunneling, and the combined carrier escape rate from the ground state.

In figure 6.6, only the first three data points fit satisfactorily to an equation of the form $A \cdot \exp(B \cdot V)$. This yields $B = 0.263 \pm 0.019 \text{ V}^{-1}$, in excellent agreement with the expected linear reduction of the barrier height calculated from (6.10) (0.278 V^{-1}), thus justifying our assumptions regarding the Stark shift and the recombination rate. It can be seen that this fit diverges for applied biases beyond 4V, suggesting a significant contribution from an additional escape mechanism.

The escape rate corresponding to tunneling processes in the applied field direction can be calculated as the product of the barrier collision frequency [28] and transmission probability through such a barrier as described in chapter 2,

$$\Gamma_{tun} = \frac{\hbar\pi}{2m_d^*a^2} \exp\left(-\frac{4\sqrt{2m_b^*}E_b^{3/2}}{3q\hbar F}\right). \quad (6.12)$$

Here, m_d^* and m_b^* are the effective carrier masses in the dot and buffer material, and E_b is the barrier height. Using the previous fit at low applied voltages, the thermionic contribution was subtracted from the total measured rates. The remaining contribution

was then fitted with equation 6.12. The field dependence of Γ_{tun} is most heavily weighted by the $1/F$ factor in the exponential transmission term, so we assume a constant barrier height E_b in our fit. We use this approximation to highlight the basic physical trend of the tunneling mechanism. The fit yields a barrier collision frequency of $395ps^{-1}$ from which we estimate an effective mass in the InAs dot to be $0.02m_0$, where m_0 is the free electron mass. Within the simplicity of our model, this leads us to believe the dynamics observed in our measurement can be attributed to the electrons. This is namely due to the fact that in InAs and GaAs, the heavy hole mass is one order of magnitude larger than this.

Figure 6.6 illustrates how the individual contributions of thermionic emission and tunneling dominate in the regions of low and high fields respectively. Also, note that the sum of these two contributions ($\Gamma_{th} + \Gamma_{tun}$) gives an excellent fit to the measured rates across the entire range of applied voltages. We believe our measurements are not resolving the very fast hole dynamics. Previously reported band offset ratios [29] indicate that, even at low fields the thermionic emission of holes would be well over one order of magnitude faster than for electrons. In addition, at larger electric fields, it is likely that the hole bound states merge with the continuum due to the lowering of the barrier.

6.3.1 Temperature dependent escape in InAs DWELL

In monolithic mode-locked semiconductor lasers, spontaneous emission noise from the gain section of the lasers is absorbed by an unbiased section. This generally involves a fast recovering saturable absorber which modulates the loss of the cavity at the roundtrip frequency and leads to pulse formation [30]. Additionally, in the presence of gain saturation, coupled with absorption saturation, a slower recovering saturable absorber can be used, whereby the two mechanisms open up a time window of net gain. This then amplifies and shapes the pulse upon successive round trips.

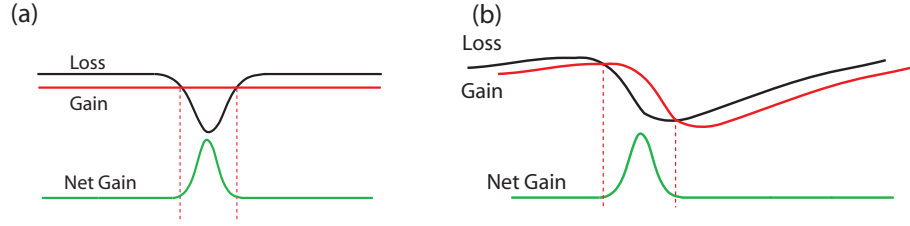


Figure 6.7: (a) Schematic showing pulse generation mechanism in passive mode-lock lasers in the absence of gain saturation and (b) with gain saturation.

A fast absorber is desirable in the case of semiconductor lasers due to their short cavity roundtrip time. Absorption recovery should be less than or comparable to this value, typically tens of picoseconds. Applying a reverse bias or temperature elevation assists the carrier escape, decreasing the recovery time of the absorber as shown previously. To date pulse widths of 400fs at 21GHz from monolithic two-section devices have been reported [16]. Additionally pulse width duration has been seen to decrease for fixed reverse bias by increasing the temperature [31]. Another benefit of fast absorbers is the reduction of high order dispersion due to pulse propagation. Self-phase modulation (SPM) in slow saturable absorbers leads to erosion of the red-shifted leading edge, giving pulse broadening as the instantaneous frequency of the pulse is blue-shifted [32]. An assessment of carrier escape from such structures will prove valuable for modeling the processes responsible for pulse formation, for example [33].

results

As seen in the previous section, at room temperature, and below 4V, thermionic emission is predominantly responsible for carrier escape in this device. The following work details pump probe measurements within this regime (2V reverse bias), whilst elevating the device temperature from 20 °C to 47 °C by way of the thermoelectric cooling element. Previous measurements from the literature using time-resolved photoluminescence (TRPL) at reduced temperatures (10K - 130K), have successfully demonstrated emission back into the wetting layer of QD structures [25].

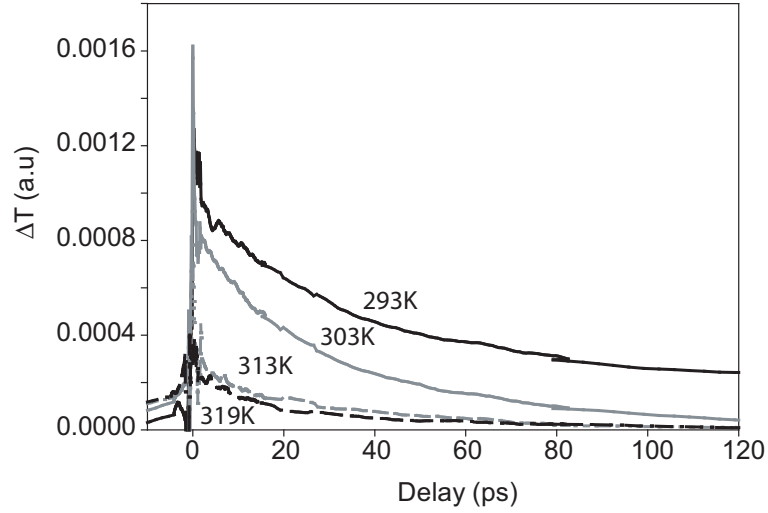


Figure 6.8: Absorption recovery in an InAs DWELL QD saturable absorber for a reverse bias of 2V over an elevated temperature range.

In figure 6.8 the absorption recovery fits very well to single exponential functions indicating the dynamics are dominated by one type of carrier, as previously observed in the measurements as a function of applied field. The characteristic times are then fitted to the following thermionic emission rate equation as discussed in chapter 2,

$$\Gamma_{therm} = AT^2 \exp\left(-\frac{E_b}{k_b T}\right). \quad (6.13)$$

In the above expression E_b is the barrier height, T is the absolute temperature and A is a material dependent constant. We fitted the absorption recovery times with such an equation and the results are shown in figure 6.9(a).

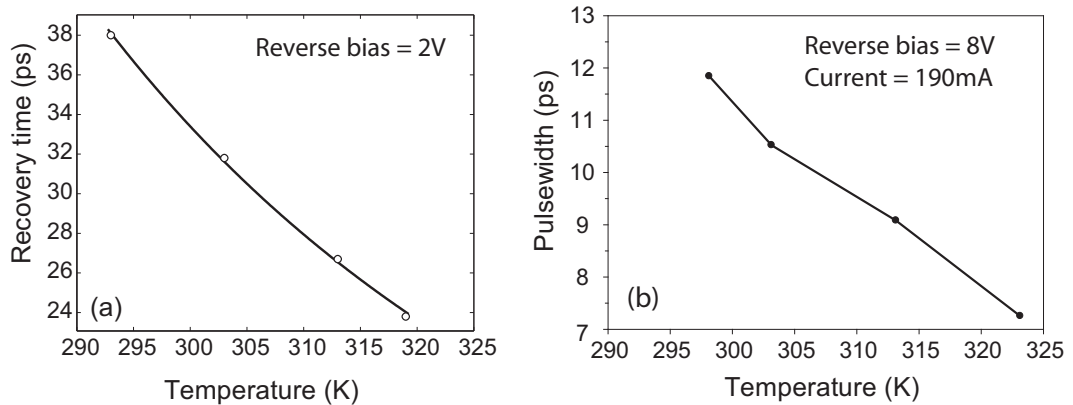


Figure 6.9: (a) Absorption recovery time fitted to a thermionic rate equation. (b) Comparison with pulse width from a similar two section mode-locked laser over the same temperature range.

In figure 6.9 the transmission change recovers with characteristic times ranging from 38ps (20 °C) down to 24ps (46 °C) at a constant reverse bias of 2V (55KV/cm). This gives a 37% decrease in recovery time up to a temperature of 46 °C. A similar reduction in the pulse width (41%) of a test, two-section mode-locked laser indicates that thermionic emission is a prominent mechanism for pulse shortening by way of absorber recovery [34].

6.4 Absorption recovery in InAs/GaAs Bilayer QD's

The need for greater gain in QD structures over the last 20 years has focussed attention on the growth of multiple QD layers with sufficient spacing to avoid electronic coupling [35]. However it was later found in lasers that vertically coupled QDs exhibit desirable properties such as low current densities [36]. It has been shown previously that strain-engineered bilayer QDs can provide enhanced long wavelength emission and a narrower inhomogeneous linewidth with higher peak gain [37]. In the previous chapter we demonstrated the large Stark shift present in such structures. The following work outlines the absorption recovery dynamics in the same structure, for the potential application in electro-absorption modulators and saturable absorbers as mode-locking elements.

Absorption recovery was measured using the previous pump probe apparatus with the wavelength tuned to the ground state of the sample at 1340nm. The pump was polarised TM (perpendicular to the growth plane), whilst the probe was polarised TE (parallel to the growth plane). The fibre coupling assembly was replaced by two high reflecting mirrors to enable the pump and probe to be coupled via free space into the device. The coupling efficiency is slightly improved in this configuration ($\eta \approx 2\%$), giving pump and probe energies in the device of 380fJ and 31fJ respectively. The absorption recovery was investigated for the range of applied reverse biases up to 10V (corresponding to a field of 200KV/cm), initially at every 2V and then at a later date, including every volt. The probe transmission was recorded with a germanium detector using phase-sensitive detection and the results are shown in figure 6.10.

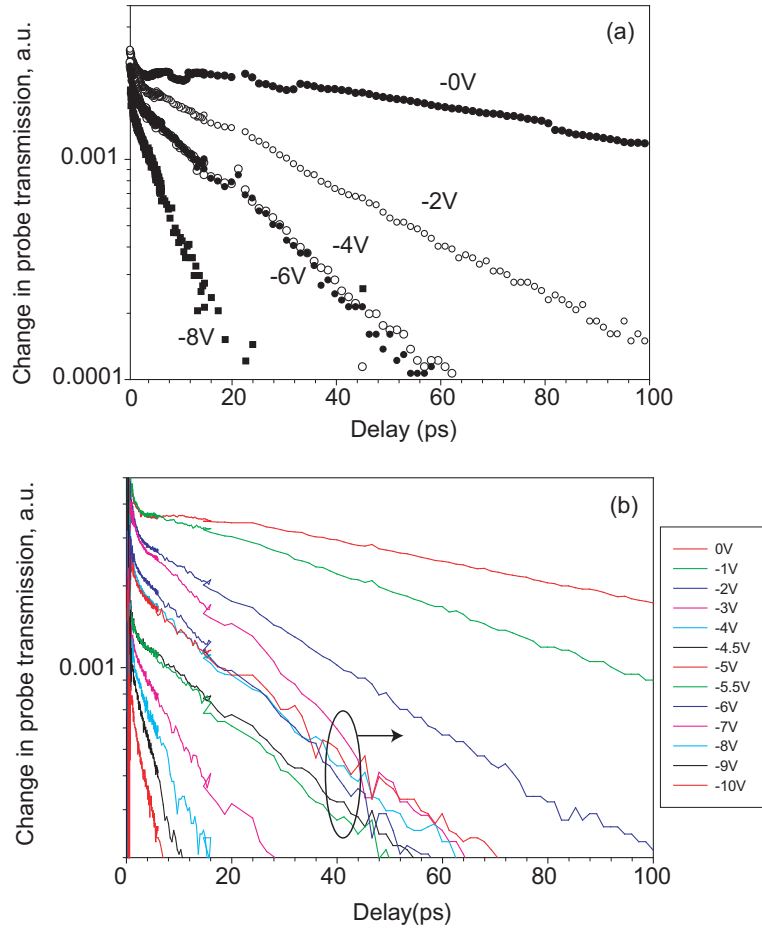


Figure 6.10: (a) Absorption recovery in a InAs bilayer p-i-n waveguide over an initial set of voltages. (b) A finer range of voltages, indicating the very similar recovery rates around 5v.

The long-lived absorption recovery, which is a limiting factor in switching applications fits well to a single exponential with characteristic times ranging from 119ps to 5ps, as seen in figure 6.11. Such fast absorption recovery offers the possibility of modulation speeds in excess of 100GHz. In addition, there are two sets of measurements in figure 6.11 (empty and full circles). These refer to data collected on the same sample but on different days and show excellent agreement with each other, indicating the accuracy of the measurements.

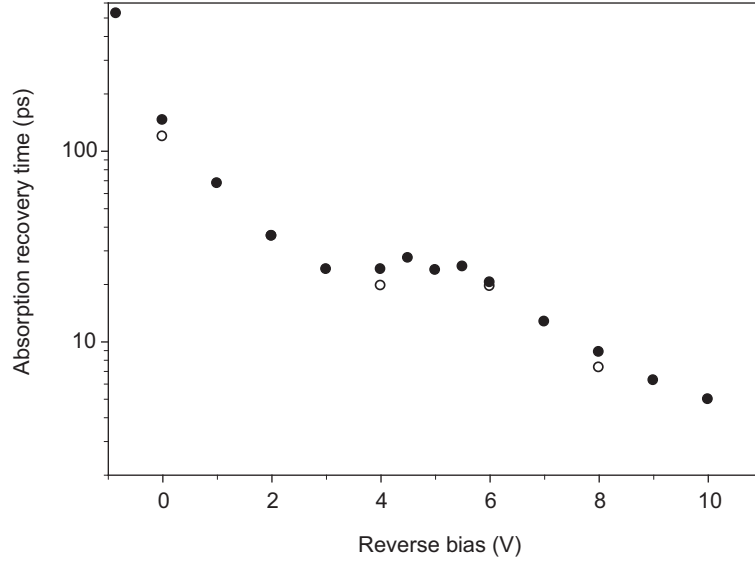


Figure 6.11: Absorption recovery times for an InAs bilayer p-i-n waveguide fitted with single exponentials.

Looking at fig 6.11, there is clearly a feature between 4V and 6V where the recovery stagnates at approximately 20ps. To understand this we must first think about the mechanisms by which electronic injection occurs in the bilayer structure. The carriers are captured into the smaller QDs (seed layer). Thereafter they transfer by a resonant tunneling effect into the excited state of the larger dots (in the adjacent layer), before relaxing to the ground state.

These capture mechanisms have been extensively studied using photoluminescence (PL) measurements and time-resolved PL exciting into the GaAs barrier, wetting layer and the QD states directly. In the case of highly correlated bilayer dots (GaAs spacing of 30ML) the overall relaxation mechanism has been found to be dependent on the radiative lifetime of the electrons in the larger dots (second layer) [38]. This demonstrates that carrier transfer from small to large dots is a dominant relaxation channel in such coupled systems. When a reverse bias is applied, this creates a resonant escape route for the carriers initially in the excited state of the large dots. The most likely mechanism for this would be thermionic emission, having been identified using PL measurements as a transport process between different sized dots which are in the same layer [39, 40]. However as a reverse bias is applied, the band sloping that is part of the QCSE acts to reduce the fast tunneling contribution whilst the energy levels are shifted by differing amounts (due to their size

difference).

In the case of extremely large fields, the wave function overlap can be greater between the ground state of both dots than between the second layer excited state and seed layer ground state. In this case a resonant tunneling contribution could be drastically reduced over a finite voltage range, whilst re-appearing when a resonant path is again established. Similar mechanisms have been observed in multiple quantum well devices [41], whilst tunneling times between bilayer dots have been shown to be comparable to asymmetric double $GaAs/Al_xGa_{1-x}As$ QWs with similar well separations [42, 43]. This supports the interpretation given here of QDs in closely coupled systems.

Within bilayer QD systems a multiple LO phonon mediated, non-resonant (due to inhomogeneous size distribution) tunneling process has been proposed [44, 45]. This was measured by integrating PL from each of the dot layers and then using the ratio as a yield, to quantify the transport time (τ_{dwell}) between the layers. In the former case these times at 6K were found to be in qualitative agreement with the theory of such QD pairs separated by $\sim 10\text{nm}$ [46].

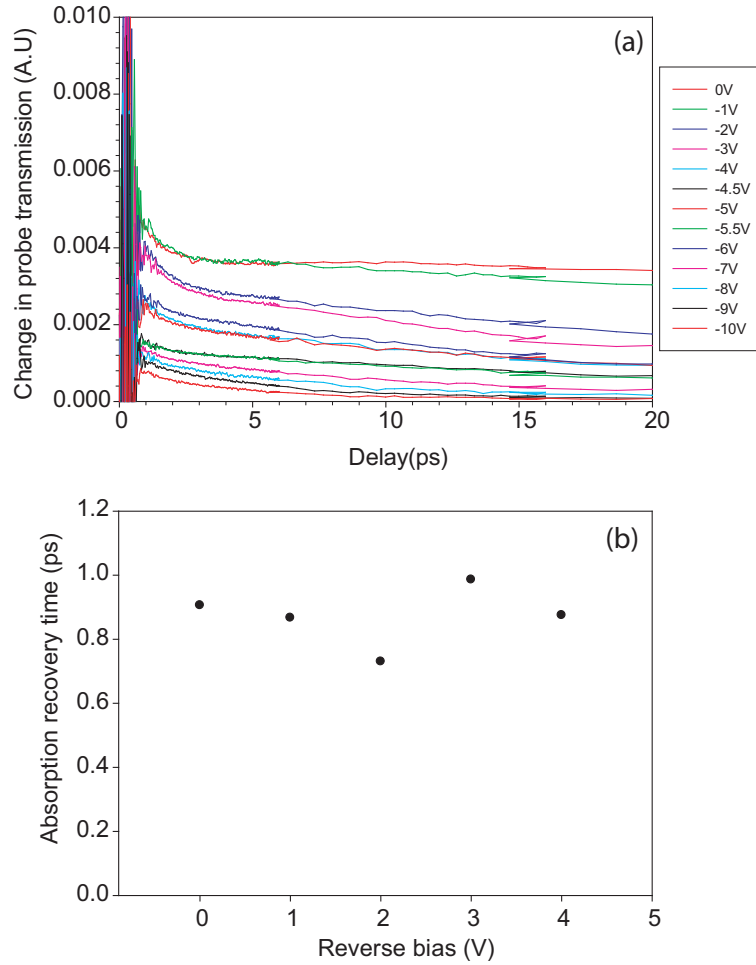


Figure 6.12: (a) Probe transmission indicating absorption recovery in bilayer QD waveguide. (b) Absorption recovery times for the fast component of pump probe bilayer QD measurements.

An explanation for pump probe results in figure 6.11 could be, when the excited state of the large dots is resonant with the ground state of the smaller dots (the seed layer), the carrier emission is dominated by two thermal escape rates (one from each dot). The faster of the two being due to tunneling to the smaller dots and subsequent thermionic emission from a dot with a lower barrier height. As the reverse bias reduces the wave function overlap between the two layers, the resonant tunneling contribution would almost be switched off, returning when the overlap was significant between another two resonant levels. This is a simple explanation for what is clearly a very complicated correlated electronic system, the modeling of which is beyond the scope of this thesis.

One further interesting feature in the pump probe traces is the initially fast absorption recovery, that can be seen in more detail in figure 6.12(a) above. These recoveries fit well to

single exponentials and the recovery times are plotted in figure 6.12(b). Upon inspection the dependence of this recovery on the applied bias is not clear. These times are close to the resolution limit imposed by the pulsewidth, which could introduce some uncertainty in the measured values. If the escape was due to a less confined carrier (holes in the valance band), one would expect this absorption recovery to account for exactly half the absorption saturation, which is not the case. The most likely explanation is carrier thermalisation of the distribution which could be mediated via carrier phonon interactions. This would explain the consistency of the time dynamic, however one would expect such a contribution to be present even at high applied fields.

6.5 Field dependent absorption dynamics in GaInNAs MQWs

The waveguide geometry of a saturable absorber under reverse electrical field is in many ways similar to an electro-absorption modulator (EAM), as seen in previous sections. Although EAMs employing quantum wells have been used for pulse generation in lasers [47], they have been more widely applied to demultiplexing [48], wavelength conversion [49] and signal recovery [50] in optical networks. The dynamic recovery of such components depends on rapid cross-well transport of carriers with subsequent escape or recombination of carriers out of the wells.

6.5.1 Field screening effects

The larger density of states in quantum wells relative to quantum dots, allows a larger density of carriers to be generated. Under optical injection, photogenerated carriers reduce the absorption due to band filling in the same way as in QDs, seen previously. However when suitable high densities of carriers are generated and escape out of the wells they can screen the applied electric field, which in turn leads to a change in the absorption through the QCSE. This effect has been observed experimentally in InGaAs/InP [51], AlGaAs/GaAs [52] and InGaAs/GaAs [53] p-i-n structures. Electrons (holes) temporally build up at the i-n (i-p) junction interface, leading to a characteristic blue-shift of the band-edge. This can be overcome by reducing the optical saturation by lowering the input optical power or increasing the reverse electric field in order to speed up the carrier sweep

out of the intrinsic region.

The absorption recovery dynamics have also been investigated in such structures, the Self-electro-optic effect device (SEED) being a particular example [54]. This device is similar to an EAM but exploits feedback from absorption saturation to operate as an optically bistable switch, where modulation at high frequencies is ultimately limited by any space-charge build up of carriers. In pump-probe investigations (pumping in the growth direction) of such a $Al_{0.3}Ga_{0.7}As/GaAs$ p-i-n modulator it was proposed that field screening from high optical intensities caused a reduction in the carrier escape from the QWs by thermionic emission and this caused an overall increase in the absorption of the device [41]. This has also been observed in QW waveguide devices [55]. The work of Miller et al. was subsequently modeled by solving the equations for carrier drift of the generated charge distribution outside of the wells [23]. In this model carrier diffusion was neglected and the field was presumed to be restored once the charge reached the p and n regions. In another approach, pump-probe measurements have been fitted in a similar manner to that described earlier in this chapter. One particular approach [56] used an overall response function which includes individual impulse response functions describing carrier escape, drift and diffusion, making up the contribution to field screening. In addition a contribution from absorption saturation of the exciton is included. This overall function was found to accurately describe the experimental results and introduce the idea of carrier recapture into the wells.

6.5.2 Results for absorption recovery

The GaInNAs/GaAs p-i-n device is described in chapter 4. The pump-probe setup is the same as that of figure 6.1, whilst the degenerate wavelength was chosen to be on the long wavelength side of the exciton at 1310nm. Two samples were used, which were identically processed and only differ with regards to their lengths, $500\mu\text{m}$ and 1mm respectively. In the case of the $500\mu\text{m}$ device (Sample A) the pump and probe pulse energies were 975fJ and 29fJ respectively. Whilst for the 1mm device (Sample B) the pump and probe pulse energies were 2.9pJ and 29fJ respectively. Both samples were pumped with TM polarised light and probed with TE light, and the results are presented in figure 6.13.

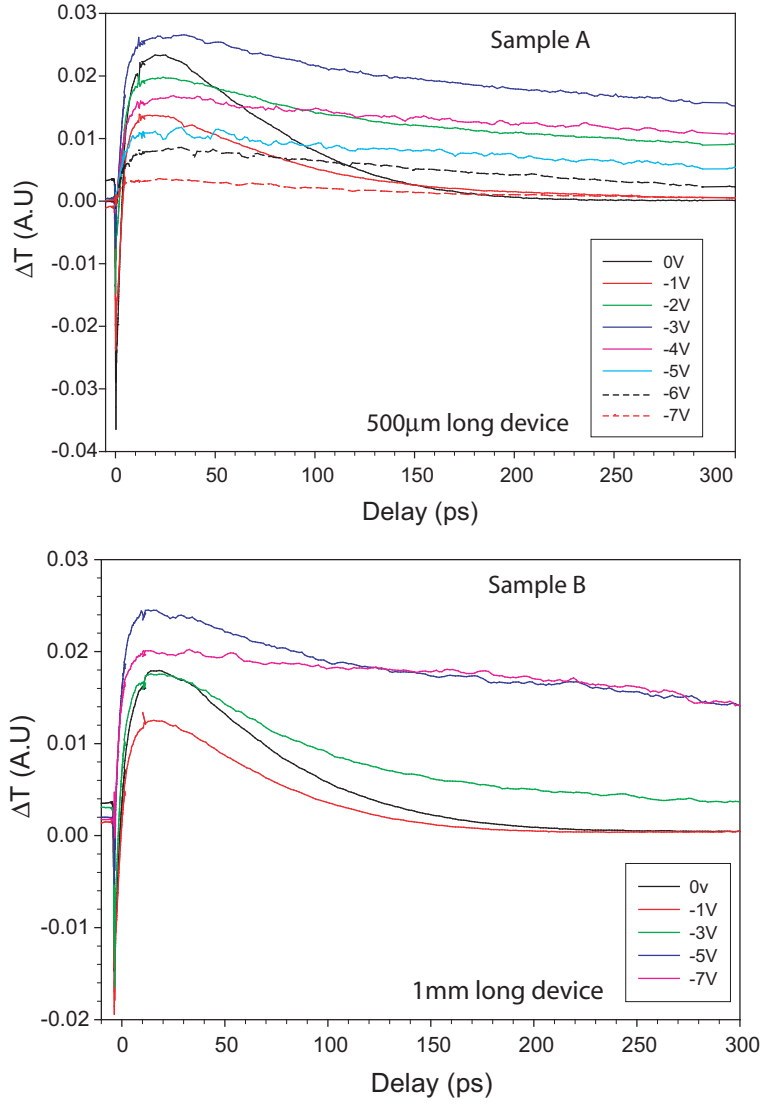


Figure 6.13: Pump probe traces for deeply etched (down to the active region) GaInNAs waveguide devices under reverse electric field, (a) $500\mu\text{m}$ long and (b) 1mm long.

In figure 6.13 the traces exhibit an overall absorption saturation and recovery. The initial reduction in probe transmission is due to TPA, after which absorption saturation occurs by band filling. Thereafter the absorption recovers on the order of 50-60ps for low applied fields, with the most likely mechanism being radiative and non-radiative recombination [57]. For higher fields the existence of field screening, reducing the carrier escape from the quantum wells is likely to occur, as previously mentioned. The longer device experiences a weaker optical pumping due to the limit of the OPO power output (it is difficult to accurately scale the power required for a nonlinear interaction in a device that is twice as long). The mechanisms responsible for absorption recovery at high fields have

previously been shown to be thermionic emission and tunneling. The long lived absorption recovery was therefore fitted to single exponentials and the results are shown in figure 6.14.

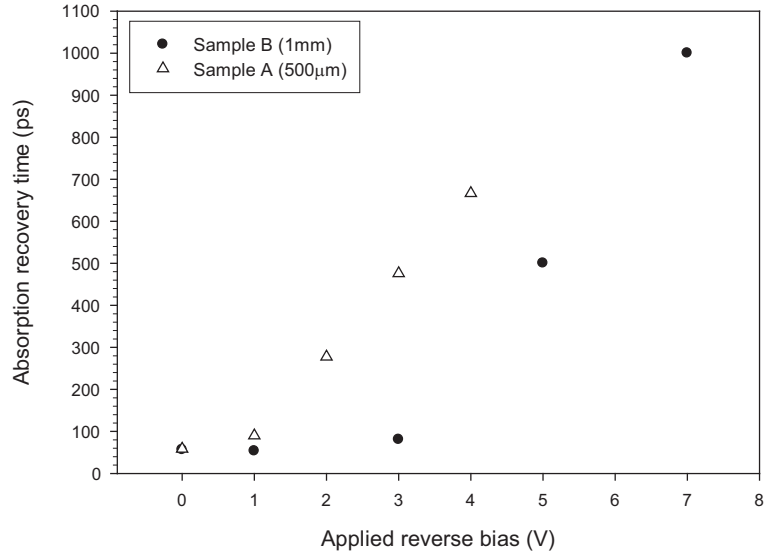


Figure 6.14: Pump probe traces for deeply etched (to the active region) GaInNAs waveguide devices under reverse electric field, (a) $500\mu\text{m}$ long and (b) 1mm long.

In figure 6.14 the recovery times for sample A did not fit to exponentials after 4V, however a clear distinction between low optical pumping (sample B) and high optical pumping (sample A) can be seen in the traces. The difference reflects the idea of increased field screening from higher optical pumping due to the larger number of photogenerated carriers present. From inspection of figure 6.13 for high reverse fields the overall absorption recovery appears to slow down, in contrast to previous investigations mentioned above.

6.5.3 Field screening dynamics involving heterobarriers

To describe the effects mentioned above we must take into account the epitaxial structure of the device. A separate confinement heterostructure (SCH) is common in waveguide based lasers and modulators, the point of which is two-fold. Firstly, by providing a refractive-index profile across the p-i-n junction, this gives high optical confinement for guiding of modes with low propagation loss. In addition it creates a large overlap of the optical mode with the active region improving the gain of the mode. Secondly, the refractive-index profile is achieved by using materials of differing band gap and by increasing the band offset this provides high confinement for electrically injecting carriers, which improves

the efficiency in laser devices. However, despite the advantages just mentioned the SCH restricts the escape of carriers in EAMs, as stressed by Hojfeldt et al. [58]. It has previously been shown that if the potential barrier of such a heterostructure is much larger than the thermal energy of carriers, these will pile up at the interface. In the case of the structures investigated in this work the heterobarriers are made of $Al_{0.6}Ga_{0.4}As$ where the barriers of the QWs are GaAsN (with 1% nitrogen). With such a high concentration of Al the ternary alloy exhibits an indirect band-gap, and using a typical conduction band offset (60:40) would lead to a potential barrier of $\sim 460\text{meV}$ (while $k_bT \sim 25\text{meV}$).

As the carriers build up further at the i-n (i-p) interfaces, electrons and holes become increasingly spatially separated, which reduces recombination and limits the overall recovery of the device. This is shown schematically in figure 6.15,

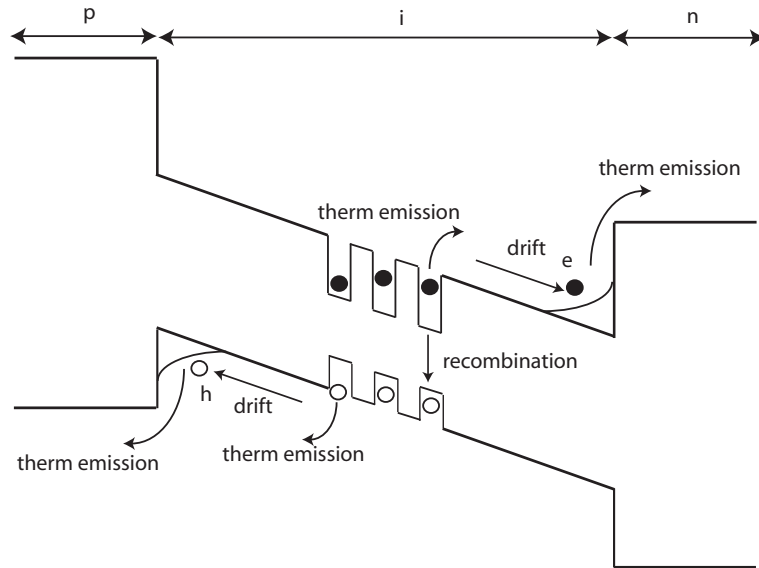


Figure 6.15: Schematic showing the escape mechanisms in a waveguide p-i-n device under reverse electric field, in particular the limiting effect of a heterobarrier.

This has been modeled extensively by Hojfeldt et al. [58] where for pulsed excitation, carrier recapture into wells was not expected to be significant and carrier diffusion was also minimal due to the times scales involved. Experimental measurements and theoretical modeling of the effects of increasing the optical intensity were investigated and found to increase the overall recovery time of the absorption modulator [59]. Although such an extensive theoretical model has not been applied to the device used in this thesis, we can qualitatively explain the results with such a model as follows.

For low applied fields radiative/nonradiative recombination is responsible for the fast recovery of the field screening. As the applied field is increased, carriers escape from the wells and drift towards the heterobarriers. This gives rise to the long lived transients as recombination is reduced due to the spatial separation of the electrons and holes. The long lived transients in the field screening increase with larger fields, as we believe absorption recovery is dominated by recombination and not by thermionic emission escape over the heterobarriers. We base this on the fact that the heterobarriers have extremely large potentials compared to the thermal energy of the carriers.

It must be noted that the sample investigated was not designed specifically as an EAM and as such these long lived field screening transients could be suppressed by optimising the design of the heterobarriers. In addition the material differs from that of Hojfeldt, and while GaInNAs has a more complex bandstructure than other III-V semiconductors these results show the potential of modulator devices due to the intrinsic fast absorption recovery demonstrated here.

6.6 Summary

We have directly measured, by optical means, firstly the electron escape time from the QD ground state in a reverse biased p-i-n DWELL structure. Absorption recovery times at room temperature ranging from 62ps (0V) to 700fs (-10V) were found, showing a decrease by nearly two orders of magnitude. We have given strong evidence that tunneling is responsible for the shortest absorption recovery times, in excellent agreement with previously reported trends observed in mode-locked lasers. Additionally, we have demonstrated close agreement of the temperature dependent absorption recovery and the pulse width shortening of pulses generated from a passively mode-locked laser, employing a similar saturable absorber. This indicates that thermionic emission plays a major role in absorption recovery in two extremes of reverse bias.

We have also measured absorption recovery in an InAs/GaAs bilayer QD p-i-n waveguide device, showing an ultrafast recovery of 5ps at a bias of -10V. This offers potential for modelocking elements in both solid state lasers and monolithic integration of passively modelocked semiconductor lasers, with the benefit of extending the operating wavelength.

Finally, the absorption recovery has been measured in a GaInNAs MQW waveguide p-i-n modulator. Such devices have been shown to have recovery limited by escape over the heterobarriers however, exploiting this increases the saturation power of such devices. Carrier recovery via escape from the QWs is shown to be very fast at low applied reverse voltages. In addition overall device recovery under no applied voltage was found to be 55ps, offering the potential for high speed modulators and mode-locking elements in this material system.

We note that absorption recoveries on the order of a picosecond are capable of producing sub-100fs pulses by passive mode-locking [16]. This should also prove useful in the development of sub-picosecond electro-absorption modulators for switching above 1THz.

References for Chapter 6

- [1] K L Hall, E R Thoen, and E P Ippen. *Semiconductors and Semimetals*, volume 59, chapter 2 Nonlinearities in Active Media. Academic Press, 1999.
- [2] K L Hall, G Lenz, E P Ippen, U Koren, and G Raybon. Carrier heating and spectral hole burning in strained-layer quantum-well laser amplifiers at $1.5\mu\text{m}$. *Appl. Phys. Lett.*, 61(21):2512, 1992.
- [3] P Borri, W Langbein, J M Hvam, F Heinrichsdorff, M H Mao, and D Bimberg. Spectral hole-burning and carrier-heating dynamics in InGaAs quantum-dot amplifiers. *IEEE J. Sel. Top. Quantum Electron.*, 6(3):544–551, 2000.
- [4] C P Hultgren, D J Dougherty, and E P Ippen. Above- and below-band femtosecond nonlinearities in active AlGaAs waveguides. *Appl. Phys. Lett.*, 61(23):2767, 1992.
- [5] K. L. Hall, A. M. Darwish, E. P. Ippen, U. Koren, and G. Raybon. Femtosecond index nonlinearities in InGaAs optical amplifiers. *Applied Physics Letters*, 62(12):1320–1322, 1993.
- [6] C. T. Hultgren and E. P. Ippen. Ultrafast refractive index dynamics in InGaAs diode laser amplifiers. *Applied Physics Letters*, 59(6):635–637, 1991.
- [7] L F Tiemeijer, P J A Thijs, T van Dongen, J J M Binsma, and E J Jansen. Polarisation resolved, complete characterisation of 1310 nm fiber pigtailed multiple-quantum-well optical amplifiers. *IEEE J. Lightwave Technol.*, 14(6):1524–1533, 1996.
- [8] R P Schreieck, M H Kwakernaak, H Jackel, and H Melchior. All-optical switching at multi-100-Gb/s data rates with Mach-Zehnder interferometer switches. *IEEE J. Quant. Elec.*, 38(8):pp1053, 2002.
- [9] J Shim, B Liu, J Pipek, and J E Bowers. An improved approach of optical loss measurement using photocurrent and optical transmission in an electroabsorption modulator. *IEEE Ph. Tech. Lett.*, 16(6):pp10–12, 2004.
- [10] D Bimberg, N Kirstaedter, N N Ledentsov, Zh I Alferov, and V M Ustinov. InGaAs-GaAs Quantum-Dot Lasers. *IEEE J. Sel. Top. Quantum Elec.*, 3(2):196, 1997.
- [11] T Akiyama, H Kuwatsuka, T Simoyama, Y Nakata, K Mukai, M Sugawara, O Wada, and H Ishikawa. Nonlinear gain dynamics in quantum dot optical amplifiers and its application to optical communication devices. *IEEE J. Quantum Elec.*, 37:1059, 2001.
- [12] S Schneider, P Borri, W Langbein, U Woggon, R L Sellin, D Ouyang, and D Bimberg. Excited-State Gain Dynamics in InGaAs Quantum Dot Amplifiers. *IEEE Phot. Tech. Lett.*, 17(10):2014, 2005.
- [13] T S Sosnowski, T B Norris, H Jiang, J Singh, K Kamath, and P Bhattacharya. Rapid carrier relaxation in $\text{In}_{0.4}\text{Ga}_{0.6}\text{As}/\text{GaAs}$ quantum dots characterized by differential transmission spectroscopy. *Phys. Rev. B*, 57(16):R9423, 1998.
- [14] A McWilliams, A A Lagatsky, C T A Brown, W Sibbet, A E Zhukov, V M Ustinov, A P Vasil'ev, and E U Rafailov. Quantum-dot-based saturable absorber for femtosecond mode-locked operation of a solid-state laser. *Optics Letters*, 31(10):1444, 2006.
- [15] X Huang, A Stintz, H Li, A Rice, G T Lui, L F Lester J Cheng, and K J Malloy. Passive mode-locking in $1.3\mu\text{m}$ two-section InAs quantum dot lasers. *J. Quantum Elect.*, 78(19):2825, 2001.
- [16] E U Rafailov, M A Cataluna, W Sibbet, N D Ii'inskaya, Y M Zadiranov, A E Zhukov, V M Ustinov, D A Livshits, A R Kovsh, and N N Ledentsov and. High-power picosecond and femtosecond pulse generation from a two-section mode-locked quantum-dot laser. *Appl. Phys. Lett.*, 87(8), 2005.
- [17] M G Thompson, A Rae, R L Sellin, C Marinelli, R V Penty, I H White, A R Kovsh, S S Mikhlin D A Livshits, and I L Krestnov. Subpicosecond high-power mode locking using flared waveguide monolithic quantum-dot lasers. *Appl. Phys. Lett.*, 88(13), 2006.

- [18] C M A Kapteyn, F Heinrichsdorff, O Stier, R Heitz, M Grundmann, N D Zakharov, D Bimberg, and P Werner. Electron escape from InAs quantum dots. *Phys. Rev. B*, 60(20):14265, 1999.
- [19] L. Zhang, Thomas F. Boggess, D. G. Deppe, D. L. Huffaker, O. B. Shchekin, and C. Cao. Dynamic response of 1.3 μm -wavelength InGaAs/GaAs quantum dots. *App. Phys. Lett.*, 76(10):1222–1224, 2000.
- [20] P W Fry, J J Finley, L R Wilson, A Lemaitre, D J Mowbray, M S Skolnick, M Hopkinson, G Hill, and J C Clark. Electric-field-dependent carrier capture and escape in self-assembled InAs/GaAs quantum dots. *Appl. Phys. Lett.*, 77(26):4344, 2000.
- [21] W H Chang, T M Hsu, C C Huang, S L Hsu, C Y Lai, N T Yeh, T E Nee, and J-I Chyi. Photocurrent studies of the carrier escape process form InAs self-assembled quantum dots. *Phys. Rev. B*, 62(11):6959–6962, 2000.
- [22] D V Lang. Deep-level transient spectroscopy: A new method to characterize traps in semiconductors. *J. Appl. Phys.*, 45(7):3023–3032, 1974.
- [23] J A Cavailles, D A B Miller, J E Cunningham, P L K Wa, and A Miller. Simultaneous Measurements of Electron and Hole Sweep-out from Quantum Wells and Modeling of Photoinduced Field Screening Dynamics. *IEEE J. Quant. Elect.*, 28(10):2486, 1992.
- [24] P Borri, W Langbein, J M Hvam, F Heinrichsdorff, M H Mao, and D Bimberg. Ultrafast gain dynamics in InAs-InGaAs quantum-dot amplifiers. *IEEE Photon. Technol. Lett.*, 12(6):594–596, 2000.
- [25] W Yang, R Lowe-Webb, H Lee, and P C Sercel. Effect of carrier emission and retrapping on luminescence time decays in InAs/GaAs quantum dots. *Phys. Rev. B*, 56(20):13314–13320, Nov 1997.
- [26] G Vincent, A Chantre, and D Bois. Electric field effect on the thermal emission of traps in semiconductor junctions. *J. Appl. Phys.*, 50(8):5484–5487, 1979.
- [27] H Schneider and K V Klitzing. Thermionic emission and Gaussian transport of holes in a $\text{GaAs}/\text{Al}_x\text{Ga}_{1-x}\text{As}$ multiple-quantum-well structure. *Physical Rev. B*, 38(9):6160–6165, 1988.
- [28] A Larsson, P A Andrekson, S T Eng, and A Yariv. Tunable Superlattice p-i-n Photodetectors: Characteristics, Theory and Applications. *IEEE J. Quant. Elect.*, 24(5):787–801, 1988.
- [29] Y. Zou, P. Grodzinski, E. P. Menu, W. G. Jeong, P. D. Dapkus, J. J. Alwan, and J. J. Coleman. Characterization and determination of the band-gap discontinuity of the $\text{In}_x\text{Ga}_{1-x}\text{As}/\text{GaAs}$ pseudomorphic quantum well. *Applied Physics Letters*, 58(6):601–603, 1991.
- [30] A Haus. *Compact sources of ultrashort pulses*. Cambridge University Press, Prentice Hall, 1991.
- [31] M. A. Cataluna, E. A. Viktorov, Paul Mandel, W. Sibbett, D. A. Livshits, J. Weimert, A. R. Kovsh, and E. U. Rafailov. Temperature dependence of pulse duration in a mode-locked quantum-dot laser. *Applied Physics Letters*, 90(10):101102, 2007.
- [32] R Paschotta and U Keller. Passive mode locking with slow saturable absorbers. *Applied Physics B*, 73:pp653–662, 2001.
- [33] E. A. Viktorov, Paul Mandel, Andrei G. Vladimirov, and Uwe Bandelow. Model for mode locking in quantum dot lasers. *Applied Physics Letters*, 88(20):201102, 2006.
- [34] M A Cataluna et al. Temperature dependence of pulse duration in a modelocked quantum dot laser: experiment and theory. *LEOS 2006 and Montreal and Canada and Thj*, 2006.
- [35] L. Goldstein, F. Glas, J. Y. Marzin, M. N. Charasse, and G. Le Roux. Growth by molecular beam epitaxy and characterization of InAs/GaAs strained-layer superlattices. *Applied Physics Letters*, 47(10):1099–1101, 1985.

- [36] N N Ledentsov, V A Shchukin, M Grundmann, N Kirstaedter, J Bohrer, O Schmidt, D Bimberg, V M Ustinov, A Yu Egorov, A E Zhuov, P S Kop'ev, S V Zaitsev, N Yu Gordeev, Zh I Alferov, A I Borovkov, A O Kosogov, S S Ruvimov, P Werner, U Gosele, and J Heydenreich. Direct formation of vertically coupled quantum dots in Stranski-Krastanow growth. *Phys. Rev. B*, 54(12):8743, 1996.
- [37] E. C. Le Ru, P. Howe, T. S. Jones, and R. Murray. Strain-engineered InAs/GaAs quantum dots for long-wavelength emission. *Phys. Rev. B*, 67(16):165303, Apr 2003.
- [38] Y I Mazur, Z M Wang, H Kissel, Z Y Zhuchenko, M P Lisitsa, G G Tarasov, and G J Salamo. Spectroscopy off sub-wetting layer states in InAs/GaAs quantum dot bilayers. *Semi. Sci. and Tech.*, 22:89–96, 2007.
- [39] Y T Dai, J C Fan, Y F Chen, R M Lin, S C Lee, and H H Lin. Temperature dependence of photoluminescence spectra in InAs/GaAs quantum dot superlattices with large thicknesses. *Journal of Applied Physics*, 82(9):4489–4492, 1997.
- [40] Yu. I. Mazur, J. W. Tomm, V. Petrov, G. G. Tarasov, H. Kissel, C. Walther, Z. Ya. Zhuchenko, and W. T. Masselink. Staircase-like spectral dependence of ground-state luminescence time constants in high-density InAs/GaAs quantum dots. *Applied Physics Letters*, 78(21):3214–3216, 2001.
- [41] A Miller, C B Park, and P LiKamWa. Time resolved measurements of cross-well transport in a multiple quantum well p-i-n modulator at high photogenerated carrier densities. *Appl. Phys. Lett.*, 60(1):97–99, 1991.
- [42] T. H. Wang, X. B. Mei, C. Jiang, Y. Huang, J. M. Zhou, X. G. Huang, C. G. Cai, Z. X. Yu, C. P. Luo, J. Y. Xu, and Z. Y. Xu. LO-phonon-assisted tunneling in asymmetric double-well structures with thick barriers. *Phys. Rev. B*, 46(24):16160–16162, Dec 1992.
- [43] V. Emiliani, S. Ceccherini, F. Bogani, M. Colocci, A. Frova, and Song Stone Shi. Optical investigation of carrier tunneling in semiconductor nanostructures. *Phys. Rev. B*, 56(8):4807–4817, Aug 1997.
- [44] R. Heitz, I. Mukhametzhanov, P. Chen, and A. Madhukar. Excitation transfer in self-organized asymmetric quantum dot pairs. *Phys. Rev. B*, 58(16):R10151–R10154, Oct 1998.
- [45] Yu. I. Mazur, X. Wang, Z. M. Wang, G. J. Salamo, M. Xiao, and H. Kissel. Photoluminescence study of carrier transfer among vertically aligned double-stacked InAs/GaAs quantum dot layers. *Applied Physics Letters*, 81(13):2469–2471, 2002.
- [46] Peter C. Sercel. Multiphonon-assisted tunneling through deep levels: A rapid energy-relaxation mechanism in nonideal quantum-dot heterostructures. *Phys. Rev. B*, 51(20):14532–14541, May 1995.
- [47] J W Raring, L A Johansson, E J Skogen, M N Sysak, H N Poulsen, S P DenBaars, and L A Coldren. 40-Gb/s Widely Tunable Low-Drive-Voltage Electroabsorption-Modulated Transmitters. *IEEE J. Lightwave. Tech.*, 25(1):239, 2007.
- [48] A D Ellis, J K Lucek, D Pitcher, D G Moodie, and D Cotter. Full 10×10 Gbits/s OTDM data generation and demultiplexing using electroabsorption modulators. *Electron. Lett.*, 34(18):1766–1767, 1998.
- [49] K Nishimura, R Inohara, M Tsurusawa, and M Usami. 80 Gbit/s wavelength conversion using MQW electroabsorption modulator in delayed-interferometric configuration. *Electron. Lett.*, 39(10), 2003.
- [50] T Otani, T Miyazaki, and S Yamamoto. 40-Gb/s Optical 3R Regenerator Using Electroabsorption Modulators for Optical Networks. *J. Lightwave Tech.*, 20(2):195–200, 2002.
- [51] Thomas H. Wood, John Z. Pastalan, Jr. Charles A. Burrus, Bart C. Johnson, Barry I. Miller, Jose L. deMiguel, Uziel Koren, and Martin G. Young. Electric field screening by photogenerated holes in multiple quantum wells: A new mechanism for absorption saturation. *Applied Physics Letters*, 57(11):1081–1083, 1990.

- [52] K. Obata, M. Yamanishi, Y. Yamaoka, Y. Kan, J. Hayashi, and I. Suemune. Observation of optical bistability by charge-induced self-feedback in biased AlGaAs multiple quantum well structures. *Applied Physics Letters*, 57(5):419–421, 1990.
- [53] M K Chin, S Niki, H H Wieder, and W S C Chang. Carrier screening of electric field and electroabsorption saturation in InGaAs-GaAs quantum well structure. *Electron. Lett.*, 27(25):2310–2312, 1991.
- [54] D. A. B. Miller, D. S. Chemla, T. C. Damen, A. C. Gossard, W. Wiegmann, T. H. Wood, and C. A. Burrus. Novel hybrid optically bistable switch: The quantum well self-electro-optic effect device. *Applied Physics Letters*, 45(1):13–15, 1984.
- [55] J. R. Karin, R. J. Helkey, D. J. Derickson, R. Nagarajan, D. S. Allin, J. E. Bowers, and R. L. Thornton. Ultrafast dynamics in field-enhanced saturable absorbers. *Applied Physics Letters*, 64(6):676–678, 1994.
- [56] J Wang and H C Swizer. A quantitative comparison of the classical rate-equation model with the carrier heating model on dynamics of the QW laser: The role of carrier energy relaxation, electron-hole interaction and auger effect. *IEEE J. Quantum Electron.*, 33(8):1350–1359, 1997.
- [57] C Reith. Spin relaxation and carrier recombination in GaInNAs multiple quantum wells. *phD Thesis*, page Chapter 5: Carrier lifetime, 2006.
- [58] S Hojfeldt and J Mork. Modeling of carrier dynamics in quantum well electroabsorption modulators. *J. Sel. Topics Quant. Electron.*, 8(6):1265–1275, 2002.
- [59] S Hojfeldt, F Romstad, and J Mork. Absorption recovery in strongly saturated quantum well electroabsorption modulators. *Photon. Tech. Lett.*, 15(5):676–678, 2003.

Chapter 7

Summary and Conclusions

7.1 Summary of thesis

Over the past decades, the field of optoelectronics has undergone remarkable progress. A plethora of novel devices have emerged in part due to the driving force toward all-optical communications, with the need for switching and logic applications being essential. Over the last twenty years a great amount of research has focussed on developing novel quantum confined material systems (quantum wells and more recently quantum dots) for device applications. It is within this category that the work presented in this thesis belongs. To date much of the research involving QW and QDs has focussed on their use in forward biased active devices, such as lasers and semiconductor optical amplifiers (SOAs). Also a lot of work has been carried out with QWs for their application in electroabsorption and phase modulators, however this has so far focussed primarily on AlGaAs/GaAs, InGaAs/GaAs and InGaAsP/InP material systems. In the case of QDs very little work has been devoted to devices under reverse bias such as modulators. An exception to this is the work on mode-locked semiconductor lasers, which has also employed QWs. This process involves applying a reverse bias to an isolated section of the laser in order to modulate the cavity loss through absorption saturation enabling the generation of pulses.

The devices chosen for investigation were p-i-n waveguides which are very similar in their operating principle to that of a monolithically integrated saturable absorber (used for mode-locking) and the electroabsorption modulator (used for pulse generation, demultiplexing, wavelength conversion and signal recovery). This approach was chosen to explore

an area of optoelectronic device application, still relatively new for QDs and GaInNAs QWs.

The work presented in this thesis has compared three relatively immature material systems grown on GaAs substrates for the 1.2-1.6 μ m band. What has been demonstrated is the relative benefits that each has for the applications involving modulator type devices. Chapter 5 and 6 covered effects presented in p-i-n waveguide structures in the continuous wave (CW) and pulsed optical domains, respectively. Below is a comprehensive review of each material followed by a comparison of CW and pulsed measurements, to give as close a comparison as possible for their respective application. Finally there will be a discussion of the future work that is still required to extend the development to commercial optoelectronic devices based on these emerging technologies.

7.2 InAs quantum dots

Using a broadband tuneable source of radiation, the field dependent absorption and associated refraction has been characterised for a waveguide structure containing 5 layers of isolated QDs. Measurements of the insertion loss (21dB) from scattering, radiation and coupling losses have been shown to be comparable to QW waveguide modulators [1]. Measurements of the QCSE of 15nm (11meV) at 1280nm (969meV), demonstrates a small shift in the bandedge with nominal broadening at fields up to 270KV/cm (-10V).

This work has also demonstrated a robust technique using a supercontinuum generated with a microstructured fibre for the evaluation of electroabsorption in waveguide modulator devices. Alignment is necessary for different devices, however the continuum has been shown to provide suitable power for transmission measurements through waveguides over a much larger wavelength range than achievable with tuneable lasers. The impact of this is that the Kramers-Kronig relation can be applied (through a simple numerical approximation) in order to derive the electrorefraction. This allows full characterisation of such devices, and to assess their potential for phase modulators.

Using a degenerate pump-probe technique, the carrier escape has also been measured for the isolated QDs. This technique has allowed the measurement of absorption recovery ranging from 62ps(0V) to 700fs(-10V), showing a decrease of nearly two orders of

magnitude. Upon successful fitting to simple theoretical escape processes, we have shown there exist two regimes of operation, namely thermionic emission and tunneling. Evidence confirms that tunneling is responsible for the shortest recover times and these measurements are in excellent agreement with previously reported trends observed in mode-locked semiconductor lasers. The sub-picosecond recovery in itself suggests that sub-100fs pulse generation should be possible [2]. In addition these times demonstrate the potential for modulators operating above 1THz.

The temperature stability of mode-locked lasers is also of concern in the real world. We have measured the temperature dependence of absorption recovery in isolated quantum dots and shown it to be in quantitative agreement with the pulse shortening shown in mode-locked lasers of the same material. These results indicate that whilst tunneling is responsible for the shortest recovery times, thermionic emission still plays an important role in determining the pulse duration. The benefit of these quantitative measurements allows them to be used in modeling and optimising future laser designs.

7.3 InAs Bilayer Quantum dots

Using photocurrent apparatus the field dependent band edge shift was investigated in InAs/GaAs bilayer QDs. Measurements of the QCSE revealed a shift of 40nm (28meV) at 1340nm (927meV) for an applied field of 200KV/cm. This is remarkable in itself as it compares very favorably to InGaAsP MQW waveguides at 1.3 μ m [3]. From first inspection this indicates the potential of bilayer QDs for the use in modulator devices. However the most important parameter for such devices is the on/off ratio, which is the fraction of incident light (P_{in}) to transmitted light (P_{out}). As such, it is dependent on the change in absorption ($\Delta\alpha$) and not only the magnitude of the band edge shift, and this would require further investigation. In any case as QD material typically has lower absorption than bulk or QWs and the idea of having transverse modulators is not considered practical. For the waveguide geometry used here one must take into account the confinement factor, which is the ratio of the QD fill factor to the optical mode.

We have also measured the ultrafast absorption recovery in this device recording a change from 119ps down to 5ps for an applied field of 200KV/cm (-10V). Although not

in the sub-picosecond range this offers the potential for use in modelocked semiconductor lasers, with the added advantage that the wavelength can be extended beyond $1.3\mu\text{m}$. Also, recovery times have been found to be almost unchanged ($\approx 20\text{ps}$) in the 4-6V range. This has been attributed to a resonance of the electronically coupled dots, although theoretical modeling of this system would be a great compliment here. In addition this recovery could be even faster as no attempt to ascertain the breakdown voltage was made, for obvious reasons. Waveguide devices have in the past been used with voltages of up to 20V, although for practical devices the lower voltages are more favourable.

7.4 GaInNAs Multiple Quantum wells

The use of GaInNAs is an attractive material for optoelectronic devices as it can be grown lattice matched to GaAs for the 1.2-1.6 μm band. Whilst work is beginning to emerge for its use in surface and edge emitting lasers (see chapter 1) as well as semiconductor optical amplifiers [4], there is relatively little research on this material under reverse bias operation.

Using the photocurrent apparatus again the band edge shift has been investigated for GaInNAs MQWs. Regardless of the integration platform, the optimum performance of a modulator is ultimately limited by the band-edge absorption characteristics. Measurements of the QCSE, reveal a shift of 30nm (22meV) at 1300nm (956meV) for an applied field of 190KV/cm. This is comparable to InGaAsP based QW material at 1.3 μm , indicating that GaInNAs has the potential to be used in electroabsorption modulators at these wavelengths. As mentioned above, the absorption change is also a major factor in these applications and this would require additional work.

The absorption recovery measured with femtosecond resolution shows very different characteristics for the regime of low and high applied fields. Initially at low fields of 20KV/cm (-1V) the recovery appears to be dominated by radiative and non-radiative recombination. At high fields of 190KV/cm (-7V) this recombination becomes less pronounced as the applied field leads to the electrons and holes being spatially separated at the heterobarriers. The interesting observations with QWs is that due to large densities of photogenerated carriers relative to QDs, field screening occurs and limits the overall

recovery time of the device.

The work on electroabsorption modulators by Hojfeldt et al. [5] has used extensive modeling of these effects. Using a two step heterobarrier this has been found to speed up the absorption recovery dynamic, whilst increasing the saturation energy of the device. The device under investigation in this thesis was not designed specifically as an electroabsorption modulator, and it is clear from the literature that changes in the epitaxial structure could prove a great step forward in utilising GaInNAs in this regard.

7.5 Linear measurements

Photocurrent measurements investigating the Stark shift for the application of electroabsorption modulators has been demonstrated. Both bilayer quantum dots and GaInNAs MQWs compare favourably with band edge shifts observed in InP based quantum well waveguides. It is believed that GaInNAs MQWs would have the greatest impact for electroabsorption modulators in the near future due to the large absorption coupled with the band-edge shift. The limited absorption change in single quantum dots has highlighted the need for a greater fill factor in the active region and this is also thought to affect bilayer quantum dots. In waveguide geometry an increase in the confinement factor would be preferable, as increasing the device length would also limit the frequency response of such devices. This may initially seem to be a limiting factor in QD devices due to their low density, however as growth technology has matured it is now possible to grow multiple stacks of InAs QDs in up to 150 layers if needed [6].

7.6 Time-resolved measurements

Pump-probe measurements revealing information relevant to modelocking and switching applications has been presented. Absorption recovery times on the order of a few picoseconds for bilayer QDs and sub-picosecond for isolated QDs, highlights their advantage over GaInNAs MQWs. In addition, the small QCSE and minimal broadening shown by isolated QDs is beneficial for saturable absorbers used to modelock semiconductor lasers, where a large shift in the bandedge is undesirable. Initially expected to exhibit fast recombination and therefore fast absorption recovery GaInNAs exhibits persistent field screening tran-

sients under reverse bias conditions, which are not observed in QD samples (attributed to their low dot densities). This makes it a less appealing material for the use as a monolithically integrated saturable absorber for modelocking of semiconductor lasers. However under no applied reverse bias the absorption recovery is typically found to be 50-60ps, which is still desirable for modelocking of solidstate lasers at $1.3\mu\text{m}$ (such as Nd:YLF and Cr⁴⁺:foserite) and $1.5\text{-}1.6\mu\text{m}$ (such as ErYb:YAl₃(BO₃)₄).

7.7 Device prospects

There are many parameters that define modulator characteristics; on/off ratio (R-dB), voltage required for on/off ratio (V), 3dB frequency response (f_{dB}), insertion loss and chirping parameter (α_N). It is often common to compare modulators designed for different operational wavelengths for example by using a figure of merit (FOM). The work in this thesis is not a comparison of devices designed for one particular application and as such a FOM is not practical in this instance. However the results provide a significant contribution to optical switching applications by exploring the dynamic properties close to the bandedge, as these quadratic electro-optic effects govern the fundamental operating principles. For the long term prospects it has been demonstrated that quantum dots are ideally suited for use as modelocking elements in monolithically integrated semiconductor lasers. Due to the field screening transients that exist in GaInNAs MQWs and the their slower intrinsic absorption recovery, they are more suited to electroabsorption and phase modulators. The high speed response will ultimately be limited by the RC time constant in real devices. Bilayer QDs could find use in all of the applications above as they provide both large Stark shifts and fast absorption recovery, however the low absorption still remains an issue.

7.8 Further work

In summary, the opportunities for further work on the material systems investigated in this thesis differ widely.

In the case of isolated quantum dots we have demonstrated that phase modulators are realistically possible if a larger fill factor of quantum dots can be applied. This is also the

case in the bilayer quantum dots however it would be useful to implement the transmission measurement using the continuum generator on the bilayer samples to ascertain the maximum absorption change in dB, and how this translates into a refractive index change. For the bilayer QDs, a theoretical model of the electronically coupled system would be a great compliment to these initial results. This is an extremely new material that has yet to be implemented in any device application.

From the point of view of electroabsorption modulators, there are two areas of further work that are paramount for real-world devices. The first regards the 3dB frequency response of these devices and secondly, the chirp parameter, (ratio of the real to imaginary part of the refractive index) both of which would need to be ascertained for all three devices. However the work in this thesis has highlighted the particular applications that would benefit from the addition of these materials.

References for Chapter 7

- [1] T H Wood. Multiple quantum well (MQW) waveguide modulators. *J. Lightwave Tech.*, 6(6):743–757, 1988.
- [2] E U Rafailov, M A Cataluna, W Sibbet, N D Ii'inskaya, Y M Zadiranov, A E Zhukov, V M Ustinov, D A Livshits, A R Kovsh, and N N Ledentsov and. High-power picosecond and femtosecond pulse generation from a two-section mode-locked quantum-dot laser. *Appl. Phys. Lett.*, 87(8), 2005.
- [3] J. E. Zucker, I. Bar-Joseph, B. I. Miller, U. Koren, and D. S. Chemla. Quaternary quantum wells for electro-optic intensity and phase modulation at 1.3 and 1.55 μm . *Applied Physics Letters*, 54(1):10–12, 1989.
- [4] J Hashimoto, K Koyama, T Katsuyama, Y Iguchi, T Yamada, S Takagishi, M Ito, and A Ishida. 1.3 μm Traveling-Wave GaInNAs Semiconductor Optical Amplifier. *Jap. J. App. Phys.*, 43(6A):3419–3423, 2004.
- [5] S Hojfeldt and J Mork. Modeling of carrier dynamics in quantum well electroabsorption modulators. *J. Sel. Topics Quant. Electron.*, 8(6):1265–1275, 2002.
- [6] Jun Inoue, Toshiro Isu, Kouichi Akahane, and Masahiro Tsuchiya. Saturable absorption of highly stacked inas quantum dot layer in 1.5 μm band. *Applied Physics Letters*, 89(15):151117, 2006.

Appendix A

Numerical evaluation of the Kramers-Krönig relations

The real and imaginary parts of a complex function that has no poles in either the upper or lower complex plane are related by the Hilbert transformation. When this theorem is applied in particular to the complex susceptibility function $\chi(\omega) = \chi_1(\omega) - i\chi_2(\omega)$ the result is known as the Kramers-Kronig relations as follows,

$$\chi_1(\omega) = \frac{1}{\pi} P \int_{-\infty}^{\infty} \frac{\chi_2(\omega')}{\omega' - \omega} d\omega' \quad (\text{A.1})$$

$$\chi_2(\omega) = \frac{-1}{\pi} P \int_{-\infty}^{\infty} \frac{\chi_1(\omega')}{\omega' - \omega} d\omega'. \quad (\text{A.2})$$

Here P denotes the Cauchy principal value (the limit of an indefinite integral). We can use these relations in the study of the QCSE by way of relating the real and imaginary parts of χ to the more physically intuitive parameters of refraction (n) and absorption (α). Mathematically,

$$\left[n(\omega) + i \frac{\alpha(\omega)c}{2\omega} \right]^2 = 1 + \chi_1(\omega) + i\chi_2(\omega), \quad (\text{A.3})$$

where $n(\omega)$ is the real part of the complex refractive index. These ideas are described in more depth in chapter 1.

The Kramers-Kronig relations can be used to calculate the change in refractive index

from the change in absorption due to some external perturbation (in this case an applied electric field). Equations A.1 and A.2 can be applied in the presence and in the absence of the perturbation and the difference taken [1], to relate the change in refractive index to the change in absorption as follows,

$$\Delta n(\omega) = \frac{c}{\pi} P \int_0^{\infty} \frac{\Delta \alpha(\omega')}{\omega'^2 - \omega^2} d\omega'. \quad (\text{A.4})$$

Furthermore, this way of calculating the change in refractive index is relatively straight forward since $\Delta \alpha \neq 0$) only over a limited range of ω and thus the integral in equation A.4, only needs to be calculated over this finite range.

In most cases the integral being evaluated in equation A.4 does not have an analytical solution and so needs to be approximated numerically. There is clearly an issue in the above transform, due to the singularity at the point $\omega' = \omega$. Various methods have been used to take this point into account, as reviewed in [2]. They arrive at the conclusion that the simplest method (referred to as Maclaurin's formula) also yields the lowest error. The formula works as follows: if the singularity occurs at an odd frequency point then the integral is performed only over the even frequency points, and if it occurs at an even point then in the integration only odd frequency points are considered. For the results in chapter 5 the method used was adopted from [3] whereby the integral proceeds as normal but is only carried out for every other point except the one being investigated and as will be shown below the error is extremely small. Below is a comparison between Method A (using the Maclaurin expansion), as taken from ref. [2] and Method B (the method adopted by Lucarini et al. [3]).

In order to assess the validity of the approximation we need to use a reference function which has an analytical solution. One example is the driving point impedance for an RC circuit, where the transform of the circuit resistance (R) is in fact the reactance (X) [4]. We calculated the result of this and the methods proved excellent, however due to the nature of the frequency range in which this work took place a more suitable function is the sum of two lorentzians,

$$\Delta \alpha(\omega) = \frac{\alpha_{max}(\gamma/2)^2}{(\omega - \omega_0)^2 + (\gamma/2)^2} - \frac{\alpha_{max}(\gamma/2)^2}{(\omega + \omega_0)^2 + (\gamma/2)^2}. \quad (\text{A.5})$$

This gives the following analytical solution for Δn ,

$$\Delta n(\omega) = \alpha_{max} \left[-\frac{(\omega - \omega_0)(\gamma/2)}{(\omega - \omega_0)^2 + (\gamma/2)^2} + \frac{(\omega + \omega_0)(\gamma/2)}{(\omega + \omega_0)^2 + (\gamma/2)^2} \right]. \quad (\text{A.6})$$

The graphical representation of the equations A.5 and A.6 are given below. The number of points chosen was 300, reflecting the resolution of the experimental measurement, were $\omega_0 = 2 \times 10^{15}$ and $\gamma = 12 \times 10^{13}$. All computation was carried out in MATLAB.

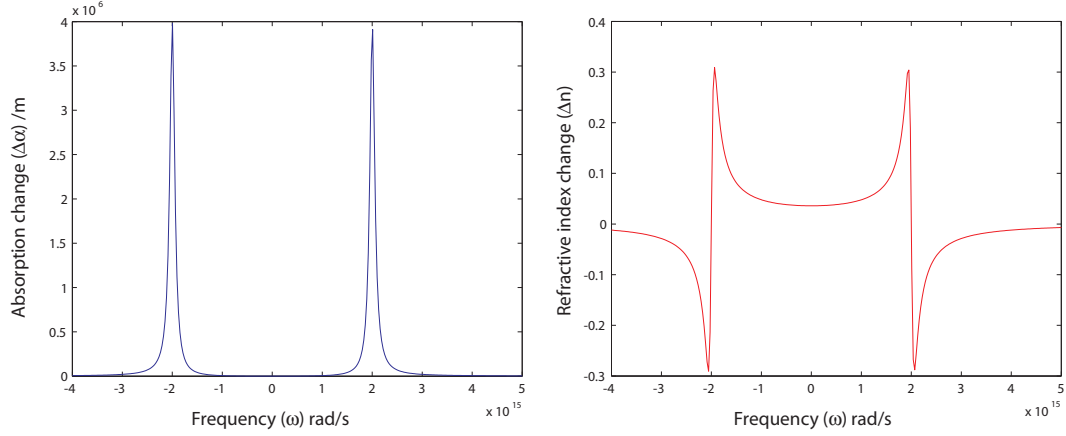


Figure A.1: Graphical solution for double Lorentzian function and the analytical solution via the Kramers-Kronig transformation as used for assessing the numerical approximation methods.

We will firstly outline the associated discretized parameters for the integration. The values of the absorption $\Delta\alpha$ are discrete values $\Delta\alpha(\omega_j)$ with a set of N values given by equally spaced frequencies ω_j . The interval of these steps is given by $\Delta\omega = \omega_{j+1} - \omega_j$, where $\Delta\alpha(\omega_j)$ is zero everywhere outside the finite range $\omega_1 - \omega_N$.

A.0.1 Method A

In this method the number of points evaluated in one integration is $N/2$ due to the nature of the algorithm taking every other point to avoid the pole at $j=i$. When i is odd, $j=2,4,6,\dots,i-1,i+1,N$. On the other hand when i is even, $j=1,3,5,\dots,i-1,i+1,N$. This can be described mathematically as,

$$I_i = \frac{c}{\pi} \times 2\Delta\omega \times \left(\sum_j \frac{\Delta\alpha_j}{\omega_j^2 - \omega_i^2} \right). \quad (\text{A.7})$$

In the computation the Lorentzian line shape absorption is taken and a numerical esti-

mate of the refractive index is accomplished.

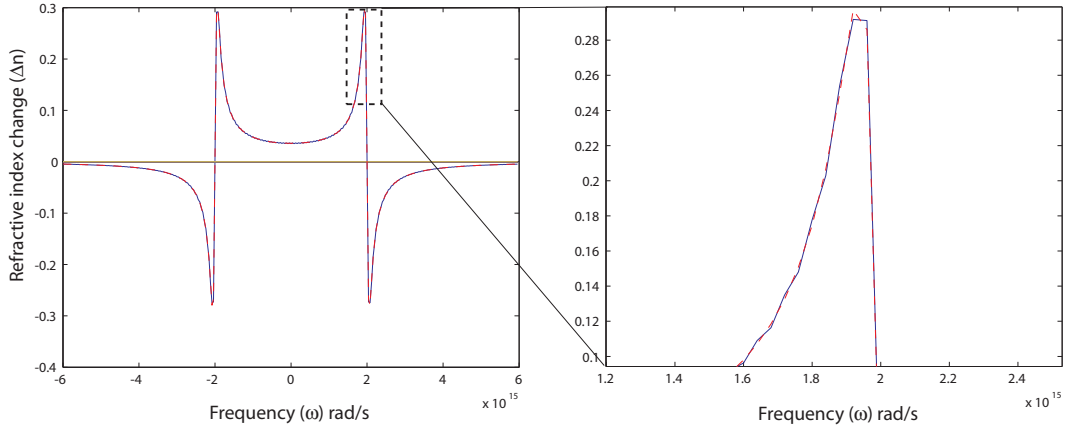


Figure A.2: Numerical approximation to the change in refractive index based on the double Lorentzian absorption function using the Maclaurin formula. Red dashed line indicates analytical result, blue line is numerical approximation.

In the above figure the agreement between analytical and numerical results is extremely good and there is little reason to plot the rms difference between the numerical and analytic results. The error is smaller than 5% at the sharpest feature.

A.0.2 Method B

The method adopted by Lucarini involves slightly more code as it routinely works out which point is the pole and therefore which point to exclude in each successive integration. The computation time is slightly longer than that for method A, including all 300 points, however it is still only a matter of seconds. The sum can similarly be represented mathematically as,

$$I_i = \frac{c}{\pi} \times \Delta\omega \times \left(\sum_{j \neq i} \frac{\Delta\alpha_j}{\omega_j^2 - \omega_i^2} \right). \quad (\text{A.8})$$

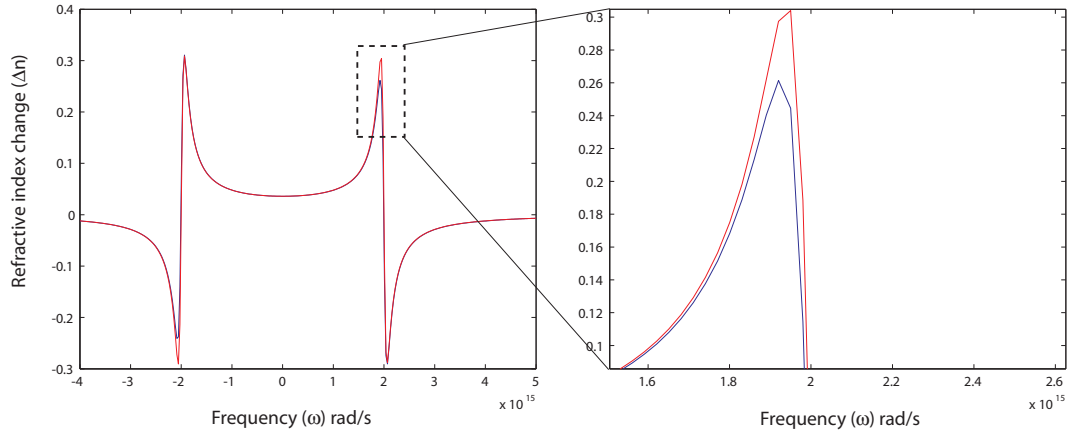


Figure A.3: Numerical approximation to the change in refractive index based on the double Lorentzian absorption function using the Lucarini method. Red line indicates analytical result, blue line is numerical approximation.

In figure A.3 the same feature is shown where the numerical approximation is worst, however this has an error of approximately 13% and is a very good fit elsewhere and again is not necessary to plot the rms error.

A.0.3 Discussion

Both methods are clearly excellent numerical approximations to the Kramers-Kronig transform relating changes in absorption and refractive index. Method A gives slightly better results, however neither makes any approximation to the pole point and are very similar in practice.

This also validates Method B which is used to estimated the change in refractive index based in experimentally measured absorption changes for the QD waveguide in chapter 5.

References for Chapter A

- [1] D C Hutchings, M Sheik-Bahae, D J Hagan, and E W Van Stryland. Kramers-Krönig relations in nonlinear optics. *Opt. Quant. Electron.*, 24:1–30, 1992.
- [2] K Ohta and H Ishida. Comparison among several numerical integration methods for Kramers-Kronig transformation. *Applied Spectroscopy*, 42(6):p952–p957, 1988.
- [3] V Lucarini, J J Saarinen, and K-E Peiponen E M Vartiainen. Kramers-Kronig relations in optical material research. *New York Springer*, 2005.
- [4] J T Verdeyen. Laser Electronics 3_{rd} edition. *Prentice Hall series in solid state physical electronics*, pages p774–778, 1995.

Publications

"Electroabsorption and Electrorefraction in an InAs Quantum-Dot Waveguide Modulator". D. B Malins, A. Gomez-Iglesias, E. U. Rafailov, W. Sibbet and Alan Miller. *Photon. Technol. Lett.* 19 (15) pp1118 2007.

"Quantum-confined Stark effect and ultrafast absorption dynamics in a bilayer InAs quantum dot waveguide". D. B Malins, A. Gomez-Iglesias, P. Spencer, E. Clarke, R. Murray and A. Miller. *Electron. Lett.* 43 (12) pp686 2007.

"Ultrafast electroabsorption dynamics in an InAs quantum dot saturable absorber at 1.3 μ m". D. B Malins, A. Gomez-Iglesias, S. J. White, E. U. Rafailov, W. Sibbet and Alan Miller. *App. Phys. Lett.* 89 (171111) 2006.

Conferences

"Temperature dependence of electroabsorption dynamics in an InAs quantum dot saturable absorber at 1.3 μ m". D. B Malins, A. Gomez-Iglesias, M. A. Cataluna, E. U. Rafailov, W. Sibbet and Alan Miller. CLEO Europe '07, June 17th-22nd 2007 poster presentation.

"Ultrafast electroabsorption dynamics in an InAs quantum dot saturable absorber at 1.3 μ m". D. B Malins, A. Gomez-Iglesias, S. J. White, E. U. Rafailov, W. Sibbet and Alan Miller. Oral presentation C-0-1. IoP Compound Semiconductor Conference Sheffield, July, 2006.

Acknowledgements

I would dearly like to acknowledge a number of people, without whom, this thesis would never have been completed.

I would like to thank especially Professor Alan Miller for his guidance and logical approach to problem solving which gave me the confidence to tackle many obstacles. I am also grateful to the Ultrafast Photonics Collaboration (EPSRC) for funding my studentship.

To postdocs, past and present...

Steven White for his hands-on laser development guidance, introducing me to running and reminding me of my roots.

To Mike Mazilu for his technical support of Mathematica and VEE . When the books didn't have the answer, you did.

To Alvaro Gomez-Iglesias for imparting his substantial knowledge of all things Semiconductor and his critical assessment of my work.

To integral members of the supply chain...

I am indebted to Dr Edik Rafailov for the QD sample and his encouragement in publishing my first results, which was the catalyst for subsequent papers.

I wish to thank Peter Spencer of Imperial college for the bilayer QD samples and his colourful tales of MBE growth.

To Mircea Guina for supplying the GaInNAs wafer which enabled the processing of devices as part of my work.

In respect of this, To Maria Kotlyar and Steven Moore, a big thankyou for introducing me to the cleanroom and imparting your valuable skills and knowledge in the field of processing.

To my fellow PhD colleges, Charis Reith, Matthew Bell, Jean-Francois Gallet, Andrew Woodman and Tim Karle. I wish to thank you all for your encouragement over the past few years and for intelligent conversation over the odd pint or three.

To Friday football and Monkeys United, gone but not forgotten. Thank you all for taking my mind away from the lab.

Finally to my family, in particular my parents, without whom I would never have reached the finish line. Thank you for all the encouragement and putting up with my stressful ramblings. "Act thick and have a few laughs"..... if only I could.